

# **k·p theory for two-dimensional transition metal dichalcogenide semiconductors**

**Andor Kormányos<sup>1</sup>, Guido Burkard<sup>1</sup>**

<sup>1</sup> Department of Physics, University of Konstanz, D-78464 Konstanz, Germany

**Martin Gmitra<sup>2</sup>, Jaroslav Fabian<sup>2</sup>**

<sup>2</sup> Institute for Theoretical Physics, University of Regensburg, D-93040 Regensburg, Germany

**Viktor Zólyomi<sup>3</sup>, Neil D. Drummond<sup>3</sup>, Vladimir Fal'ko<sup>3</sup>**

<sup>3</sup> Department of Physics, Lancaster University, Lancaster LA1 4YB, United Kingdom

E-mail: andor.kormanyos@uni-konstanz.de

E-mail: guido.burkard@uni-konstanz.de

## **Abstract.**

We present **k·p** Hamiltonians parametrised by *ab initio* density functional theory calculations to describe the dispersion of the valence and conduction bands at their extrema (the *K*, *Q*,  $\Gamma$ , and *M* points of the hexagonal Brillouin zone) in atomic crystals of semiconducting monolayer transition metal dichalcogenides. We discuss the parametrisation of the essential parts of the **k·p** Hamiltonians for MoS<sub>2</sub>, MoSe<sub>2</sub>, MoTe<sub>2</sub>, WS<sub>2</sub>, WSe<sub>2</sub>, and WTe<sub>2</sub>, including the spin-splitting and spin-polarisation of the bands, and we briefly review the vibrational properties of these materials. We then use **k·p** theory to analyse optical transitions in two-dimensional transition metal dichalcogenides over a broad spectral range that covers the Van Hove singularities in the band structure (the *M* points). We also discuss the visualisation of scanning tunnelling microscopy maps.

PACS numbers:

## **Contents**

<b>1</b>	<b>Introduction</b>	<b>2</b>
<b>2</b>	<b>Lattice parameters, band-structure calculations and vibrational properties</b>	<b>4</b>
<b>3</b>	<b>Band-edge energy differences and spin-splittings</b>	<b>7</b>
<b>4</b>	<b>Valence band width <math>D_{vb}</math></b>	<b>9</b>

<b>5</b>	<b>Effective model at the <math>K</math> and <math>-K</math> points</b>	<b>10</b>
5.1	$K$ and $-K$ points . . . . .	10
5.2	Basic characterization and material parameters . . . . .	10
5.3	$\mathbf{k} \cdot \mathbf{p}$ Hamiltonian . . . . .	16
<b>6</b>	<b>Effective models at the <math>Q</math> (a.k.a. <math>\Lambda</math>) point</b>	<b>22</b>
6.1	$Q_i$ points . . . . .	22
6.2	Basic characterisation and material parameters . . . . .	22
6.3	$\mathbf{k} \cdot \mathbf{p}$ Hamiltonian . . . . .	24
<b>7</b>	<b>Effective models at the <math>\Gamma</math> point</b>	<b>26</b>
7.1	$\Gamma$ point . . . . .	26
7.2	Basic characterisation and material parameters . . . . .	27
7.3	$\mathbf{k} \cdot \mathbf{p}$ Hamiltonian . . . . .	29
7.4	$\Gamma$ point wave functions and STM measurements . . . . .	33
<b>8</b>	<b>The <math>M</math> point: spin-orbit splitting of the Van Hove singularity</b>	<b>35</b>
8.1	Basic characterisation and $\mathbf{k} \cdot \mathbf{p}$ Hamiltonian . . . . .	35
<b>9</b>	<b>Conclusions</b>	<b>39</b>
<b>10</b>	<b>Acknowledgement</b>	<b>39</b>
	<b>Appendices</b>	<b>39</b>

## 1. Introduction

Monolayers of transition metal dichalcogenides (TMDCs) [1, 2] are truly two-dimensional (2D) semiconductors [3, 4, 5, 6, 7, 8, 9, 10, 11], which hold great appeal for electronics and opto-electronics applications due to their direct band gap properties (which contrast the indirect band gaps of three-dimensional layered crystals of TMDCs). Monolayer TMDCs have already been implemented in field-effect transistors [12, 13, 14, 15, 16, 17, 18], logical devices [15, 19], and lateral and tunnelling optoelectronic structures [20, 21, 22, 23, 24].

Like graphene, the group-IVB monolayer TMDCs of chemical composition  $\text{MX}_2$  (where  $\text{M}=\text{Mo}$  or  $\text{W}$  and  $\text{X}=\text{S}$ ,  $\text{Se}$  and  $\text{Te}$ ) considered in this work have hexagonal lattice structures, and the extrema (valleys) in the dispersion relations of both the valence and conduction bands (VB and CB) can be found at the  $K$  and  $-K$  points of the hexagonal Brillouin zone (BZ). Unlike graphene, however, these 2D crystals do not have inversion symmetry. The minimalistic approach to the theoretical modelling of monolayer TMDCs is therefore based on mimicking them as graphene with a staggered sublattice potential that breaks inversion symmetry [25, 26]. This approach captures certain optical and transport effects related to the valley degree of freedom of the electrons [26, 27, 28, 29, 30, 31]. The staggered graphene analogue [26] has also been generalised

to the tight-binding (TB) description of TMDCs [26, 32, 33, 34, 35, 36, 37, 38], but this approach suffers from the large number of atomic orbitals that have to be included on each site and the need for beyond-nearest-neighbour hopping to account for the variation of the weight of individual atomic orbitals in the band wave functions across the BZ, as revealed by detailed density functional theory (DFT) modelling (see, e.g., Figure 3). The accumulation of experimental data and the drive towards the implementation of monolayer TMDCs in practical devices call for theoretical models of their electronic properties that are both detailed and compact, containing a limited number of parameters while still offering an accurate description.

In this Review, we describe two complementary theoretical approaches that have recently been used to achieve a detailed description of the electronic properties of these materials. One consists of *ab initio* DFT modelling of the band structure, which has the potential to be accurate. DFT can be combined with transport codes [17, 38, 39, 40, 41, 42, 43, 44] or used to calculate optical spectra [45, 46, 47, 48], but *ab initio* calculations are prohibitively expensive for many practical problems focused on modelling devices and studies of, e.g., quantum dots [49, 50]. Moreover, magnetic-field effects [32, 49, 51, 52, 53, 54] and certain questions regarding neutral and charged excitons [55] cannot easily be addressed by DFT-based techniques. The second approach uses the  $\mathbf{k} \cdot \mathbf{p}$  methodology [56, 57, 58, 59], which exploits the symmetries of the system. This approach provides an accurate characterisation of the dispersion of the valence and conduction bands in the vicinity of, e.g., the  $K$  and  $-K$  points and other points of interest in the BZ in terms of a relatively small number of parameters [60]. Magnetic-field and spin-orbit coupling effects can also be taken into account in a straightforward way [49]. In contrast to DFT modelling, this method is only valid in the vicinity of certain high-symmetry  $\mathbf{k}$ -space points; however, for those intervals, it enables one to quantify all the essential features of the electronic properties. One can also relate a  $\mathbf{k} \cdot \mathbf{p}$  Hamiltonian to a particular TB model [26, 32, 34], although it is not necessary to set up a TB model in order to derive a  $\mathbf{k} \cdot \mathbf{p}$  Hamiltonian. Here we present phenomenological  $\mathbf{k} \cdot \mathbf{p}$  Hamiltonians derived for all extrema of the bands (at the  $K$ ,  $Q$ ,  $\Gamma$ , and  $M$  points of the BZ) using the symmetry properties of TMDC atomic crystals, with specific material parameters obtained by fitting them to the DFT band structures of  $\text{MoS}_2$ ,  $\text{MoSe}_2$ ,  $\text{MoTe}_2$ ,  $\text{WS}_2$ ,  $\text{WSe}_2$  and  $\text{WTe}_2$ . ‡ The DFT calculations discussed in this Review were

‡ Most of the recent theoretical and experimental work has focused on the properties of  $\text{MoS}_2$ ,  $\text{MoSe}_2$ ,  $\text{WS}_2$  and  $\text{WSe}_2$ , while  $\text{MoTe}_2$  and  $\text{WTe}_2$  have received much less attention. Bulk  $\text{MoTe}_2$  with a trigonal prismatic coordination of the chalcogen atoms (see Figure 1(a)) exists below  $815^\circ\text{C}$  (known as  $\alpha$ - $\text{MoTe}_2$ ), whereas above  $900^\circ\text{C}$  the crystal structure is monoclinic and the material becomes metallic ( $\beta$ - $\text{MoTe}_2$ ) [61, 62]. Monolayer samples using liquid exfoliation technique have been obtained from  $\alpha$ - $\text{MoTe}_2$  [63], and the optical properties of monolayer [192] the transport properties of few-layer  $\alpha$ - $\text{MoTe}_2$  [64, 191] have been investigated recently, giving a clear motivation to include this material in our review. Bulk  $\text{WTe}_2$  has an orthorhombic crystal structure, where eight tellurium atoms surround the tungsten atom in a distorted octahedral coordination [65, 66]. Nevertheless, one would expect that it may be possible to grow monolayer  $\text{WTe}_2$  with hexagonal prismatic coordination on a suitable substrate. For completeness, therefore, we include this material as well, assuming that its hexagonal

performed using the VASP [67] and FLEUR [68] codes. The robustness of our results is well illustrated by the close agreement between the results obtained from these two different first-principles codes and through comparison to all available experimental results.

Finally, we note that the field of TMDCs, akin to that of graphene [69, 70, 71, 72], has witnessed a large expansion over the last four years, encompassing both fundamental and more applications-oriented research directions. Here we focus on a particular topic that we think will be important for the further development of this field. To limit the length of this review, some fascinating topics related to, e.g., the valley-dependent optical selection rule or the exciton physics are not discussed in detail here. We refer the interested reader to complementary reviews [73, 74, 75, 76, 77, 78, 79, 80] instead.

This Review is organised as follows. Section 2 is devoted to the crystalline lattice parameters and vibrational properties of TMDCs. Sections 3 and 4 discuss spin-splitting due to spin-orbit coupling (SOC) and band width [relevant for angle-resolved photoemission spectroscopy (ARPES) studies of TMDCs]. Sections 5, 6, 7, and 8 describe the structure and parametrisation of  $\mathbf{k} \cdot \mathbf{p}$  Hamiltonians for  $K$ ,  $Q$ ,  $\Gamma$ , and  $M$  points of the BZ, respectively. Finally, we draw our conclusions in Section 9.

## 2. Lattice parameters, band-structure calculations and vibrational properties

The crystal structure of each  $\text{MX}_2$  monolayer considered in this work consists of three atomic layers, X–M–X. Within each layer the M or X atoms form a 2D hexagonal lattice: see Figure 1. The M atoms in the middle plane are surrounded by three nearest-neighbour X atoms in both the bottom and the top layer so that the crystal has  $D_{3h}$  symmetry. The crystal structure is characterised by the in-plane lattice constant  $a_0$  and the distance  $d_{X-X}$  between the two chalcogen planes. It has already been noted [81] that certain details of the band structure obtained from DFT calculations depend rather sensitively on  $a_0$  and  $d_{X-X}$ . Indeed, we have also found that agreement with the available experimental results regarding, e.g., the effective mass  $m_{\Gamma}^{\text{vb}}$  at the  $\Gamma$  point of the BZ or the energy difference  $E_{K\Gamma}$  between the top of the VB at the  $K$  and  $\Gamma$  points can only be achieved if the values of  $a_0$  and  $d_{X-X}$  fall in a rather narrow range.

As a first step, we have used two approaches to calculate the basic lattice parameters  $a_0$  and  $d_{X-X}$ . The first approach used VASP [67]. The VASP geometries were calculated using the Heyd–Scuseria–Ernzerhof 2006 (HSE06) exact-exchange density functional [82]. The plane-wave cutoff energy was set to 600 eV and the BZ was sampled by a  $12 \times 12 \times 1$  Monkhorst–Pack grid. The vertical separation between the layers was set to 20 Å to make the interaction between the repeated images of the layer in the three-dimensional cell negligible. Optimisation was carried out until atomic forces fell below 0.005 eV/Å. The second approach used the full-potential linearised augmented plane-wave (FLAPW) method as implemented in the FLEUR code [68]. The FLAPW method is an all-electron method within DFT. The FLEUR code allows 2D systems structure is stable.

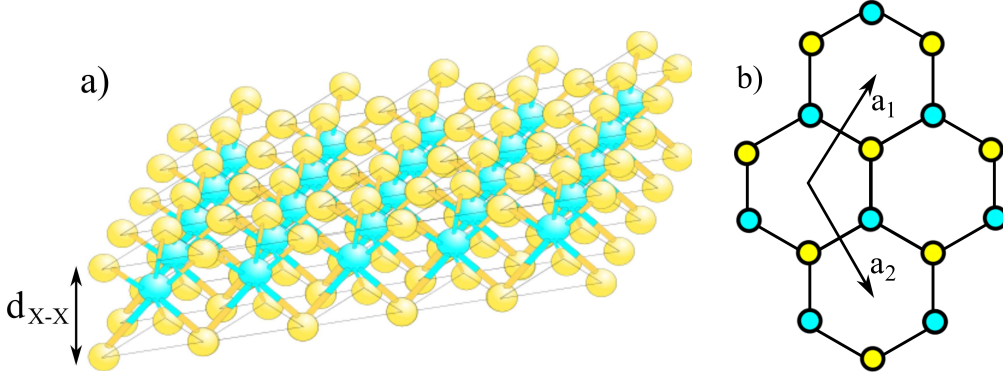


**Figure 1.** Crystal structure of monolayer  $\text{MX}_2$ . a) Side view and b) top view. Metal atoms are cyan and chalcogens are yellow. The lattice vectors  $\mathbf{a}_1$  and  $\mathbf{a}_2$  are also shown.

to be studied without constructing slabs in three-dimensionally periodic cells and the resulting electronic spectra are free of plane-wave continua. All our FLEUR calculations were carried out with a cut-off  $k_{\text{max}}$  of  $10.6 \text{ eV}^{-1}$  for the plane-wave basis set and 144  $\mathbf{k}$  points corresponding to a  $12 \times 12 \times 1$  Monkhorst–Pack grid in the irreducible wedge of the BZ. Muffin-tin radii of 1.0, 1.21, 1.27, 1.27, and  $1.27 \text{ \AA}$  were used for S, Se, Te, Mo, and W, respectively. We note that considering local orbitals for Mo ( $s, p$ ), Se ( $s, p, d$ ), and W ( $s, p, f$ ) to improve the linearised augmented plane-wave basis proved to be crucial for a correct description of the excited states. We used the Perdew–Burke–Ernzerhof (PBE) generalised gradient approximation [83] to the exchange-correlation potential. The structures were relaxed (with the effects of SOC included) until the forces were less than  $0.0005 \text{ eV/\AA}$ .

The calculated values of  $a_0$  and  $d_{S-S}$  for monolayer TMDCs are shown in Table 1 and compared to measured values for the corresponding *bulk* materials. The lattice parameters obtained from the first of the DFT approaches described above are shown in the rows labelled by “(HSE)”, the ones from the second approach are in the rows labelled by “(PBE)”. “(Exp)” indicates experimental results found in the literature. Although there is some scatter in the experimental data, Table 1 suggests that using the HSE06 functional to relax the monolayer crystal structure leads to a good agreement with the *room-temperature* empirical *bulk*  $a_0$  values. On the other hand, the PBE functional seems to slightly overestimates  $a_0$ . However, the situation is less clear in the case of  $d_{X-X}$ . We note that both the HSE06 and the PBE results are in good agreement with Reference [84].

Recent experiments show that the energy of the photoluminescence peak is quite sensitive to the temperature [5, 85, 86], which can be understood in terms of the dependence of the band structure on  $a_0$  and  $d_{X-X}$ . Indeed, a recent computational study [87] was able to qualitatively reproduce the redshift of the photoluminescence peak of  $\text{MoS}_2$  as a function of temperature by assuming a thermal expansion of the lattice. The good agreement between the calculated lattice parameters and the corresponding

**Table 1.** Lattice vector  $a_0$  and chalcogen–chalcogen distance  $d_{X-X}$  as obtained from DFT calculations. Experimental values for the corresponding bulk material are shown in rows labelled by “Exp”. For WTe<sub>2</sub> experimental results are only available for the orthorhombic structure and are therefore not shown.

	MoS <sub>2</sub>	MoSe <sub>2</sub>	WS <sub>2</sub>	WSe <sub>2</sub>	MoTe <sub>2</sub>	WTe <sub>2</sub>
$a_0$ [Å] (HSE)	3.1565	3.289	3.16	3.291	3.516	3.521
$a_0$ [Å] (PBE)	3.1854	3.319	3.18	3.316	3.557	3.553
$a_0$ [Å] (Exp)	3.1604 <sup>a</sup>	3.288 <sup>a</sup>	3.154 <sup>a,b</sup>	3.286 <sup>a</sup>	3.519 <sup>j</sup>	–
	3.14 <sup>c</sup>	3.299 <sup>c</sup>	3.1532 <sup>d</sup>	3.282 <sup>c</sup>	3.522 <sup>c,k</sup>	–
	3.1602 <sup>e</sup>	3.289 <sup>e</sup>		3.282 <sup>d</sup>	3.517 <sup>a</sup>	–
	3.1475 <sup>f</sup>	3.290 <sup>g</sup>				–
						–
$d_{X-X}$ [Å] (HSE)	3.0996	3.307	3.1176	3.327	3.5834	3.5999
$d_{X-X}$ [Å] (PBE)	3.1246	3.4371	3.1529	3.471	3.6195	3.6394
$d_{X-X}$ [Å] (Exp)	3.17 <sup>e</sup>	3.335 <sup>e</sup>	3.14 <sup>d</sup>	3.34 <sup>d</sup>	3.604 <sup>k</sup>	–

<sup>a</sup>[88], <sup>b</sup>[89], <sup>c</sup>[90], <sup>d</sup>[91], <sup>e</sup>[92], <sup>g</sup>[93], <sup>j</sup>[94], <sup>k</sup>[62].

<sup>f</sup>[95], measurement at 293 K.

experimental ones suggests that, interestingly, the predictions based on our DFT results are expected to be most accurate at room temperature (except for the band gap, which is known to be underestimated by DFT). To our knowledge systematic measurements of the temperature-dependence of the lattice parameters of bulk MX<sub>2</sub> have not been performed, except for MoS<sub>2</sub> [95].

As in the case of the lattice parameters, we have used both the VASP and the FLEUR codes to calculate the band structures of monolayer TMDCs. For the VASP calculations we used the HSE lattice parameters as input. The band structures were calculated in the local density approximation (LDA). SOC was taken into account in the non-collinear magnetic structure approach with the symmetry turned off. The charge density was obtained self-consistently using a  $12 \times 12 \times 1$   $\mathbf{k}$ -point grid and a 600 eV cutoff energy. The results obtained by this method are shown in rows denoted by “(HSE,LDA)” in Tables 2–10 below. For the FLEUR calculations the charge densities obtained from the geometry relaxation calculations (see Section 2) were used for further calculation of the band structure and spin expectation values. SOC in FLEUR is included within the second variational method for the valence electrons, whereas the core electrons are treated fully relativistically. These results are in rows denoted by “(PBE,PBE)” in Tables 2–10 below.

One possibility, which we did not explore, is to use the HSE lattice parameters and the HSE06 functional for band-structure calculations, as in Reference [84]. We note that the results of Reference [84] seem to indicate that the HSE06 functional gives larger VB spin-splittings than found experimentally.

In addition to the band structure of the TMDCs, which is our main focus in this work, electron–phonon coupling is also essential in order to understand transport [39, 40, 41] and relaxation [96] processes. For completeness, we give a brief review of the

vibrational characteristics of monolayer TMDCs. *Ab initio* lattice-dynamics calculations indicate that single layers of the TMDCs MoS<sub>2</sub>, MoSe<sub>2</sub>, WS<sub>2</sub>, and WSe<sub>2</sub> are dynamically stable [97, 98, 99], in agreement with experiments.

A comprehensive group-theory analysis of the different polytypes and stacking arrangements of few-layer TMDCs is presented in Reference [100]. The symmetry of few-layer structures determines which phonon modes are Raman-active, and therefore provides an important means of characterising samples. As mentioned earlier, monolayer MX<sub>2</sub> has  $D_{3h}$  point-group symmetry (see Table 11 for the character table and irreducible representations). The six zone-centre optical phonon modes may be classified according to the irreducible representations under which their eigenvectors transform: in the twofold-degenerate  $E''$  modes the metal atom remains stationary while the chalcogen atoms vibrate in opposite in-plane directions; in the twofold-degenerate  $E'$  modes the chalcogen atoms vibrate together in-plane in the opposite direction to the metal atom; in the non-degenerate  $A'_1$  mode the metal atom remains stationary while the chalcogen atoms vibrate in opposite out-of-plane directions; finally, in the non-degenerate  $A''_2$  mode the chalcogen atoms vibrate together out-of-plane in the opposite direction to the metal atom. Of these vibrations, all but the  $A''_2$  mode are Raman-active. Only the  $E'$  and  $A''_2$  modes are infrared-active.

DFT-LDA and DFT-PBE results for the phonon frequencies are summarised in Table 1 of Reference [101]. There is a reasonable degree of agreement between the LDA and PBE results, suggesting that the DFT phonon frequencies are accurate. Subsequent theoretical studies [97, 98, 99] have reproduced the results of Reference [101] for the monolayer. Regarding WTe<sub>2</sub>, we note that our calculations give real phonon frequencies in the whole BZ, indicating that the assumed hexagonal structure may indeed be stable. In experimental studies of thin films of WS<sub>2</sub>, WSe<sub>2</sub>, and MoS<sub>2</sub> it is found that modes that were Raman inactive in the bulk become active in thin films and that there are small shifts in the phonon frequencies on going from the bulk to a thin film [102, 103, 104]. Where comparison is possible, the experimental Raman frequencies of thin films are in agreement with the DFT results.

### 3. Band-edge energy differences and spin-splittings

Detailed discussion of the conduction and valence band dispersions in the vicinity of the  $\mathbf{k}$ -space points of interest ( $K$ ,  $Q$ ,  $\Gamma$ , and  $M$ ) will be given in Sections 5, 6, 7, and 8. In this section we briefly introduce the various band-splittings and band-edge energy differences that we use to characterise the band structure. An overview of the band structure obtained from DFT calculations is shown in Figure 2. The direct band gap  $E_{\text{bg}}$  of monolayer TMDCs can be found at the  $K$  and  $-K$  points of the BZ. Due to the lack of inversion symmetry, all bands are split by the intrinsic SOC except at the time-reversal invariant points  $M$  and  $\Gamma$ . We denote by  $2\Delta_{\text{vb}}$  and  $2\Delta_{\text{cb}}$  the spin-splitting of the VB and CB, respectively. There are another six minima in the CB that might be important, e.g., for transport or relaxation processes in certain compounds. We denote

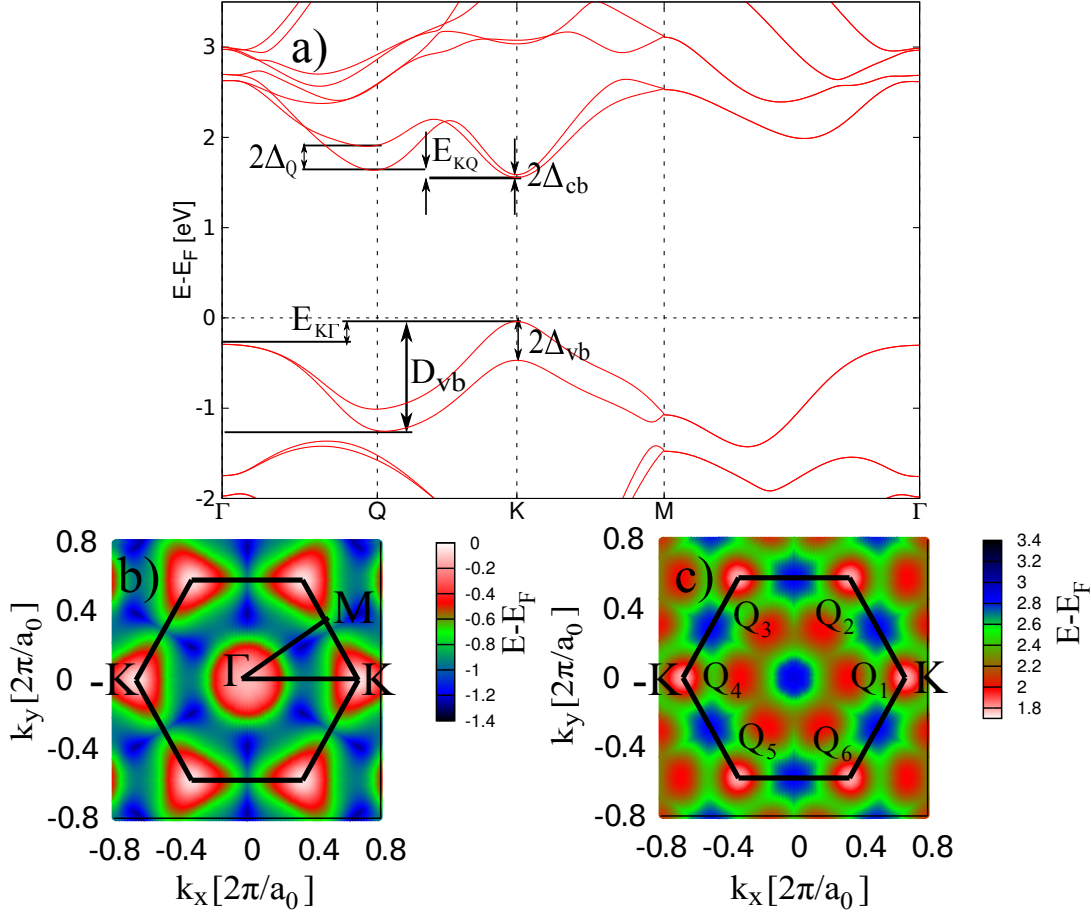


**Figure 2.** Overview of the band structure of monolayer TMDCs as obtained from DFT calculations. a) Dispersion along the  $\Gamma$ - $K$ - $M$ - $\Gamma$  line in the BZ. SOC is taken into account. Various band-edge energy differences and spin-splittings are also indicated; for definitions see the main text. b) Dispersion of the VB as a function of the wavevector  $\mathbf{k}$  in the whole BZ. The hexagonal BZ is denoted by thick black lines. c) The same as b) for the CB. In b) and c) SOC is neglected.

these points by  $Q_i$ ,  $i = 1 \dots 6$ . They can be found roughly half way between the  $K$  ( $-K$ ) and the  $\Gamma$  points. The spin-splitting of the CB at  $Q_i$  given by  $2\Delta_Q$ . The importance of the  $Q_i$  points depends, amongst other things, on the energy difference between the bottom of the CB at the  $K$  and  $Q_i$  points. This energy difference is denoted by  $E_{KQ}$ . Looking at the VB now, the energy difference between the top of the VB at  $K$  and  $\Gamma$  is denoted by  $E_{K\Gamma}$ . Finally, since it is directly available in recent ARPES measurements [106, 107, 108], we also record the width of the VB, which we define as the energy difference between the maximum of the VB at  $K$  and the minimum that can be found on the  $\Gamma$ - $K$  line.

Certain properties of TMDCs are easier to understand if one considers which atomic orbitals contribute to a given band at a given  $\mathbf{k}$ -space point. For example, as pointed out in, e.g., References [26, 36, 37, 109], the different atomic orbital composition can explain the difference in the spin-splitting magnitude of the CB and VB at the  $K$  point.



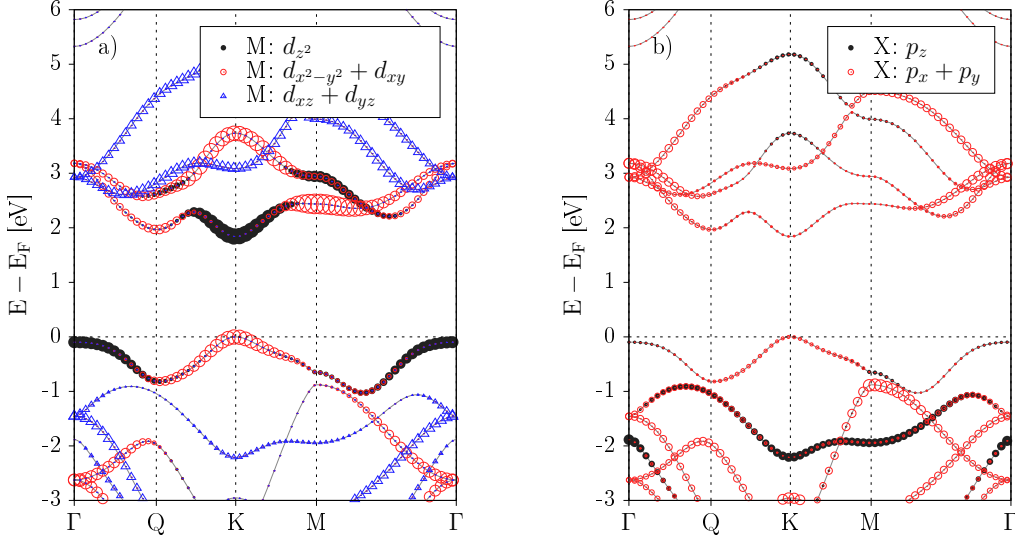


**Figure 3.** Atomic orbital weights in the energy bands of  $\text{MX}_2$ . a)  $d$  orbitals of the metal atom, and b)  $p$  orbitals of the chalcogen atoms. The size of each symbol is proportional to the weight of the atomic orbital. SOC was neglected in these calculations.

Furthermore, the atomic orbital composition of the energy bands underlies the tight-binding modelling of TMDCs [26, 32, 33, 35] and was also important in developing the  $\mathbf{k} \cdot \mathbf{p}$  model [49, 60]. The contribution of individual atomic orbitals to a given band is shown in Figure 3 for the  $d$  orbitals of the metal atoms and the  $p$  orbitals of the chalcogens (the weights of other atomic orbitals are much smaller). Comparing Figures 3(a) and (b) we find that in general more than one type of atomic orbital contributes to both the CB and the VB and the weight of the atomic orbitals changes throughout the BZ. Setting up a consistent tight-binding model for TMDCs is therefore more difficult than is the case for, e.g., graphene.

#### 4. Valence band width $D_{\text{vb}}$

An observable that can be directly compared to experimental ARPES measurements [106, 107, 108] is the width of the VB  $D_{\text{vb}}$ . In order to be able to compare the experimental and theoretical results, we define  $D_{\text{vb}}$  to be the difference between the top of the VB at the  $K$  point and the minimum, which lies between the  $\Gamma$  and  $K$  points: see Figure 2. (Note that the absolute minimum of the VB is not at this  $\mathbf{k}$ -space point. However, Reference [107] shows the dispersion only between  $\Gamma$  and  $K$ ; therefore we use the definition of  $D_{\text{vb}}$  given above.) Comparison between the calculated and experimental values is given in Table 2.

In the case of  $\text{MoS}_2$ , Reference [106] reported that the VB is narrower than the calculated one by  $\approx 10\%$ , whereas for  $\text{MoSe}_2$  [107] the opposite seems to be true.

**Table 2.** The width of the VB as obtained from DFT calculations. Experimental values are shown in the row denoted by “Exp”.

$D_{\text{vb}}$ [eV]	MoS <sub>2</sub>	MoSe <sub>2</sub>	WS <sub>2</sub>	WSe <sub>2</sub>	MoTe <sub>2</sub>	WTe <sub>2</sub>
(HSE,LDA)	0.911	0.84	1.215	1.132	0.657	0.933
(PBE,PBE)	0.896	0.84	1.207	1.136	0.688	0.965
Exp	$\approx 0.8^{\text{a}}$ , $\approx 0.9\text{--}1.0^{\text{b}}$	$\approx 1.0^{\text{c}}$				

<sup>a</sup>[106], exfoliated samples on a SiO substrate.

<sup>b</sup>[108], samples grown by chemical vapour deposition on a highly oriented pyrolytic graphite (HOPG) substrate.

<sup>c</sup>[107], samples grown by molecular beam epitaxy (MBE) on bilayer graphene on top of SiC (0001).

Reference [106] also provides a comparison between calculations and the ARPES band structures of bilayer, trilayer and bulk MoS<sub>2</sub>, showing a better agreement than is found for monolayer MoS<sub>2</sub>. Furthermore, a good agreement between DFT calculations and ARPES measurements for the VB was observed for bulk MoS<sub>2</sub> and MoSe<sub>2</sub> [62, 110] and for MoTe<sub>2</sub> [62]. The orbital composition of the VB away from the  $K$  point is not purely of Mo  $d$  orbital type:  $p$  orbitals of X atoms are also admixed (see Figure 3); hence  $D_{\text{vb}}$  in monolayers can be sensitive to interactions with substrates, which are not considered in our calculations and which might explain some of the differences with respect to measurements.

## 5. Effective model at the $K$ and $-K$ points

### 5.1. $K$ and $-K$ points

The physics around the  $K$  and  $-K$  points has attracted the most attention both experimentally and theoretically so far. This is mainly due to the exciting optical properties of these materials at the direct band gap, which can be found at the  $K$  and  $-K$  points. Moreover, it turns out that the effect of SOC is strong at this BZ point, leading to spin-split and spin-polarized bands. Since the  $K$  and  $-K$  points are connected by time-reversal symmetry, the polarization of the bands has to be opposite at  $K$  and  $-K$ , i.e., the spin and the valley degrees of freedom are coupled [26]. We start our discussion in Section 5.2 with a basic characterization of the band structure in terms of effective masses and spin-splittings. Then, in Section 5.3, a detailed  $\mathbf{k} \cdot \mathbf{p}$  theory is presented which captures the salient features of the DFT band structure and allows us to interpret the results of recent experiments [111, 112, 113, 114, 115].

### 5.2. Basic characterization and material parameters

The aim of this section is twofold. First, we want to point out that there is a difference between the MoX<sub>2</sub> and WX<sub>2</sub> materials regarding the sign of the SOC constant in the

CB (for a microscopic explanation see References [34], [36] and [49]). This difference is important for the interpretation of experiments in which properties of A and B excitons [27, 30] are compared (for introduction to exciton physics see e.g., [116]). Second, we report effective masses and spin-splittings extracted from our DFT calculations and compare them to experimental results, where available; see Tables 3 and 4.

One of the phenomena that first sparked strong interest in monolayer TMDCs was the pronounced effect of SOC on the VB around the  $K$  and  $-K$  points. SOC leads to the spin-splitting and spin-polarization of the VB and the energy scale associated with SOC is several hundreds of meVs: see Table 4. SOC in the VB was first studied using DFT calculations [109, 117, 118, 119], but it can be readily understood using, e.g., a tight-binding model and first-order perturbation theory [26, 36, 37]. An experimental signature of the spin-splitting of the VB is the energy difference of the A and B excitons [27, 30].

SOC also affects the CB. This was initially neglected, mainly because in  $\text{MoS}_2$ , which is the most widely studied of the TMDCs, it is indeed a small effect and it was assumed that the situation would be similar in other monolayer TMDCs. In general the magnitude of the spin-splitting of the CB is only 7–10% of that of the VB, with the exception of  $\text{MoS}_2$ , where it is only  $\approx 2\%$ : see Table 3. However, in absolute terms it is an energy scale that can be important at low temperatures and in ballistic samples. Note that the SOC in the CB at the  $K$  point is a more subtle effect than in the VB. In the simplest theoretical approximation, which assumes that it is sufficient to consider only the  $d_{z^2}$  atomic orbitals of the metal atoms, the SOC vanishes. DFT calculations, on the other hand, indicate that there is a finite spin-splitting in the CB at the  $K$  point [60, 109, 117, 118, 119].

As it turns out, the SOC in the CB can be understood in terms of a competition between two contributions [34, 36, 49, 60, 120]: i) a first-order contribution from the chalcogen atoms, which have a small, but finite weight [34, 37] and ii) a second-order contribution due to the coupling to other bands [34, 36, 49, 60], where the  $d_{xz}$  and  $d_{yz}$  atomic orbitals have large weights; see Figure 3. Due to this competition the spin-polarisation of the spin-split CBs is different in  $\text{MoX}_2$  and  $\text{WX}_2$ . Our latest results were obtained using the FLEUR code, which allows the explicit calculation of the spin expectation value  $\langle s_z \rangle$  in a given band. We find that the spin-split CB with  $\langle s_z \rangle > 0$  ( $\langle s_z \rangle < 0$ ) is higher (lower) in energy in  $\text{MoX}_2$ , while the opposite is true for  $\text{WX}_2$ : see Figures 4(a) and 4(b), in which the CBs of  $\text{MoSe}_2$  and  $\text{WSe}_2$  are shown, respectively. By contrast, as shown in Figures 4(c) and 4(d), in the VB the sign of  $\langle s_z \rangle$  is the same for both  $\text{MoX}_2$  and  $\text{WX}_2$ . Furthermore, as can be seen in Figures 4(a) and 4(b), the band with the lighter effective mass is lower in energy for  $\text{MoX}_2$ , leading to band crossing of the two spin-split bands in the vicinity of the  $K$  and  $-K$  points [34, 36, 49], whereas for  $\text{WX}_2$  the lighter spin-split band is higher in energy and therefore there is no band crossing. ( $\text{MoTe}_2$  is somewhat special in that the crossing of the spin-split bands on the  $\Gamma$ - $K$  line is absent. The other band crossing, on the  $K$ - $M$  line, is present). These differences notwithstanding, there is a spin-valley coupling in the CB similar to the VB. In Figure

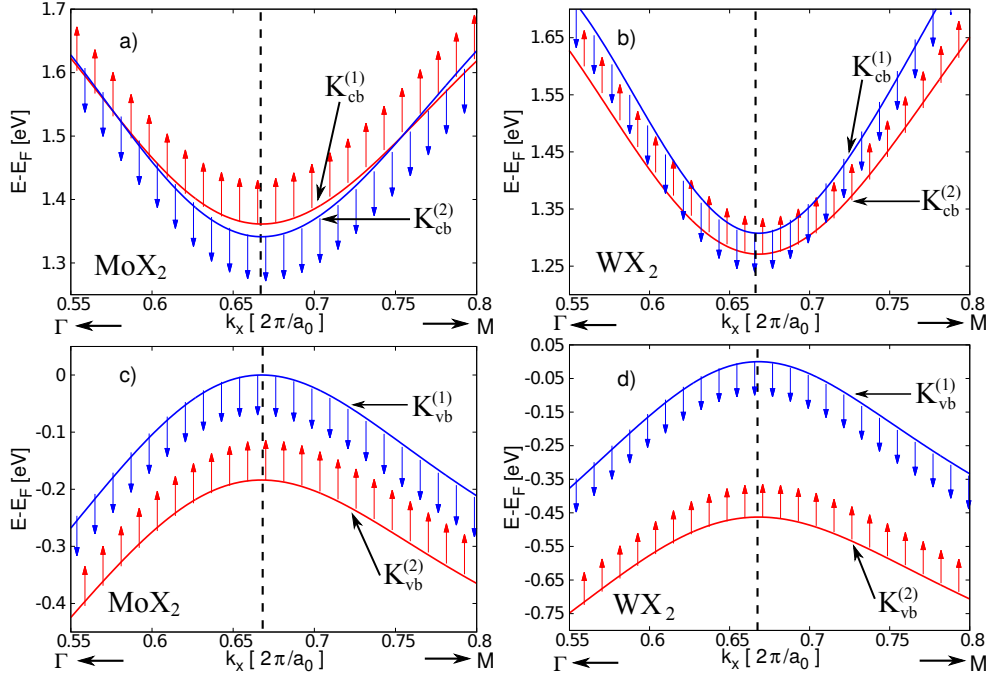


**Figure 4.** Spin polarisation and dispersion of the spin-split CB and VB in the vicinity of the  $K$  point from DFT calculations. Arrows show the direction of the spin expectation values (red: spin-up, blue: spin-down). a) and c) results for  $\text{MoX}_2$ ; b) and d) results for  $\text{WX}_2$ . Note that the order of spin-up and spin-down bands in the CB is different for  $\text{MoX}_2$  and  $\text{WX}_2$ . The vertical dashed line shows the position of the  $K$  point. The actual calculations were performed for  $\text{MoSe}_2$  and  $\text{WSe}_2$  using the “(PBE,PBE)” approach.

4 we also introduce the notation  $K_{\text{vb}}^{(1)}$  ( $K_{\text{vb}}^{(2)}$ ) for the higher-in-energy (lower-in-energy) spin-split VB, and similarly for the CB. As a consequence of the spin polarisation of the bands in optical experiments the lowest-energy spin-allowed transition is  $K_{\text{vb}}^{(1)} \rightarrow K_{\text{cb}}^{(2)}$  for  $\text{MoX}_2$  and  $K_{\text{vb}}^{(1)} \rightarrow K_{\text{cb}}^{(1)}$  for  $\text{WX}_2$ . We note that very recently the first spin-resolved ARPES measurement on bulk  $\text{WSe}_2$  has appeared [121] and seems to indicate an out-of-plane spin polarisation of the spin-split VB around  $K$  and  $-K$  points. Assuming that the measurements predominantly probe the top layer [121], i.e., effectively a monolayer sample, they are in agreement with the DFT calculations presented here.

The dispersion around the  $K$  and  $-K$  points is not simply parabolic [60], which has to be borne in mind when fitting the band structure to obtain the effective masses and other band parameters. This can already be appreciated in Figures 2(b) and (c), where a trigonal warping (TW) of the dispersion around the  $K$  and  $-K$  points can clearly be seen. The TW is more pronounced in the VB than in the CB. In the simplest approximation this can be taken into account by a cubic term in the dispersion. Therefore the dispersion of each spin-split band in the VB and the CB can be described by

$$E_K(\mathbf{q}) = \frac{\hbar^2 \mathbf{q}^2}{2m_{\text{eff}}} + C_{3w} |\mathbf{q}|^3 \cos(3\varphi_{\mathbf{q}}), \quad (1)$$

where the wavevector  $\mathbf{q} = (q_x, q_y)$  is measured from the  $K$  point,  $\varphi_{\mathbf{q}} = \arctan(q_y/q_x)$ ,  $m_{\text{eff}}$  is the effective mass of the given band, and  $C_{3w}$  is a parameter describing the TW. The derivation of  $E_K(\mathbf{q})$  based on a multi-band  $\mathbf{k} \cdot \mathbf{p}$  model is presented in Section 5.3 and Appendix A. We note that a similar model was recently used in Reference [122].

The values of the  $m_{\text{eff}}$  and  $C_{3w}$  that we have extracted from our DFT calculations for each band and material are given in Tables 3 and 4. We note that several works have already presented tables of, e.g., effective masses [43, 45, 81, 123, 124, 125, 126] for different monolayer TMDCs. However, the effects of SOC have often been neglected leading to, e.g., the conclusion that the effective masses of the spin-split VBs are the same. Recent experimental evidence shows that this is not the case [107, 193]. Moreover, due to the presence of the TW, some care has to be taken when defining the effective mass and, especially, when choosing the fitting range that is used to obtain it from a DFT band structure. All our DFT band-structure calculations were performed along the  $\Gamma$ – $K$ – $M$  line in the BZ. We first fitted  $m_{\text{eff}}$ , i.e., we set  $C_{3w} = 0$  in Equation (1). The fitting range corresponded to 5% of the  $\Gamma$ – $K$  distance. The dispersion over such range was considered to be isotropic and the difference in the effective masses along  $K$ – $\Gamma$  and  $K$ – $M$  was neglected. Therefore the effective masses shown in Tables 3 and 4 characterise, strictly speaking, a rather narrow vicinity of the band edge. The non-parabolicity of the band structure and the trigonal distortion of the constant energy contours, described by the second term in Equation (1), was taken into account in a second step, whereby Equation (1) was fitted over a wider range (typically  $\approx 10\%$  of the  $\Gamma$ – $K$  distance), but  $m_{\text{eff}}$ , obtained in the previous step, was kept fixed. This two-step fitting was needed to obtain coherent parameter sets between the simple approach outlined here and a more accurate model presented in Section 5.3. Further details of the fitting procedure are discussed in Appendix B. Looking at Tables 3 and 4 one can see that the effective masses and spin-splittings obtained from the two different DFT calculations are in almost perfect agreement, while there are some differences in the extracted values of  $C_{3w}$ .

Considering first the CB, the extracted band parameters and SOC splittings  $2\Delta_{\text{cb}}$  for different monolayer TMDCs are shown in Table 3. To our knowledge there are no direct measurements of  $\Delta_{\text{cb}}$  or  $m_{\text{cb}}$  for any of these materials yet; therefore it is difficult to tell how reliable these DFT-based predictions are. In addition we show the charge density  $n_{\text{cb}}$  at which the upper spin-split CB  $K_{\text{cb}}^{(1)}$  starts to be populated. This charge density is calculated using the effective mass of the  $K_{\text{cb}}^{(2)}$  band given in Table 3 and assuming a simple parabolic dispersion (i.e., neglecting  $C_{3w}$ ), which is a good approximation in the CB. Note that typical charge densities achieved by gating in MoS<sub>2</sub> are reported to be  $\sim 4 \cdot 10^{12} \text{ cm}^{-2}$ – $3.6 \cdot 10^{13} \text{ cm}^{-2}$  [127], a few times  $10^{12} \text{ cm}^{-2}$  for monolayer samples [128] and few-layer samples [129]), and up to  $10^{14} \text{ cm}^{-2}$  in few-layer WS<sub>2</sub> using ionic liquid gating [130].

Turning now to the VB, the band parameters and SOC splitting  $2\Delta_{\text{vb}}$  obtained from our DFT calculations are shown in Table 4. In the case of MoSe<sub>2</sub>, very recent high-resolution ARPES measurements [107] allow for a direct comparison with the

**Table 3.** Band dispersion parameters and spin-splittings at the  $K$  and  $-K$  points in the CB from DFT calculations.  $m_{\text{cb}}^{(1)}$  ( $m_{\text{cb}}^{(2)}$ ) is the effective mass of the  $K_{\text{cb}}^{(1)}$  ( $K_{\text{cb}}^{(2)}$ ) band, and similarly for  $C_{3w}^{(1)}$  ( $C_{3w}^{(2)}$ ).  $m_e$  is the free electron mass.  $n_{\text{cb}}$  is the electron density above which the upper spin-split CB starts to fill.

	MoS <sub>2</sub>	MoSe <sub>2</sub>	WS <sub>2</sub>	WSe <sub>2</sub>	MoTe <sub>2</sub>	WTe <sub>2</sub>
$m_{\text{cb}}^{(1)}/m_e$ (HSE,LDA)	0.46	0.56	0.26	0.28	0.62	0.26
$m_{\text{cb}}^{(1)}/m_e$ (PBE,PBE)	0.47	0.58	0.27	0.29	0.61	0.25
$m_{\text{cb}}^{(2)}/m_e$ (HSE,LDA)	0.43	0.49	0.35	0.39	0.53	0.39
$m_{\text{cb}}^{(2)}/m_e$ (PBE,PBE)	0.44	0.50	0.36	0.40	0.51	0.38
$C_{3w}^{(1)}$ [eVÅ <sup>3</sup> ] (HSE,LDA)	-3.36	-3.11	-2.8	-3.02	-3.85	-5.86
$C_{3w}^{(1)}$ [eVÅ <sup>3</sup> ] (PBE,PBE)	-3.57	-2.94	-1.8	-2.44	-3.95	-17.54
$C_{3w}^{(2)}$ [eVÅ <sup>3</sup> ] (HSE,LDA)	-3.34	-3.12	-3.14	-3.23	-3.86	-4.90
$C_{3w}^{(2)}$ [eVÅ <sup>3</sup> ] (PBE,PBE)	-3.49	-2.86	-2.54	-2.97	-4.04	-9.67
$2\Delta_{\text{cb}}$ [meV] (HSE,LDA)	3	22	-32	-37	36	-52
$2\Delta_{\text{cb}}$ [meV] (PBE,PBE)	3	20	-31	-37	32	-54
$n_{\text{cb}}$ [10 <sup>12</sup> cm <sup>-2</sup> ] (HSE,LDA)	0.54	4.5	4.68	6.03	7.97	8.48

calculations, because the difference between the effective masses of  $K_{\text{vb}}^{(1)}$  and  $K_{\text{vb}}^{(2)}$  could be directly observed. We show two theoretical values for the effective masses in the VB of MoSe<sub>2</sub>. The first one is obtained using the fitting procedure described above, i.e., by averaging the values along the  $K$ - $\Gamma$  and  $K$ - $M$  directions. The second value, shown in parenthesis, is obtained by following the fitting procedure that was used for the experimental data [131]. This latter procedure involves fitting only along the  $K$ - $\Gamma$  direction, and a fitting range of  $\approx 13\%$  of the  $K$ - $\Gamma$  distance. One can see that the theoretical and experimental effective masses that were obtained using the same fitting range are in good agreement. Moreover, the calculated value of  $2\Delta_{\text{vb}}$  also corresponds rather well to the measured one. MoS<sub>2</sub> is the only other monolayer TMDC for which ARPES measurements are available to extract the effective mass. However, the ARPES data of Reference [132] do not resolve  $K_{\text{vb}}^{(1)}$  and  $K_{\text{vb}}^{(2)}$  separately; therefore the reported effective mass is the average of  $m_{\text{vb}}^{(1)}$  and  $m_{\text{vb}}^{(2)}$ . Taking into account the experimental uncertainty, our results are in reasonable agreement with the measurements of Reference [132]. The available data for MoS<sub>2</sub>, MoSe<sub>2</sub> and WSe<sub>2</sub> suggest that DFT can capture the VB effective masses quite well even without  $GW$  corrections, such as those found in Reference [47]. For the other three monolayers, to our knowledge, no ARPES data are yet available.

In optical experiments the difference of the A and B exciton energies are usually identified with  $2\Delta_{\text{vb}}$  providing the results shown in Table 4. We note that there are two assumptions behind the identification of the A and B exciton energy difference with  $2\Delta_{\text{vb}}$ : i) that the spin-splitting in the CB is negligible and ii) that the binding energies of the A and B excitons are the same. Regarding i), one can see in Table 3 that  $\Delta_{\text{cb}}$  is small,

**Table 4.** Effective masses and spin-splittings at the  $K$  point in the VB from DFT calculations.  $m_{\text{vb}}^{(1)}$  ( $m_{\text{vb}}^{(2)}$ ) is the effective mass of the  $K_{\text{vb}}^{(1)}$  ( $K_{\text{vb}}^{(2)}$ ) band, and similarly for  $C_{3w}^{(1)}$  ( $C_{3w}^{(2)}$ ).  $m_e$  is the free electron mass. The values in brackets were obtained using a slightly different fitting range, as explained in the text. Experimental values are shown in rows denoted by “Exp”.

	MoS <sub>2</sub>	MoSe <sub>2</sub>	WS <sub>2</sub>	WSe <sub>2</sub>	MoTe <sub>2</sub>	WTe <sub>2</sub>
$m_{\text{vb}}^{(1)}/m_e$ (HSE,LDA)	-0.54	-0.59 (-0.64)	-0.35	-0.36	-0.66	-0.34
$m_{\text{vb}}^{(1)}/m_e$ (PBE,PBE)	-0.54	-0.60 (-0.60)	-0.36	-0.36	-0.62	-0.32
Exp	$-0.6 \pm 0.08^a$	$-0.67 \pm 0.4^b$		$-0.35 \pm 0.01^z$		
$m_{\text{vb}}^{(2)}/m_e$ (HSE,LDA)	-0.61	-0.7 (-0.72)	-0.49	-0.54	-0.82	-0.58
$m_{\text{vb}}^{(2)}/m_e$ (PBE,PBE)	-0.61	-0.7 (-0.69)	-0.50	-0.54	-0.77	-0.54
Exp	$-0.6 \pm 0.08^a$	$-0.75 \pm 0.3^b$		$-0.49 \pm 0.05^z$		
$C_{3w}^{(1)}$ [eVÅ <sup>3</sup> ] (HSE,LDA)	6.16	5.67	4.59	6.47	5.44	6.77
$C_{3w}^{(1)}$ [eVÅ <sup>3</sup> ] (PBE,PBE)	6.08	5.21	6.07	5.79	5.46	17.61
$C_{3w}^{(2)}$ [eVÅ <sup>3</sup> ] (HSE,LDA)	5.78	5.42	5.50	5.18	5.14	4.83
$C_{3w}^{(2)}$ [eVÅ <sup>3</sup> ] (PBE,PBE)	5.71	5.064	5.04	4.78	5.09	9.08
$2\Delta_{\text{vb}}$ [meV] (HSE,LDA)	148	186	429	466	219	484
$2\Delta_{\text{vb}}$ [meV] (PBE,PBE)	148	184	425	462	213	480
Exp [meV]	$\approx 140^c$ $\approx 150^d$ $160^m$ $140^n$ $140^p$ $138^r$	$\approx 180^e$ $\approx 180^f$ $\approx 200^m$	$\approx 400^g$ , $380^h$ $410^i$ $400^j$ $400^l$ $400^l$ $379^r$ $391^t$	$\approx 400^g$ $\gtrsim 460^k$ $400^l$ $510^m$ $\sim 500^q$ $404^r$ $412^t$ $430^x$ $513^z$	$250^y$	

<sup>a</sup>[132], sodium intercalated sample and ARPES measurement.

<sup>b</sup>Private communication by Yi Zhang based on ARPES measurements; see [107].

<sup>c</sup>[27], <sup>f</sup>[133], <sup>i</sup>[134], <sup>j</sup>[135], <sup>l</sup>[136], <sup>r</sup>[137], from differential reflectance.

<sup>e</sup>[107], from ARPES measurement.

<sup>d</sup>[138], <sup>g</sup>[139], <sup>p</sup>[140], from photoluminescence.

<sup>h</sup>[141], from differential transmission.

<sup>k</sup>[23], from electroluminescence.

<sup>m</sup>[142], from photocurrent spectroscopy of suspended samples.

<sup>n</sup>[143], from absorbance measurement.

<sup>q</sup>[121], from spin-resolved ARPES measurement.

<sup>t</sup>[144], from reflectivity measurement.

<sup>x</sup>[145], from linear absorption.

<sup>y</sup>[192], from reflectance measurements.

<sup>z</sup>[193], ARPES measurement.

but finite, and for quantitative comparisons between theory and experiment it should not be neglected. As for ii), we note that the binding energy of the A and B excitons

depends on their reduced mass, which, according to Table 4, should be different for the different exciton species. With these caveats the agreement between the calculations and the experiments is qualitatively good, especially for MoS<sub>2</sub> and MoSe<sub>2</sub>.

Comparing the DFT-calculated effective masses in Tables 3 and 4 for the VBs and CBs that have the same spin-polarisation, one can observe that there is no electron–hole symmetry in the band structure. The first experimental evidence to support this observation, coming from magnetoluminescence experiments, has appeared very recently [112, 113, 114, 115, 195]. Regarding the experimental relevance of TW, it has been argued [111] that it leads to measurable effects in the polarisation of electroluminescence in p–n junctions. We note that due to the heavier effective mass in the VB and the larger values of  $C_{3w}$ , the TW is more pronounced in our DFT calculations in the VB than in the CB. In the latter a simple parabolic approximation is often adequate.

We finish Section 5.2 with a brief discussion of the quasiparticle band gap  $E_{\text{bg},K}$ , which we define as the difference between the maximum of the  $K_{\text{vb}}^{(1)}$  and  $K_{\text{cb}}^{(2)}$  bands at the  $K$  and  $-K$  points. DFT calculations for monolayer TMDCs underestimate the band gap (see Table 5) and its evaluation requires the use of  $GW$  methodology [45, 46, 47, 81, 117]. Experimental evidence that supports the conclusions of the  $GW$  calculations is now also emerging. Apart from its fundamental importance, the main reason for discussing  $E_{\text{bg},K}$  and showing our DFT results is that  $E_{\text{bg},K}$  enters into the fitting procedure that we use to obtain the parameters of the  $\mathbf{k} \cdot \mathbf{p}$  Hamiltonian that describes the dispersion in the vicinity of the band edge. The details of the  $\mathbf{k} \cdot \mathbf{p}$  model and the fitting procedure are given in Section 5.3 and Appendix B. As one can see, our DFT calculations significantly underestimate the experimental quasiparticle band gaps. We also note that in heavily doped samples, which were used in the ARPES measurements [107, 132], the observed band gap is reduced with respect to results obtained by other methods [24, 135, 142, 146], hinting at the crucial importance of screening in monolayer TMDCs.

### 5.3. $\mathbf{k} \cdot \mathbf{p}$ Hamiltonian

We now present a low-energy effective  $\mathbf{k} \cdot \mathbf{p}$  Hamiltonian that describes the coupled dynamics of the VB and CB. Part of the theory was previously discussed in References [60] and [49]; in the present work we both overview and extend these earlier results.

To obtain a model that captures the most important features of the dispersion of the VB and CB one can start from a seven-band model, which was introduced in Reference [60, 49]; motivation and details of the model are given in Appendix A. An effective low-energy Hamiltonian can be derived from the seven-band model by systematically eliminating all degrees of freedom other than the ones corresponding to the VB and CB using Löwdin partitioning [150]. We keep terms up to third order in the off-diagonal coupling elements of the original seven-band model and use the spinful basis  $\{|\Psi^{\text{vb}}, s\rangle, |\Psi^{\text{cb}}, s\rangle\}$ , where  $|\Psi^{\text{vb}}\rangle$  ( $|\Psi^{\text{cb}}\rangle$ ) are spinless Bloch wave functions in the VB (CB) and  $|\Psi^{\text{b}}, s\rangle = |\Psi^{\text{b}}\rangle \otimes |s\rangle$ , with  $\text{b} = \{\text{cb}, \text{vb}\}$  and  $s = \{\uparrow, \downarrow\}$  denoting the band spin



**Table 5.** Band gap  $E_{\text{bg},K}$  at the  $K$  point from DFT calculations, from  $GW$  calculations, and from measurements.  $E_{\text{bg},K}$  is defined as the energy difference between the bands  $K_{\text{vb}}^{(1)}$  and  $K_{\text{cb}}^{(2)}$  at  $K$ . The  $GW$  “flavour” used in the calculations is also shown. Experimental values are shown in rows denoted by “Exp”. All values are in eV.

	MoS <sub>2</sub>	MoSe <sub>2</sub>	WS <sub>2</sub>	WSe <sub>2</sub>	MoTe <sub>2</sub>	WTe <sub>2</sub>
(HSE,LDA)	1.67	1.40	1.60	1.30	0.997	0.792
(PBE,PBE)	1.59	1.34	1.58	1.27	0.947	0.765
$GW$	2.84 <sup>h</sup>	2.41 <sup>l,m</sup>	2.88 <sup>l,q</sup>	2.42 <sup>l</sup>	1.77 <sup>l</sup>	1.77 <sup>q</sup>
	2.76 <sup>j,q</sup>	2.26 (2.13) <sup>n</sup>	2.70 <sup>p</sup>	2.38 <sup>q</sup>	1.79 <sup>m</sup>	1.79 <sup>x</sup>
	2.80 <sup>k</sup>	2.33 <sup>q</sup>	3.11 <sup>k</sup>	2.51 <sup>x</sup>	1.82 <sup>q</sup>	
	2.82 <sup>l</sup>	2.31 <sup>x</sup>	2.91 <sup>x</sup>		1.77 <sup>x</sup>	
	2.97 <sup>m</sup>					
Exp	2.5 <sup>a</sup>	2.18 <sup>b</sup>	2.14 <sup>c</sup>	2.51 ± 0.04 <sup>r</sup>		
	2.14 ± 0.08 <sup>g</sup>	2.02 <sup>s</sup> , 2.22 <sup>s</sup>	2.41 <sup>d</sup>	2.0 <sup>s</sup> , 2.18 <sup>s</sup>		
Exp (ARPES)	1.86 <sup>e</sup>	1.58 <sup>f</sup>				

<sup>a</sup>[142], photocurrent spectroscopy on suspended samples, lower bound.

<sup>b</sup>[146], scanning-tunnelling experiments, on bilayer graphene substrate.

<sup>c</sup>[24], transport measurements using ionic liquid gating.

<sup>d</sup>[135], differential reflectance, on SiO<sub>2</sub> substrate.

<sup>e</sup>[132], <sup>f</sup>[107], from ARPES, heavily doped sample.

<sup>g</sup>[151], <sup>s</sup>[152], scanning-tunnelling experiments, on graphite substrate.

<sup>r</sup>[153], scanning-tunnelling experiments.

<sup>h</sup>[47],  $G_1W$ .

<sup>j</sup>[117], quasiparticle self-consistent  $GW$ .

<sup>k</sup>[81], self-consistent  $GW_0$ .

<sup>l</sup>[45], <sup>m</sup>[46], <sup>q</sup>[147], <sup>x</sup>[101],  $G_0W_0$  method.

<sup>n</sup>[146],  $G_1W$ , without (with) substrate screening taken into account.

<sup>p</sup>[134],  $G_1W$ .

degree of freedom, respectively. One finds that the low-energy effective Hamiltonian

$$H_{\text{eff}}^{\tau,s} = H_0 + H_{\mathbf{k}\cdot\mathbf{p}}^{\tau,s} + H_{\text{so}}^{\tau,s} \quad (2)$$

is the sum of the following terms:

- i) The free-electron term  $H_0 = \frac{\hbar^2 \mathbf{q}^2}{2m_e} (\mathbb{1}_2 \otimes s_z)$ , where  $\mathbb{1}_2$  is a unit matrix in the electron–hole space,  $s_z$  is a spin Pauli matrix, and  $m_e$  is the free electron mass. Here and in Equations (4b)–(4f) the wavevector  $\mathbf{q} = (q_x, q_y)$  is measured from the  $K$  or  $-K$  points. We note that  $H_0$  is usually neglected in the GaAs literature on account of the light effective mass in this material, but here we want to keep it.
- ii) The SOC Hamiltonian  $H_{\text{so}}^{\tau,s}$ , which contains the diagonal and  $\mathbf{q}$ -independent contributions of the SOC. It reads

$$H_{\text{so}}^{\tau,s} = \begin{pmatrix} \tau \Delta_{\text{vb}} s_z & 0 \\ 0 & \tau \Delta_{\text{cb}} s_z \end{pmatrix}, \quad (3)$$

i.e., it is diagonal in spin space and is proportional to the Pauli matrix  $s_z$  (for further details see Appendix A).  $H_{\text{so}}^{\tau,s}$  describes the spin-splittings of the CB and the VB, which are due to the absence of inversion symmetry in monolayer TMDCs. Since  $H_{\text{so}}^{\tau,s}$  is diagonal, one can also write it in terms of the eigenvalues  $s = \pm 1$  of  $s_z$ ; we will use the two notations interchangeably. Moreover, the index  $\tau = 1$  ( $\tau = -1$ ) denotes the valley  $K$  ( $-K$ ). Where it is more convenient, we will also use the matrix  $\tau_z$  which acts in the valley space. In the VB, the parameter  $\Delta_{\text{vb}}$  that describes the strength of the SOC can always be taken to be positive. As explained in Section 5.2, the situation is more complicated in the CB [34, 49, 36], because DFT calculations show that, in the case of  $\text{MoX}_2$ , the spin-split bands cross close to the  $K$  and  $-K$  points, while there is no such band crossing for  $\text{WX}_2$ . This can be understood in terms of  $\Delta_{\text{cb}}$  having opposite signs in  $\text{MoX}_2$  and  $\text{WX}_2$ .

iii) Finally, the  $\mathbf{k} \cdot \mathbf{p}$  Hamiltonian  $H_{\mathbf{k},\mathbf{p}}^{\tau,s}$  in Equation (2) is given by

$$H_{\mathbf{k},\mathbf{p}}^{\tau,s} = H_{\text{D}}^{\tau,s} + H_{\text{as}}^{\tau,s} + H_{3w}^{\tau,s} + H_{\text{cub}}^{\tau,s}, \quad (4a)$$

where

$$H_{\text{D}}^{\tau,s} = \begin{pmatrix} \varepsilon_{\text{vb}} & \tau \cdot \gamma_{\tau,s} q_-^\tau \\ \tau \cdot \gamma_{\tau,s}^* q_+^\tau & \varepsilon_{\text{cb}} \end{pmatrix}, \quad (4b)$$

$$H_{\text{as}}^{\tau,s} = \begin{pmatrix} \alpha_{\tau,s} \mathbf{q}^2 & 0 \\ 0 & \beta_{\tau,s} \mathbf{q}^2 \end{pmatrix}, \quad (4c)$$

$$H_{3w}^{\tau,s} = \begin{pmatrix} 0 & \kappa_{\tau,s} (q_+^\tau)^2 \\ \kappa_{\tau,s}^* (q_-^\tau)^2 & 0 \end{pmatrix}, \quad (4d)$$

$$H_{\text{cub},1}^{\tau,s} = -\tau \frac{1}{2} \mathbf{q}^2 \begin{pmatrix} 0 & \eta_{\tau,s} q_-^\tau \\ \eta_{\tau,s}^* q_+^\tau & 0 \end{pmatrix}. \quad (4e)$$

$$H_{\text{cub},2}^{\tau,s} = -\tau \frac{\omega_s}{2} |\mathbf{q}|^3 \cos(3\varphi_{\mathbf{q}}) \begin{pmatrix} 1 & 0 \\ 0 & 1 \end{pmatrix}. \quad (4f)$$

Here  $q_\pm^\tau$  is defined as  $q_\pm^\tau = q_x \pm i\tau q_y$ ,  $\varphi_{\mathbf{q}} = \arctan(q_y/q_x)$ ,  $\varepsilon_{\text{vb}}$  and  $\varepsilon_{\text{cb}}$  are band-edge energies,  $\gamma_{\tau,s}$ ,  $\alpha_{\tau,s}$ ,  $\beta_{\tau,s}$ ,  $\kappa_{\tau,s}$ ,  $\eta_{\tau,s}$ , and  $\omega_s$  are material parameters discussed below.  $H_{\mathbf{k},\mathbf{p}}^{\tau,s}$  is a generalisation of the results given in Reference [60] for the case in which the material parameters depend on the SOC.

In general all off-diagonal material parameters appearing in  $H_{\mathbf{k},\mathbf{p}}^{\tau,s}$  are complex numbers such that for  $\tau = -1$  ( $-K$  valley) they are the complex conjugate of the  $\tau = 1$  ( $K$  valley) values. Concrete values of the material parameters for each  $\text{MX}_2$  material can be obtained by, e.g., fitting a DFT band structure, see Tables 6 and 7. Note however, that the fitting procedure (see Appendix B) yields real numbers for each parameter. We now briefly discuss each of the terms [Equations (4b)–(4f)].

- i) *Terms up to linear order in  $q_+$  and  $q_-$*  can be found in Equation (4b).  $H_{\text{D}}^{\tau,s}$  is basically the massive Dirac fermion model introduced in Reference [26]. It describes an isotropic dispersion around the band edge and it does not break the electron–hole

symmetry. The value of  $\gamma_{s,\tau}$  also depends on the SOC, but the Löwdin-partitioning calculations suggest that this dependence should be weak. This is indeed what we have found from fits to the DFT band structure. Therefore in the following we suppress both the spin index  $s$  and, since  $\gamma$  is taken to be a real number, the valley index  $\tau$ .

- ii) *Diagonal terms quadratic in  $q_+$  and  $q_-$*  are given in Equation (4c).  $H_{\text{as}}^{\tau,s}$  breaks the electron–hole symmetry because in general  $\alpha_{\tau,s} \neq \beta_{\tau,s}$ . The recent observation of photoluminescence peak splitting in magnetic fields [112, 114, 113, 115] suggests that electron–hole symmetry is indeed broken. Both  $\alpha_{\tau,s}$  and  $\beta_{\tau,s}$  can be written as, e.g.,  $\alpha_{\tau,s} = \alpha_0 + \tau \cdot s \cdot \tilde{\alpha}$  and hence  $\alpha_{\tau,s} = \alpha_{-\tau,-s}$ ,  $\beta_{\tau,s} = \beta_{-\tau,-s}$ .
- iii) *Off-diagonal terms quadratic in  $q_+$  and  $q_-$*  are given in Equation (4d).  $H_{3w}^{\tau,s}$ , in combination with  $H_{\text{D}}^{\tau,s}$ , leads to the TW of the energy contours that can be observed in Figures 2(b) and (c). [For further details see Equation (B.1) in Appendix B]. The TW is expected to play an important role in the explanation of recent electroluminescence experiments [111]. It may facilitate the generation of valley and spin currents that are second order in the applied bias [122]. Moreover, it was observed in ARPES measurements [108, 121].
- iv) *Off-diagonal terms cubic in  $q_+$  and  $q_-$*  appear in Equation (4e).  $H_{\text{cub},1}^{\tau,s}$  is important for obtaining a good fit to the DFT band structure away from the  $K$  point in a two-band model that describes the coupled dynamics of the VB and CB. They also play role when one uses the eigenvalues of Hamiltonian (2) to fit the DFT band structure in order to extract material parameters (see Tables 6 and 7 below). In particular, combined with the off-diagonal first-order terms, they contribute in second order in the wavenumber to the eigenvalues (for details see Appendix B).
- v) *Diagonal terms cubic in  $q_+$  and  $q_-$* . In some cases it is more convenient to work with a model that gives the dispersions of the VB and CB separately. Cubic terms in  $\mathbf{q}$  are needed to capture the non-parabolicity of the bands, and such a model is given by Equation (1). It can easily be obtained by applying Löwdin partitioning to Equation (2) and eliminating either the electron or the hole degrees of freedom. In this case, for consistency, the term  $H_{\text{cub},2}^{\tau,s}$  in Equation (4f) also has to be taken into account.

We note that, starting from a TB Hamiltonian, a model containing the terms (4b)–(4d) and the VB spin-splitting was also obtained in Reference [32].

In comparison to Equations (3) and (4b)–(4f), the widely used gapped Dirac Hamiltonian model introduced in Reference [26] contains only the terms linear in  $q$  and the spin-splitting in the VB. It can be written as

$$\tilde{H}_D = \gamma(\tau q_x \sigma_x + q_y \sigma_y) + \frac{E_{\text{bg}}}{2} \sigma_z + \Delta_{\text{vb}} \tau s_z \frac{\sigma_z - 1}{2}. \quad (5)$$

Here the Pauli matrices  $\sigma_{x,y,z}$  act in the electron–hole space. This simple model correctly captures the large spin-splitting of the VB, that the dispersion in the close vicinity of the  $K$  valley is quadratic, and predicts the valley-dependent optical selection rule [26]

in accordance with experiments [27, 28, 29]. However, the preceding discussion of the various terms in Equation (2) clearly indicates the limitations of Equation (5) in the interpretation of certain experimental results and DFT calculations: it cannot describe, for example, the spin-splitting of the CB, the electron–hole asymmetry and the trigonal warping of the spectrum.

The eigenstates and eigenvalues of the  $\mathbf{k} \cdot \mathbf{p}$  Hamiltonian (2) can also be used as a starting point for analytical calculation of the *Berry curvature* [148]. The Berry curvature is relevant for the quantum transport characteristics of TMDCs, such as the valley Hall effect [26] and weak localisation [154], while a related quantity, the spin Berry curvature [149], gives rise to a finite spin Hall conductivity for moderate hole doping.

Finally, we show the  $\mathbf{k} \cdot \mathbf{p}$  parameters obtained from fitting of the DFT band structure (see Tables 6 and 7) using the model that explicitly contains the coupling between the VB and the CB. In this case the diagonal cubic term [Equation (4f)] is not important for obtaining a good fit to the band structure and therefore the  $\omega_s$  parameter is not shown. Close to the band edge the  $\mathbf{k} \cdot \mathbf{p}$  parameters given in Tables 6 and 7 reproduce the effective masses shown in Tables 3 and 4. The details of the fitting procedure are given in Appendix B. Since the effective masses and  $C_{3w}$  parameters extracted from the (HSE,LDA) and (PBE,PBE) approaches are rather similar, we only show results that are based on (HSE,LDA) DFT band-structure calculations. Due to the SOC all parameters, with the exception of  $\gamma$ , are different for different spin indices  $s$ . Since the Hamiltonian of Equation (4a) is diagonal in the spin space, i.e., it describes the coupled dynamics of the VB and CB having the same spin, it is convenient to introduce the notation  $s = \uparrow$  ( $s = \downarrow$ ) for  $s = 1$  ( $s = -1$ ). Regarding the correspondence between the notation used in Section 5.2 and here, note that the order of the bands with  $\uparrow$  and  $\downarrow$  polarisation in the CB is different for  $\text{MoX}_2$  and  $\text{WX}_2$ . Therefore in the VB the upper index (1) ((2)) is equivalent to  $\downarrow$  ( $\uparrow$ ), but in the CB the relation depends on which material is considered. We note that the parameter  $\gamma$  can, in principle, also be obtained directly as a momentum matrix element between the Kohn–Sham wave functions of the VB and CB. For these calculations we used the CASTEP code [155], where the necessary plane-wave coefficients of the wave functions at the band edges are readily accessible. These values are denoted by  $|\gamma_{\text{KS}}|$  in Tables 6 and 7. On the one hand, the good agreement between  $|\gamma|$  and  $|\gamma_{\text{KS}}|$  indicates the consistency of our fitting procedure. This is not trivial, because the fitting involves a non-linear function of the  $\mathbf{k} \cdot \mathbf{p}$  parameters. On the other hand, one has to bear in mind that  $|\gamma|$  is obtained such that it would give the best fit to the DFT band structure over a certain range in the BZ. Therefore it may differ from the value of  $|\gamma_{\text{KS}}|$  that is calculated at a single point of the BZ. The valley index  $\tau$  is suppressed in Tables 6 and 7 because, as mentioned above, from the fitting procedure we obtain real numbers for the off-diagonal terms.

As explained in Appendix B, our fitting procedure involves the quasiparticle band gap  $E_{\text{bg,K}}$ . For this reason two sets of  $\mathbf{k} \cdot \mathbf{p}$  parameters are reported in Tables 6 and 7: one in which we used  $E_{\text{bg,K}}$  values obtained from our DFT calculations and one in which we used  $E_{\text{bg,K}}$  values found in *GW* calculations; see Table 5. In the latter case we make the

**Table 6.**  $\mathbf{k} \cdot \mathbf{p}$  parameters at the  $K$  point. In columns labelled by “DFT” the parameters obtained with the help of DFT band gap are shown, for the columns labelled by “GW” the band gap is taken from  $GW$  calculations.

	MoS <sub>2</sub>		MoSe <sub>2</sub>		WS <sub>2</sub>		WSe <sub>2</sub>	
	DFT	GW	DFT	GW	DFT	GW	DFT	GW
$E_{\text{bg},K}$ [eV]	1.67	2.80	1.40	2.26	1.60	2.88	1.30	2.42
$ \gamma_{\text{KS}} $ [eV·Å] (HSE,LDA)	3.00	–	2.52	–	3.85	–	3.31	–
$ \gamma $ [eV·Å] (HSE,LDA)	2.76	2.22	2.53	2.20	3.34	2.59	3.17	2.60
$\alpha_{\uparrow}$ [eV·Å <sup>2</sup> ] (HSE,LDA)	–5.97	–6.21	–5.34	–5.76	–6.14	–6.56	–5.25	–5.97
$\alpha_{\downarrow}$ [eV·Å <sup>2</sup> ] (HSE,LDA)	–6.43	–6.65	–5.71	–6.20	–7.95	–7.96	–6.93	–7.58
$\beta_{\uparrow}$ [eV·Å <sup>2</sup> ] (HSE,LDA)	0.28	0.52	–0.95	–0.54	1.62	2.03	0.33	1.08
$\beta_{\downarrow}$ [eV·Å <sup>2</sup> ] (HSE,LDA)	0.54	0.76	–0.52	–0.03	4.00	4.00	2.35	3.0
$\kappa_{\uparrow}$ [eV·Å <sup>2</sup> ] (HSE,LDA)	–1.48	–1.84	–1.31	–1.49	–1.24	–1.60	–1.11	–1.36
$\kappa_{\downarrow}$ [eV·Å <sup>2</sup> ] (HSE,LDA)	–1.45	–1.80	–1.23	–1.40	–1.09	–1.41	–0.93	–1.14
$\eta_{\uparrow}$ [eV·Å <sup>3</sup> ] (HSE,LDA)	13.7	17.74	15.11	18.28	21.85	29.49	18.04	23.78
$\eta_{\downarrow}$ [eV·Å <sup>3</sup> ] (HSE,LDA)	21.1	26.95	17.10	20.93	31.73	40.94	26.17	34.49

**Table 7.**  $\mathbf{k} \cdot \mathbf{p}$  parameters at the  $K$  point. In columns labelled by “DFT” the parameters obtained with the help of DFT band gap are shown, for the columns labelled by “GW” the band gap is taken from  $GW$  calculations.

	MoTe <sub>2</sub>		WTe <sub>2</sub>	
	DFT	GW	DFT	GW
$E_{\text{bg},K}$ [eV]	0.997	1.82	0.792	1.77
$ \gamma_{\text{KS}} $ [eV·Å] (HSE,LDA)	2.12	–	2.84	–
$ \gamma $ [eV·Å] (HSE,LDA)	2.33	2.16	3.04	2.79
$\alpha_{\uparrow}$ [eV·Å <sup>2</sup> ] (HSE,LDA)	–4.78	–5.31	–3.94	–5.02
$\alpha_{\downarrow}$ [eV·Å <sup>2</sup> ] (HSE,LDA)	–4.85	–5.78	–5.20	–7.31
$\beta_{\uparrow}$ [eV·Å <sup>2</sup> ] (HSE,LDA)	–2.19	–1.66	–0.9	0.17
$\beta_{\downarrow}$ [eV·Å <sup>2</sup> ] (HSE,LDA)	–1.78	–0.84	0.60	2.72
$\kappa_{\uparrow}$ [eV·Å <sup>2</sup> ] (HSE,LDA)	–1.19	–1.28	–1.01	–1.10
$\kappa_{\downarrow}$ [eV·Å <sup>2</sup> ] (HSE,LDA)	–1.01	–1.09	–0.96	–1.04
$\eta_{\uparrow}$ [eV·Å <sup>3</sup> ] (HSE,LDA)	13.26	15.18	14.72	17.61
$\eta_{\downarrow}$ [eV·Å <sup>3</sup> ] (HSE,LDA)	13.54	16.37	19.41	27.12

assumption that the bands above the Fermi energy are rigidly shifted upwards in energy such that the effective masses and the TW in the VB and CB remain the same. We believe that this is a reasonable assumption because the available experimental evidence

(see Tables 4 and 10) suggests that, at least in the VB, the effective masses are captured quite well by the DFT calculations.

## 6. Effective models at the $Q$ (a.k.a. $\Lambda$ ) point

### 6.1. $Q_i$ points

In addition to the  $K$  and  $-K$  points, there are six other minima in the CB which may be important for, e.g., relaxation processes. We denote the BZ points where these minima are located by  $Q_i$ , ( $i = 1 \dots 6$ ); they are also known as  $\Lambda$  points [see Figures 2 and 5(b)]. We note that phonon scattering between the  $K$  and  $-K$  points and  $Q_i$  points is symmetry-allowed [96] and that, depending on the energy difference  $E_{KQ}$  (see Figure 2), the electron mobility may be significantly affected by these scattering processes [39, 40, 42]. However, as we will show, understanding the SOC at the  $Q_i$  points is also important when considering the possible scattering processes, a fact which seems to have been overlooked in some recent publications. We start in Section 6.2 with a basic characterisation of the band structure in terms of the effective masses and point out an important effect of SOC on the spin polarisation of the bands. A detailed  $\mathbf{k} \cdot \mathbf{p}$  theory is given in Section 6.3.

### 6.2. Basic characterisation and material parameters

Let us consider the  $Q_1$  minimum, which can be found along the  $\Gamma$ - $K$  direction [see Figure 2(c)]. We choose  $k_x$  to be parallel to the  $\Gamma$ - $K$  direction, while  $k_y$  is perpendicular to it. Neglecting SOC for a moment, our DFT calculations show that, close to the  $Q_1$  point, the energy contours are to a good approximation ellipses whose axes are parallel to  $k_x$  and  $k_y$  [see Figure 5(a)]. Therefore, to a first approximation the dispersion around  $Q_1$  is quadratic with different effective masses  $m_{Q,x}^0$  and  $m_{Q,y}^0$  along  $k_x$  and  $k_y$ :

$$E_Q(\mathbf{q}) = \frac{\hbar^2 q_x^2}{2m_{Q,x}^0} + \frac{\hbar^2 q_y^2}{2m_{Q,y}^0}, \quad (6)$$

where the wavenumbers  $q_x$  and  $q_y$  are measured from the energy minimum of the dispersion (see Section 6.3 for details). As one can see in Table 8, the ratio of the effective masses is  $m_{Q,y}^0/m_{Q,x}^0 \approx 2$  for  $\text{MoX}_2$  and  $\text{WTe}_2$  and  $m_{Q,y}^0/m_{Q,x}^0 \approx 1.3$ – $1.8$  for  $\text{WS}_2$ ,  $\text{WSe}_2$ . The SOC has two major effects [see Figure 5(b)]:

- i) it splits the spin-degenerate levels by an energy  $2\Delta_Q$ , and
- ii) the effective masses in the spin-split bands are different.

Similarly to Section 5.2, we introduce the notation  $Q_i^{(1)}$  ( $Q_i^{(2)}$ ) for the higher-in-energy (lower-in-energy) spin-split CB at the  $Q_i$  point [see Figure 5(b)]. The basic characterisation of these bands therefore requires two effective masses for each of the two spin-split bands and the spin-splitting energy  $2\Delta_Q$ . In addition, it is also important to know the energy difference  $E_{KQ}$  between the band extrema of the  $Q_i^{(2)}$  and  $K_{\text{cb}}^{(2)}$  bands. These parameters, obtained by fitting to our DFT band structures, are shown in Table

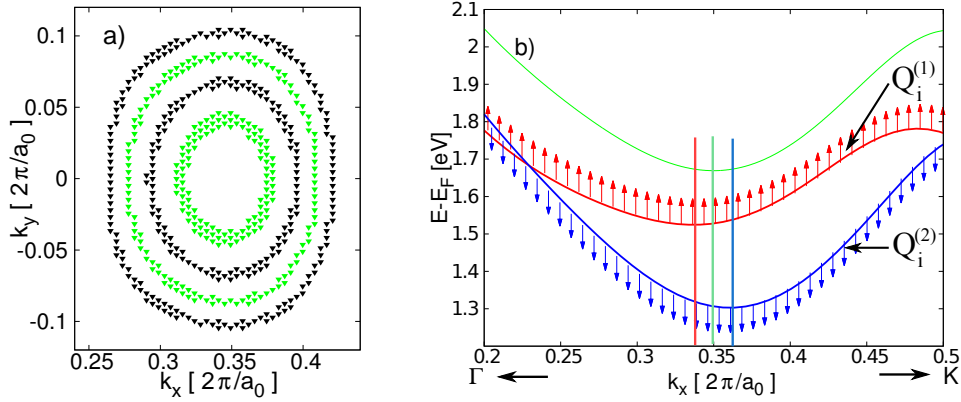


**Figure 5.** a) Energy contours at the  $Q$  point obtained from (HSE,LDA) DFT calculations for  $\text{MoS}_2$ . SOC is not taken into account. The energy difference between the energy contours is 0.04 eV. b) Band structure of  $\text{WSe}_2$  along the  $\Gamma$ - $K$  direction around the  $Q$  point with SOC (red and blue lines) and without SOC (green line). The bands without SOC are shifted in energy for clarity. Vertical bars indicate the  $k_x$  values at which the corresponding curve has a minimum. The results were obtained from (PBE,PBE) DFT calculations.

**Table 8.** Material parameters at the  $Q$  point.  $n_Q$  is the electron density above which the carriers start to populate the  $Q$  valleys, assuming (HSE,LDA) values for  $E_{KQ}$ .

	$\text{MoS}_2$	$\text{MoSe}_2$	$\text{WS}_2$	$\text{WSe}_2$	$\text{MoTe}_2$	$\text{WTe}_2$
$m_{Q,x}^{(1)}/m_e$ (HSE,LDA)	0.64	0.54	0.69	0.73	0.42	0.44
$m_{Q,x}^{(1)}/m_e$ (PBE,PBE)	0.66	0.58	0.86	0.71	0.36	0.44
$m_{Q,y}^{(1)}/m_e$ (V, HSE,LDA)	1.21	1.11	0.94	0.91	1.16	0.922
$m_{Q,y}^{(1)}/m_e$ (PBE,PBE)	1.31	1.18	0.95	0.93	1.18	0.94
$m_{Q,x}^{(2)}/m_e$ (HSE,LDA)	0.56	0.48	0.52	0.42	0.43	0.3
$m_{Q,x}^{(2)}/m_e$ (PBE,PBE)	0.61	0.51	0.54	0.45	0.44	0.29
$m_{Q,y}^{(2)}/m_e$ (HSE,LDA)	1.13	1.08	0.74	0.74	0.99	0.81
$m_{Q,y}^{(2)}/m_e$ (PBE,PBE)	1.21	1.15	0.74	0.75	1.22	0.8
$2\Delta_Q$ [meV] (HSE,LDA)	70	21	264	218	22	192
$2\Delta_Q$ [meV] (PBE,PBE)	75	26	262	221	13	201
$E_{KQ}$ [meV] (HSE,LDA)	207	137	81	35	158	158
$E_{KQ}$ [meV] (PBE,PBE)	246	163	58	32	173	140
$E_{KQ}$ [meV] (Exp)	$\gtrsim 60^a$	$150 \pm 30^b$		$\approx 0^b$		
$n_Q$ [ $10^{12} \text{ cm}^{-2}$ ] (HSE,LDA)	76.42	54.97	17.17	5.7	66.62	37.27

<sup>a</sup> from ARPES; see [156].

<sup>b</sup>[152], from scanning-tunnelling microscopy.

8. The fitting range we used was  $\approx \pm 7.5\%$  of the  $\Gamma$ - $K$  distance around the  $Q$  point in the  $k_x$  direction and roughly half of that in the  $k_y$  direction. Looking at Table 8 one can see that the effective masses obtained from the two DFT calculations are again in good agreement, while small differences can be seen in the results for  $2\Delta_Q$ . However, there

are noticeable differences in the energy separation  $E_{KQ}$  between the bottom of the CB at the  $Q$  and the  $K$  points, which we ascribe to the different lattice constants used in the two types of DFT calculations. There are no experimental results for  $E_{KQ}$  to date, except for  $\text{MoS}_2$ , where the data indicate that  $E_{KQ} \gtrsim 60$  meV [132]. Note, however, that the ARPES measurements in Reference [132] were performed on potassium-intercalated samples, and the effects of the intercalation on the band structure of TMDCs have not yet been studied in detail. We also note that computationally  $E_{KQ}$ , in contrast to the band gap  $E_{\text{bg}}$ , appears to be less sensitive to  $GW$  corrections [157] if the latter calculations are well converged. As already pointed out in Section 5.2, due to the lack of experimental evidence, it is currently difficult to tell how accurate these predictions for the effective masses and spin-splittings are.

We have also calculated the carrier density  $n_Q$  at which the Fermi energy, measured from the bottom of the  $K$ -point valley in the CB, reaches the bottom of the  $Q$ -point valley; see Table 8. We assumed a simple parabolic dispersion for the CB in the vicinity of  $K$ , where the effective masses of  $K_{\text{cb}}^{(1)}$  and  $K_{\text{cb}}^{(2)}$  are given in Table 3. Our results suggest that for  $\text{MoX}_2$  it would not be easy to achieve the doping levels needed to populate the  $Q_i^{(1)}$  valleys, but for  $\text{WS}_2$  and  $\text{WSe}_2$  the required doping levels appear to be attainable.

As noted in Reference [37], the valley–spin coupling is present not only in the  $K$  and  $-K$  valleys, but also in the  $Q_i$  valleys, and this may have experimental consequences. The calculated spin polarisation of the CB between the  $K$  and the  $Q_1$  point is shown in Figure 6 for  $\text{MoSe}_2$  and  $\text{WSe}_2$ . One finds that despite the band crossing(s) between the  $K$  and  $Q_1$  points, for  $\text{MoS}_2$  and  $\text{MoSe}_2$  the spin-polarisation of the  $Q_1^{(2)}$  band is *the same* as the spin polarisation of the  $K_{\text{cb}}^{(2)}$  band [see Figure 6(a)]. For  $\text{WX}_2$  and  $\text{MoTe}_2$ , however, due to the band crossings, the spin-polarisation of  $K_{\text{cb}}^{(2)}$  is *opposite* to the spin polarisation of  $Q_1^{(2)}$  [Figure 6(b)]. The spin polarisation of the  $Q_i^{(1)}$  and  $Q_i^{(2)}$  bands in other  $Q_i$  valleys can be deduced by taking into account time-reversal symmetry and whether they are along the  $\Gamma$ – $K$  or  $\Gamma$ – $(-K)$  line. The spin-polarisation of bands at the  $Q_i$  points determines which scattering processes are allowed or suppressed between the  $K$  ( $-K$ ) and  $Q_i$  valleys. This is illustrated in Figures 6(c) and 6(d). For example, in the case of  $\text{MoS}_2$  and  $\text{MoSe}_2$  [Figure 6(c)] scattering from  $K_{\text{cb}}^{(2)}$  to  $Q_1^{(2)}$ ,  $Q_3^{(2)}$ , and  $Q_5^{(2)}$  is allowed, while scattering to  $Q_2^{(1)}$ ,  $Q_4^{(1)}$ , and  $Q_6^{(1)}$  is, strictly speaking, also allowed but should be suppressed with respect the former processes due to the relatively large spin-splitting  $2\Delta_Q$ .

### 6.3. $\mathbf{k} \cdot \mathbf{p}$ Hamiltonian

Due to the low symmetry of the  $Q_i$  points in the BZ and because there are many nearby bands in energy, there is a large number of band-overlap parameters that would need to be taken into account in a detailed multi-band  $\mathbf{k} \cdot \mathbf{p}$  model. Therefore it is more difficult to develop such a theory and it would offer less insight. Nevertheless, a low-energy effective  $\mathbf{k} \cdot \mathbf{p}$  Hamiltonian can be derived with the help of the theory of invariants [57]



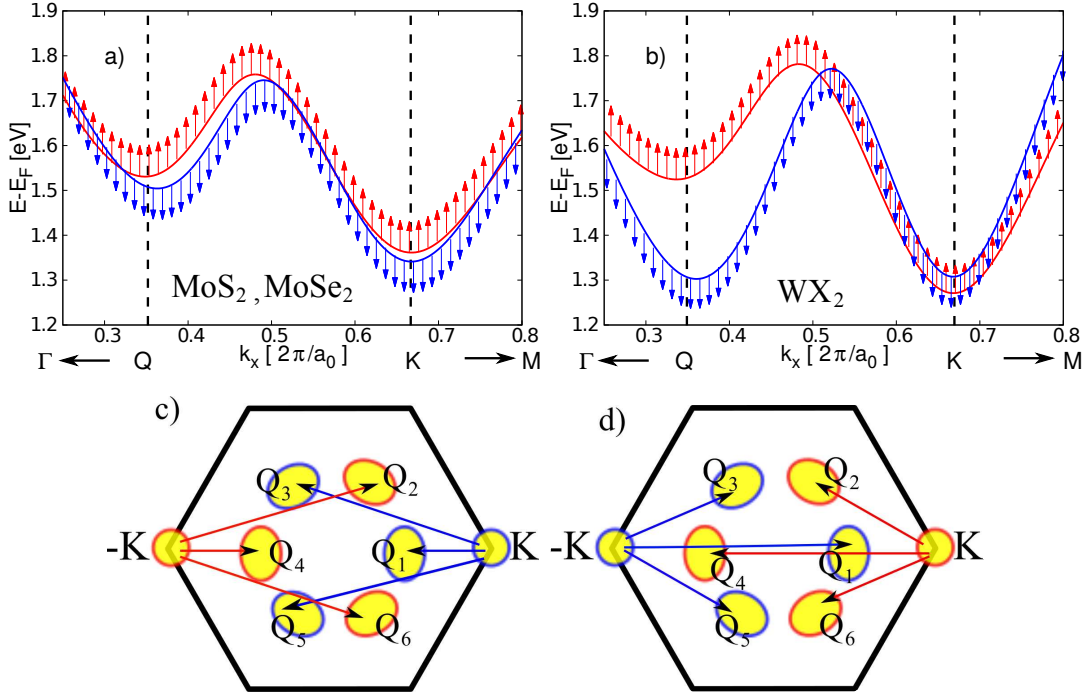


**Figure 6.** a) and b): Dispersion of the CB between the  $K$  and  $Q_1$  points obtained from DFT calculations. Arrows show the direction of the spin expectation value (red: spin-up, blue: spin-down). a) Results for  $\text{MoS}_2$  and  $\text{MoSe}_2$ ; b) results for  $\text{WX}_2$ .  $\text{MoTe}_2$ , strictly speaking, is different from both a) and b). The actual calculations were performed for  $\text{MoSe}_2$  and  $\text{WSe}_2$  using the (PBE,PBE) approach. c) and d): schematic illustration of the lowest energy allowed scattering processes between the spin-split bands at the  $K$  ( $-K$ ) and  $Q_i$  points. The situation in  $\text{MoTe}_2$  corresponds to d).

(for a recent discussion see, e.g., References [158] and [159]). The pertinent symmetry group is  $C_{1h}$ ; for convenience, its character table is shown in Table 9 [58].

**Table 9.** Character table and invariants for the group  $C_{1h}$ .

$C_{1h}$	$E$	$\sigma_h$
$A'$ $k_x^2, k_y^2, k_x k_y$	$s_z, k_x, k_y$	1
$A''$	$z, s_x, s_y$	-1

As in the case of the  $K$  and  $-K$  valleys, the  $Q_i$ -point minima are pairwise connected by time-reversal symmetry and to describe this one can introduce the matrix  $\tau_z$ , whose eigenvalues,  $\tau = \pm 1$  label individual members of the pairs of valleys. As an example, let us consider the  $Q_1$  ( $\tau = 1$ ) and  $Q_4$  ( $\tau = -1$ ) minima, which can be found along the  $\Gamma-K$  and  $\Gamma(-K)$  directions, respectively [see Figure 2(c)]. This direction is parallel to the  $k_x$  component of  $\mathbf{k}$ . Using Table 9, the most general Hamiltonian, up to second-order

in  $\mathbf{k}$  and taking SOC into account, reads:

$$H_Q^{\tau,s} = \frac{\hbar^2 k_x^2}{2m_{Q,x}^{\tau,s}} + \frac{\hbar^2 k_y^2}{2m_{Q,y}^{\tau,s}} + \frac{\hbar^2 k_x k_y}{2m_{Q,xy}^{\tau,s}} + \Delta_Q s_z \tau_z + a_1 k_x s_z + a_2 k_y s_z + b_1 k_x \tau_z + b_2 k_y \tau_z + E_Q, \quad (7)$$

$1/m_{(Q,x,y,xy)}^{\tau,s}$  are effective masses,  $s = \pm 1$  are the eigenvalues of the spin Pauli matrix  $s_z$ . Furthermore,  $E_Q$  is the band-edge energy if SOC is neglected,  $\Delta_Q$  is the spin-splitting at  $Q$ , and  $a_{1,2}$  and  $b_{1,2}$  are material parameters to be discussed later. Since we are going to develop a theory in which the dispersion is parabolic, in contrast to Section 5, we will not keep track of the free-electron contribution explicitly.

To simplify the discussion, let us first neglect the spin degree of freedom. Then  $\Delta_Q = a_{1,2} = 0$  and  $m_{(Q,x,y,xy)}^{\tau,s} = m_{(Q,x,y,xy)}^0$ . Since close to  $Q_1$  ( $Q_4$ ) the energy contours are, to a good approximation, ellipses whose axes are in the  $k_x$  and  $k_y$  directions [see Figure 5(a)], one finds that  $1/m_{(Q,x,y)}^0 = 0$ . The effect of the terms  $\sim b_1, b_2$  in Equation (7) is to shift the minimum of the dispersion. Therefore introducing the wavenumbers  $q_x$  and  $q_y$ , which are measured from  $\mathbf{k} = (\tau k_Q, 0)$ , i.e., from the  $Q_1$  ( $Q_4$ ) point, one can set  $b_1 = b_2 = 0$  and write

$$H_Q^0 = \frac{\hbar^2 q_x^2}{2m_{Q,x}^0} + \frac{\hbar^2 q_y^2}{2m_{Q,y}^0} + \tilde{E}_{KQ}, \quad (8)$$

where  $\tilde{E}_{KQ}$  measures the energy difference with respect to the  $K$  point in the absence of SOC. The effective masses  $m_{Q,x}^0$  and  $m_{Q,y}^0$  are in general different.

Taking SOC into account,  $H_Q^{\tau,s}$  [Equation (7)] can be re-written in the following form:

$$H_Q^{\tau,s} = \frac{\hbar^2 (q_x + s_z \cdot q_{Q,x})^2}{2m_{Q,x}^{\tau,s}} + \frac{\hbar^2 (q_y + s_z \cdot q_{Q,y})^2}{2m_{Q,y}^{\tau,s}} + \Delta_Q s_z \tau_z + E_{KQ}, \quad (9)$$

where  $E_{KQ}$  is defined in Figure 2. One can see that SOC has the following effects:

- i) it splits the bands and opens a gap  $\Delta_Q$  between the spin-up and spin-down bands;
- ii) it shifts the minima of the spin-split bands off from the  $\mathbf{k} = (\tau k_Q, 0)$  point by  $q_{Q,x}$  and  $q_{Q,y}$ ;
- iii) it makes the effective masses of the spin-polarised bands different, so they are given by  $1/m_{(Q,x,y)}^{\tau,s} = 1/m_{(Q,x,y)}^0 - \tau s / \delta m_{(Q,x,y)}$ .

An illustration of i) and ii) is shown in Figure 5(b) taking WSe<sub>2</sub> as an example, where these effects are most clearly seen. The material parameters  $m_{Q,x,y}^{\tau,s}$ ,  $q_{Q,x}$ ,  $q_{Q,y}$ ,  $\Delta_Q$ , and  $E_{KQ}$  can be obtained from, e.g., DFT calculations; see Section 6.2. We find that  $q_{Q,y}$  is zero within the precision of our calculations and  $q_{Q,x}$  is always very small.

## 7. Effective models at the $\Gamma$ point

### 7.1. $\Gamma$ point

Next we consider the band structure at the  $\Gamma$  point. There are three main motivations to include the  $\Gamma$  point in our work: i) there is a local maximum in the VB at the  $\Gamma$

point, which could be observed in recent ARPES measurement [106, 107] and therefore it is of interest to compare the experimental and calculated effective masses; ii) there are several experimental reports [137, 142, 143, 196] on optical transitions over a broad energy range showing peak(s) in the absorption of monolayer TMDCs at energies larger than the one corresponding to the fundamental gap at the  $K$  point. Theoretically, it was argued that in MoS<sub>2</sub> excitons can also be formed in the vicinity of the  $\Gamma$  point [47] and that these “C-excitons” are qualitatively different from the ones at the  $K$  point because they arise from an effectively one-dimensional energy minimum in the “optical band structure” (for the exact definition see below); and iii) finally, understanding of the VB and CB behaviour at the  $\Gamma$  point is important in the interpretation of scanning tunnelling microscopy (STM) experiments [146, 151, 152, 153, 160, 161].

## 7.2. Basic characterisation and material parameters

We start the discussion with the VB maximum at the  $\Gamma$  point (VBMG). The spin-splitting at  $\Gamma$  point is zero, and in the VB it remains negligible over a considerable region of  $\mathbf{k}$  space [see Figure 2(a)]. Moreover, to a good approximation the dispersion around the VBMG is isotropic (see Figure 2(b) and Section 7.3) and parabolic. Therefore it can be described by

$$E_{\Gamma}(\mathbf{k}) = E_{K\Gamma} + \frac{\hbar^2 \mathbf{k}^2}{2m_{\Gamma}^{\text{vb}}}, \quad (10)$$

which is characterised by a single effective mass  $m_{\Gamma}^{\text{vb}}$  and the energy  $E_{K\Gamma}$ , which is the energy difference between the maximum of the  $K_{\text{vb}}^{(1)}$  band at the  $K$  point and the VBMG. The values of  $m_{\Gamma}^{\text{vb}}$  obtained from fitting the results of our DFT calculations are given in Table 10 and experimental results, where available, are also shown. The effective masses  $m_{\Gamma}^{\text{vb}}$  were obtained by fitting the band structure along the  $\Gamma$ – $K$  direction in a range of  $\approx 21\%$  of the  $\Gamma$ – $K$  distance. The calculated  $m_{\Gamma}^{\text{vb}}$  values are in reasonable agreement with the available experimental results. There are, however, noticeable differences between the theoretical and experimental  $E_{K\Gamma}$  values, which we attribute to substrate effects. Note that the weight of the chalcogen  $p$  orbitals is substantial at the  $\Gamma$  point (see Figure 3 or Reference [35]) so that one can expect a stronger interaction between the substrate and the electronic states. Interestingly, the  $m_{\Gamma}^{\text{vb}}$  parameter does not seem to be affected as strongly as  $E_{K\Gamma}$  by the substrate. Comparing Tables 4 and 10, one would expect the VBMG to be the most important for the transport properties of MoS<sub>2</sub> because it is probably quite close in energy to the maximum of the  $K_{\text{vb}}^{(1)}$  band (which we denote by VBMK1; we also introduce the label VBMK2 for the maximum of the  $K_{\text{vb}}^{(2)}$  band), thus facilitating scattering processes in the VB that do not require spin-flips. Furthermore, according to our DFT calculations VBMG lies in between VBMK1 and VBMK2 for MoS<sub>2</sub> and WS<sub>2</sub>, while it lies below VBMK2 for MoSe<sub>2</sub> and WSe<sub>2</sub>.

Optical transitions at higher energies than the ones at the fundamental band gap have attracted considerable theoretical interest [47, 162, 163, 164] recently. To obtain an insight into the possible transitions, we plot the optical band structure for monolayer

**Table 10.** Effective masses  $m_{\Gamma}^{\text{vb}}$  at the  $\Gamma$  point in the VB from DFT calculations.  $m_e$  is the free electron mass. The energy difference  $E_{\text{K}\Gamma}$  between the VBMG and VBMK1 is also given.  $n_{\Gamma}$  is the hole density where the states at the  $\Gamma$  point start to fill with holes assuming the (HSE,LDA) values for  $E_{\text{K}\Gamma}$ . Experimental values are shown in rows denoted by “Exp”.

	MoS <sub>2</sub>	MoSe <sub>2</sub>	WS <sub>2</sub>	WSe <sub>2</sub>	MoTe <sub>2</sub>	WTe <sub>2</sub>
$m_{\Gamma}^{\text{vb}}/m_e$ (HSE,LDA)	-2.60	-3.94	-2.18	-2.87	-29	-5.19
$m_{\Gamma}^{\text{vb}}/m_e$ (PBE,PBE)	-2.45	-3.49	-2.15	-2.70	-10.76	-4.18
$m_{\Gamma}^{\text{vb}}/m_e$ (Exp)	$-2.4 \pm 0.3^a$	$-3.9 \pm 0.3^b$				
$E_{\text{K}\Gamma}$ [meV] (HSE,LDA)	-70	-342	-252	-496	-540	-630
$E_{\text{K}\Gamma}$ [meV] (PBE,PBE)	-46	-329	-269	-506	-526	-646
$E_{\text{K}\Gamma}$ [meV] (Exp)	$\approx -140^a$	$-380^c$		$-880^e$		
		$-370 \pm 40^d$		$-590 \pm 40^d$		
$n_{\Gamma}$ [10 <sup>12</sup> cm <sup>-2</sup> ](HSE,LDA)	15.8	130	36.86	81.4	259	124.92

<sup>a</sup>[106], ARPES measurements, exfoliated samples on SiO<sub>2</sub> substrate.

<sup>b</sup>private communication by Yi Zhang, ARPES measurements, see [107].

<sup>c</sup>[107], ARPES measurements, samples grown by MBE on bilayer graphene on top of SiC (0001).

<sup>d</sup>[152], STM measurements, samples grown by MBE on HOPG.

<sup>e</sup>[193], ARPES measurements, exfoliated samples on SiO<sub>2</sub> substrate.

TMDCs in Figures 7-9 over the whole BZ. Here, following References [142] and [165], the optical band structure is defined as the difference between the dispersions of the CB and VB:  $E_{\text{cb}}(\mathbf{k}) - E_{\text{vb}}(\mathbf{k})$ . For simplicity, SOC is neglected in these calculation. A clear “gear-shaped” minimum [142] is noted both for MoS<sub>2</sub> and WS<sub>2</sub> around the  $\Gamma$  point [Figures 7(a) and 8 (a)] and for each material one can also observe saddle point(s). Both minima and saddle points lead to Van Hove singularities in the optical density of states (see below) and can have an important effect on the interband optical transitions. For a more quantitative understanding of the interband transitions therefore one also needs to consider the optical density of states (optical DOS), which is defined as the density of states of the optical band structure (the terminology “joint density of states” is also used; see, e.g., [165]). For 2D systems it reads

$$\rho_{\text{cv}}(E) = \frac{2}{(2\pi)^2} \int \delta([E_{\text{cb}}(\mathbf{k}) - E_{\text{vb}}(\mathbf{k})] - E) d^2\mathbf{k}. \quad (11)$$

The calculated optical DOS for the monolayer TMDCs that we have considered are shown in Figures 7–9. A peak in the optical DOS corresponding to the minimum in the optical band structure is present at  $\approx 2.65$  eV for MoS<sub>2</sub> [Figure 7(c)] and  $\approx 2.75$  eV for WS<sub>2</sub> [Figure 8(c)]. However, other peak(s) and a wide shoulder extending into higher energies can also be seen in the optical DOS. We attribute these features to saddle points in the optical band structure, which can be observed, e.g., along the  $\Gamma$ – $K$  line for WS<sub>2</sub> and to the saddle points at the  $M$  point in the optical band structure of all four MX<sub>2</sub> materials. These observations motivate us to have a closer look at the band structure at the  $M$  point as well, which is presented in Section 8.

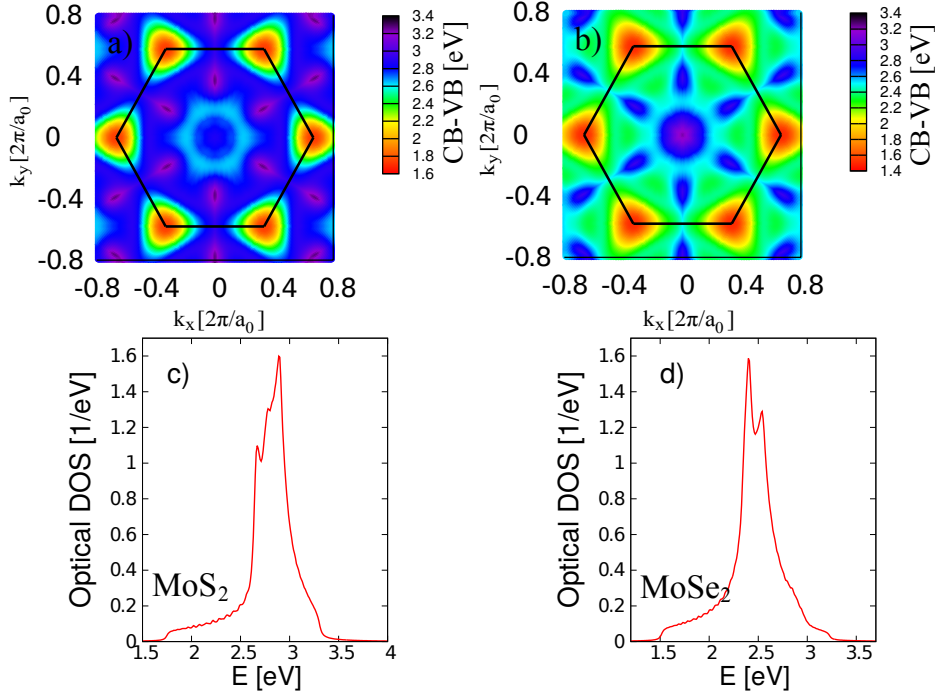


**Figure 7.** Optical band structures [a) and b)] and the corresponding optical densities of states [c) and d)] obtained from (HSE,LDA) DFT calculations in which SOC was neglected. In a) and c) data for MoS<sub>2</sub> are shown; in b) and d) data for MoSe<sub>2</sub> are shown. In a) a lighter colour “gear-shaped” region around the  $\Gamma$  point is clearly visible.

Finally, we emphasise that for a quantitative understanding of the optical band structure and the interband optical transitions the effects of SOC are also important. In general, they lead to spin-splitting of the bands (except along the  $\Gamma$ – $M$  line), or splitting of the Van Hove singularity (see Section 8.1). The energies of these splittings may be comparable to or larger than the linewidth of the optical transitions leading to, e.g., the possibility of spin-polarised optical current injection [26, 164].

### 7.3. $\mathbf{k} \cdot \mathbf{p}$ Hamiltonian

As in previous sections, we use group theory to obtain effective  $\mathbf{k} \cdot \mathbf{p}$  Hamiltonians for the VB and CB. Similarly to the  $K$  point, it is possible to set up a multi-band  $\mathbf{k} \cdot \mathbf{p}$  model. We have found, however, that the number of necessary bands, even if one neglects SOC, is quite large and, as will be shown later, terms up to fourth order in  $\mathbf{k}$  need to be taken into account in order to capture the features of the band structure related to the C-exciton terms. Therefore we present here only a simplified discussion of the problem; a more complete theory is left for a future work. As we will show, important insight can be gained from the spinless case, i.e., in the discussion that follows we will neglect SOC.

The bands of interest are the VB, the (doubly degenerate) CB [shown by green lines

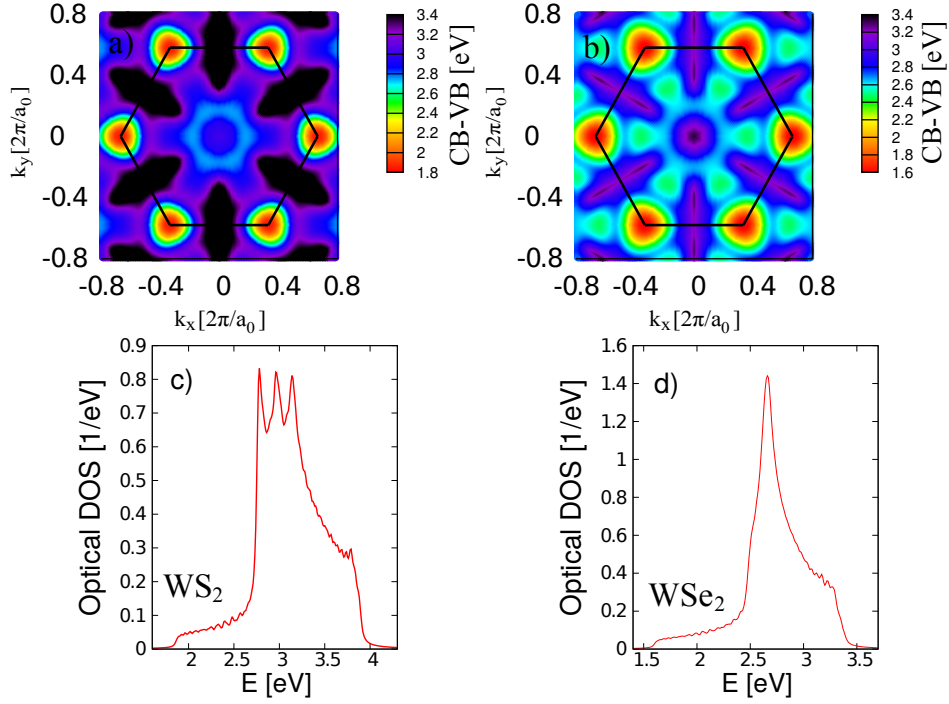


**Figure 8.** Optical band structures [a) and b)] and the corresponding optical densities of states [c) and d)] obtained from (HSE,LDA) DFT calculations in which SOC was neglected. In a) and c) data for  $\text{WS}_2$  are shown; in b) and d) data for  $\text{WSe}_2$  are shown.

in Figure 10(a)] and the first (doubly degenerate) band *above* the CB, which we denote by CB+1 [black lines in Figure 10(a)]. We will rely on group-theoretical arguments, which are very convenient at the  $\Gamma$  point, where, as mentioned above, several atomic orbitals contribute with significant weight to each band. The pertinent symmetry group is  $D_{3h}$  and the character table is shown in Table 11.

**Table 11.** Character table of the point group  $D_{3h}$ .

$D_{3h}$	$E$	$\sigma_h$	$2C_3$	$2S_3$	$3C'_2$	$3\sigma_v$
$A'_1$	1	1	1	1	1	1
$A'_2$	1	1	1	1	-1	-1
$A''_1$	1	-1	1	-1	1	1
$A''_2$	1	-1	1	-1	-1	-1
$E'$	2	2	-1	-1	0	0
$E''$	2	-2	-1	1	0	0

Symmetry analysis of the contributing atomic orbitals implies (see, e.g., Table IV in Reference [60] and the discussion at the end of Appendix A) that the VB at the  $\Gamma$  point belongs to the  $A'_1$  irreducible representation of  $D_{3h}$ . As already given in Equation (10), up to second order in  $\mathbf{q}$ , the dispersion is parabolic and isotropic [see Figure 2(b)], characterised by a single effective mass  $m_{\Gamma}^{\text{vb}}$ . Values of  $m_{\Gamma}^{\text{vb}}$  obtained from fitting the

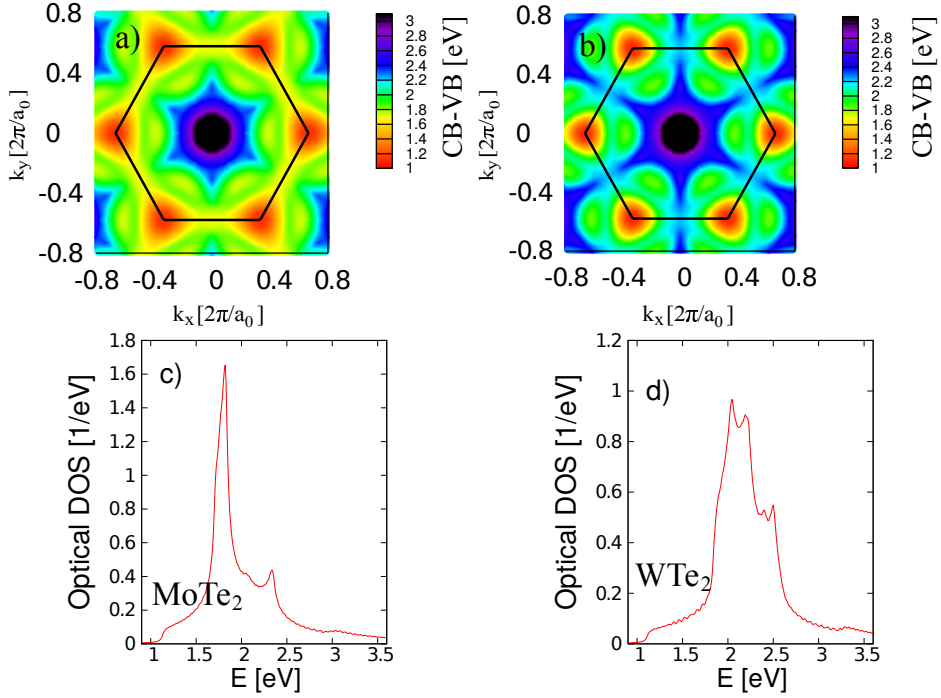


**Figure 9.** Optical band structures [a) and b)] and the corresponding optical densities of states [c) and d)] obtained from (HSE,LDA) DFT calculations in which SOC was neglected. In a) and c) data for MoTe<sub>2</sub> are shown; in b) and d) data for WTe<sub>2</sub> are shown.

DFT band structures are shown in Table 10. Along the  $\Gamma$ - $K$  direction, the spin-splitting of the VB is small up to wavevectors corresponding to about half of the  $\Gamma$ - $Q$  distance. This is due to the fact that in the vicinity of  $\Gamma$  the  $d_{z^2}$  atomic orbitals of the metal and the  $p_z$  atomic orbitals of the chalcogen atoms contribute with large weight to the VB (see Figure 3 and [34, 35]). Along  $\Gamma$ - $M$  all bands remain spin-degenerate due to symmetry; see Section 8.1. The spin-splitting of the VB is therefore suppressed around the  $\Gamma$  point.

Turning now to the CB [shown by green lines in Figure 10(a)], at the  $\Gamma$  point it is doubly degenerate and antisymmetric with respect to the horizontal mirror plane  $\sigma_h$  of the crystal lattice. In group theoretical terms, it corresponds to the  $E''$  irreducible representation (irrep) of  $D_{3h}$ . Since the VB is symmetric with respect to  $\sigma_h$ , one can show using group-theoretical arguments that the optical matrix element between the VB, which has  $A'_1$  symmetry, and the CB, which has  $E''$  symmetry, is zero at the  $\Gamma$  point.

However, as shown in Figure 10, due to band crossings one of the degenerate CB+1 bands becomes the CB at some distance from  $\Gamma$ . The doubly degenerate CB+1 band belongs to the 2D  $E'$  irreducible representation of  $D_{3h}$ . This irrep is symmetric with respect to  $\sigma_h$ , and optical transitions between bands of  $A'_1$  and  $E'$  symmetries are allowed. Therefore as a starting point for studying the optical transitions in the vicinity of the  $\Gamma$  point one has to describe the CB+1 bands.

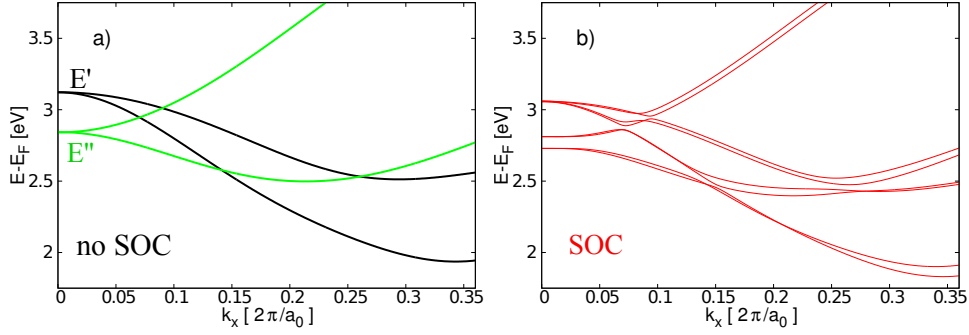


**Figure 10.** a) The dispersion of the CB and CB+1 bands along the  $\Gamma$ - $K$  direction, without taking SOC into account. Black lines show the symmetric  $E'$  bands and green lines the antisymmetric  $E''$  bands. b) The same as in a) but the SOC is taken into account. The actual DFT calculation were performed for MoS<sub>2</sub> using the (HSE,LDA) approach; for other materials the results are qualitatively similar, except that the spin-splittings are larger.

Up to second-order terms in the wavevector  $\mathbf{k}$ , the effective Hamiltonian describing the  $E'$  bands in the vicinity of  $\Gamma$  reads:

$$H_{\Gamma,\text{eff}}^{\text{cb}+1} = H_0 + H_d^{(2)} + H_{wr}^{(2)}, \quad (12a)$$

$$H_d^{(2)} = (\varepsilon_{\text{cb}+1} + \alpha \mathbf{k}^2) \cdot \mathbb{1}_2, \quad (12b)$$

$$H_{wr}^{(2)} = -\beta \mathbf{k}^2 \begin{pmatrix} (1 - \cos(3\phi_{\mathbf{k}})) & \frac{1}{2}(e^{i6\phi_{\mathbf{k}}} - 1)e^{-2i\phi_{\mathbf{k}}} \\ \frac{1}{2}(e^{-i6\phi_{\mathbf{k}}} - 1)e^{2i\phi_{\mathbf{k}}} & (1 + \cos(3\phi_{\mathbf{k}})) \end{pmatrix}, \quad (12c)$$

where  $\mathbb{1}_2$  is a  $2 \times 2$  unit matrix, and  $\phi_{\mathbf{k}}$  is the argument of  $k_x + ik_y$  (here the wavevector components  $k_x$  and  $k_y$  are measured from  $\Gamma$ ). We also keep explicit the free-electron term  $H_0 = \frac{\hbar^2 \mathbf{k}^2}{2m_e} \cdot \mathbb{1}_2$ . The term  $\alpha \mathbf{k}^2$  in  $H_d^{(2)}$  describes the coupling of the CB+1 bands to other remote bands with the same  $E'$  symmetry, while  $H_{wr}^{(2)}$  captures the coupling of the CB+1 bands to other remote bands with  $A'_1$  symmetry. In contrast to the VB, one can see that  $H_{wr}^{(2)}$  leads to a hexagonal distortion of the energy contours of the CB+1 bands already in second order of  $\mathbf{k}$ . Looking at Equation (12c) one can also note that, e.g., along the  $\Gamma$ - $K$  line the off-diagonal and one of the diagonal terms become zero. Therefore Equation (12c) alone would suggest that one of the  $E'$  bands is dispersionless. Since the dispersion of the higher-in-energy  $E'$  band is indeed very flat along  $\Gamma$ - $K$  [see Figure 10(a)], we expect that  $H_d^{(2)}$  largely cancels  $H_0$ .

SOC, as illustrated in Figure 10(b), has two main effects:

- i) At the  $\Gamma$  point it leads to a splitting of the otherwise degenerate states. Therefore, instead of four-fold degeneracies, which would follow from taking into account the spin but not the SOC there are only two-fold degeneracies. [For the  $E'$  bands in MoS<sub>2</sub> the splitting is too small to be seen on the scale of Figure 10(b)].
- ii) Close to the  $\Gamma$  point the band crossings between the  $E'$  and  $E''$  bands are turned into avoided crossings.



One can observe, however, that beyond these avoided crossings the dispersion of the spin-split CB follows that of the spinless CB quite closely. This is remarkable for the following reason: it has been argued [142] that the existence of the C-exciton is related to a minimum in the optical band structure. Looking along the  $\Gamma$ - $K$  or  $\Gamma$ - $M$  lines, the minimum in the optical band structure can be found for  $\mathbf{k}$  values where the spinful CB closely follows the lower-in-energy  $E'$  band. We expect therefore that, theoretically, the starting point for describing the C-exciton physics in an effective-mass approximation would be to extend the model shown in Equations (10) and (12a) by terms that contain higher powers of  $\mathbf{k}$ , especially for the  $E'$  bands, where these corrections become important closer to the  $\Gamma$  point than is the case in the VB. Neglecting the coupling between the two  $E'$  bands and considering only the one lower-in-energy band that becomes the CB, the terms up to fourth order in  $\mathbf{k}$  that need to be added to the dispersion are

$$H^{(3)} + H^{(4)} = C^{(3)}|\mathbf{k}|^3(1 + \cos \phi_{\mathbf{k}}) + |\mathbf{k}|^4[C_1^{(4)} + C_2^{(4)}(1 + \cos \phi_{\mathbf{k}}) + C_3^{(4)}(1 + \cos \phi_{\mathbf{k}})^2], \quad (13)$$

where the constants  $C^{(3)}$  and  $C_{1,2,3}^{(4)}$  can be obtained from fitting the band structure.

Looking at Figures 7 and 8, this approach appears to be most useful for MoS<sub>2</sub> and WS<sub>2</sub>, where a clear minimum in the optical band structure in the vicinity of  $\Gamma$  can be seen. However, the exact location of the minimum in the optical band structure would also depend on the SOC, which was not taken into account in Figures 7 and 8 and this introduces additional complexity into the problem. A detailed discussion of the optical band structure based on  $\mathbf{k} \cdot \mathbf{p}$  theory is therefore left for a future work. Numerically, using DFT calculations combined with maximally localised Wannier functions, the effects of SOC on the optical transitions have very recently been studied in Reference [164].

#### 7.4. $\Gamma$ point wave functions and STM measurements

The shape and extent of the VB and CB wave functions at the  $\Gamma$  point can also play an important role in the interpretation of STM measurements. Since there is a growing experimental interest [146, 151, 152, 153, 160, 161] in STM studies of monolayer TMDCs, we give a brief account of calculations that can be used to interpret STM measurements.

We first focus on the STM maps that one can obtain using a tip with a curvature radius larger than atomic distances at scanning distances comparable to or larger than the lattice constant. In this case the current is dominated by electrons tunnelling from the metal with the largest  $k_z$  momentum component at the energy given by the scanning voltage. Therefore the in-plane momentum components of the tunnelling electron can be neglected:  $k_{x,y} \rightarrow 0$ . On one hand, this implies that the real space 2D maps of the tunnelling current should reflect the vertical extent of the  $\Gamma$ -point wave functions in the CB and VB. On the other hand, electron tunnelling into the band edges, which are at the  $K$  and  $-K$  points, can take place as a two-step process: first, the electron tunnels into a virtual state close to the  $\Gamma$  point in the corresponding band, then it emits a BZ-corner phonon to scatter into the final state near the band edge. The expected  $I$ - $V$  characteristic therefore should have a tunnelling gap in the current of magnitude

of the phonon energy, counted from the Fermi level in a doped 2D semiconductor or the band edge in an undoped one.

STM images of bulk  $\text{MX}_2$  can be simulated from first-principles. Since in STM measurements one detects the tail of either the VB or CB wave function, depending on whether electrons or holes are injected into the material, one has to determine the decay rate of the wave function of the relevant states in different parts of the unit cell. This can be achieved by numerical differentiation of the logarithm of the square modulus of the band-decomposed wave function along the  $z$  direction (i.e., perpendicular to the sheet). For this purpose we use a trilayer geometry to model the surface of the bulk material, since we do not expect the inter-layer interaction to affect the tail of the wave functions severely. In these calculations we used the optB88 van der Waals density functional [105]. This functional should provide a significantly better description of the interlayer interaction than the LDA or PBE functionals. Figure 11 illustrates the decay

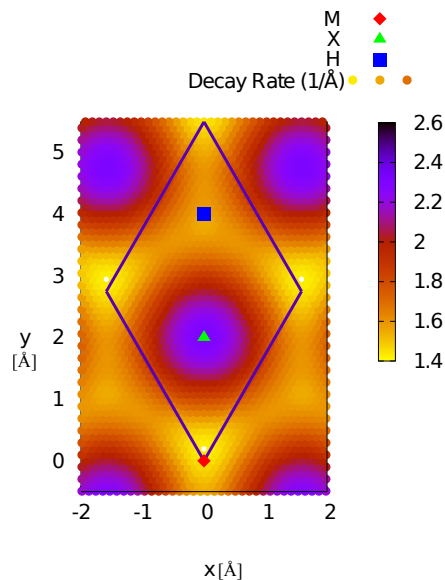


**Figure 11.** Decay rate in the unit cell of  $\text{MoS}_2$ .

rate of the VB of  $\text{MoS}_2$ . Three points are highlighted: the position of the metal atom (M), the chalcogen atom (X), and the centre of the hexagon formed by three M and three X atoms on the surface (H). Large tunnelling currents occur when the decay rate is low. For example, in the case of the VB, the tunnelling current is dominated by the contribution of the sublattice where the metal atom is located in the VB. Note that the centre of the hexagon is also quite bright; this is due to constructive interference between the  $p_x$  and  $p_y$  orbitals of the chalcogen atoms. Table 12 summarises the decay rates at the three notable positions in the unit cell for the four  $\text{MX}_2$  materials studied in this work. It can be used to explain which sublattice is expected to dominate the tunnelling current in a particular  $\text{MX}_2$  material. A recent experiment [152] has shown a  $\Gamma$ -point decay rate of  $\approx 0.9/\text{\AA}$  in monolayer  $\text{MoSe}_2$  and  $\approx 0.7/\text{\AA}$  in monolayer  $\text{WSe}_2$  on graphitic substrate. These values are in good agreement with our calculated result

**Table 12.** Decay rate of monolayer  $\text{MX}_2$  at the  $\Gamma$  point in units of  $1/\text{\AA}$ .

	MoS <sub>2</sub>	MoSe <sub>2</sub>	MoTe <sub>2</sub>	WS <sub>2</sub>	WSe <sub>2</sub>	WTe <sub>2</sub>
$M_{VB}$	1.44	0.91	1.20	1.54	1.02	1.35
$X_{VB}$	2.31	2.19	3.18	2.33	2.10	3.07
$H_{VB}$	1.53	1.20	2.03	1.60	1.23	1.98
$M_{CB}$	5.10	3.50	5.44	3.50	3.28	5.37
$X_{CB}$	3.84	4.28	6.01	4.50	4.48	5.99
$H_{CB}$	5.01	3.89	5.50	6.40	3.96	5.49

of 0.91 and 1.02  $1/\text{\AA}$ , respectively.

One can also envisage an alternative STM arrangement where the tunnelling current is determined by coupling with a single atomic site at the end of the tip brought to atomic/subatomic distances from the 2D material. In this case, momentum transfer and momentum conservation are not problems for the tunnelling electron; hence, the tunnelling spectrum may reflect the structure of the electronic wave function at the band edges in the BZ corners. However, in this case, the actual current maps would be affected by the form of the atomic orbital of the last atom in the tip and analysis of such details lies outside the scope of this review.

## 8. The $M$ point: spin-orbit splitting of the Van Hove singularity

In Section 7 we have already shown that optical transitions in monolayer TMDCs are expected to occur not only at the  $K$  and  $-K$  points, but at other points in the BZ as well. Indeed, a strong light-matter interaction was observed in Reference [20] and attributed to Van Hove singularities in the electronic density of states. Moreover, strong absorption beyond the energy range of visible light has been found in MoS<sub>2</sub> [143] and in WSe<sub>2</sub> [196]. High-energy optical transitions (in the range of 1.5–9 eV) have also been studied using ellipsometry in Reference [140]. Very recently, it was argued that electron-phonon scattering processes involving the  $M$  point may help to explain the origin of certain peaks in the Raman spectrum of monolayer MoTe<sub>2</sub> [194]. Motivated by these observations and by the fact that, according to Figures 7 and 8, the optical DOS is finite at energies that correspond to transitions at the  $M$  point of the BZ, we briefly discuss the dispersion of the VB and CB at the  $M$  point. Higher energy optical transitions in TMDCs were studied theoretically in Refs. [162, 164], and the effects of a saddle point in the dispersion have also been investigated recently in monolayer graphene [166].

### 8.1. Basic characterisation and $\mathbf{k} \cdot \mathbf{p}$ Hamiltonian

Figure 12 shows the band structure of a monolayer TMDC near the  $M$  point of the BZ. Looking at Figure 12(a) first, where the SOC is neglected, one can see that upon going from  $M$  towards  $K$  the energy difference between the VB and the CB decreases, whereas

along the  $M$ - $\Gamma$  direction it slightly increases. This leads to a saddle point in the optical band structure, as shown in Figures 7 and 8. It is important to point out that for all the

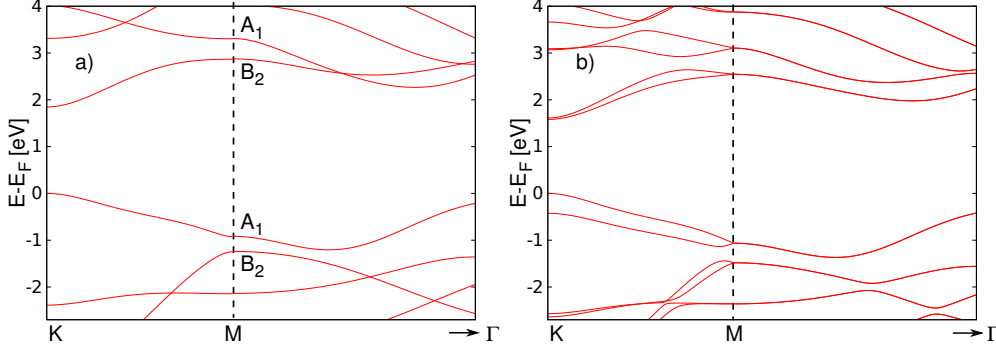


**Figure 12.** Band structure of a monolayer TMDC at the  $M$  point obtained from DFT calculations a) without taking SOC into account; and b) with SOC. In a) the labels above the bands denote the pertinent irreps of the group  $C_{2v}$ . The actual calculations were performed for  $\text{WS}_2$  using the (PBE,PBE) approach.

monolayer TMDCs considered here the energy difference between the CB and the CB+1 (VB and VB-1) bands is rather small compared to the band gap; the difference between the CB and CB+1 is around 0.5 eV and the difference between the VB and VB-1 is 0.15-0.3 eV. Therefore, regarding optical transitions, the situation at the  $M$  point is different from the  $K$  point, where the CB and the VB are well separated in energy from all other bands. It is also different from the situation encountered at the  $\Gamma$  point, where the CB was antisymmetric, while the VB and the CB+1 bands were symmetric with respect to the horizontal mirror plane. Here all four bands are symmetric and in-plane polarised electromagnetic radiation can, in principle, induce transitions between them.

The discussion of the band dispersion at the  $M$  point is simplified if one introduces the local coordinate system shown in Figure 13. Here both  $q_x$  and  $q_y$  are measured from the  $M$  point, the former being parallel to the  $K$ - $M$  direction, the latter to the  $\Gamma$ - $M$  direction. Similarly to the  $Q$  point, we content ourselves with the construction of a  $\mathbf{k} \cdot \mathbf{p}$

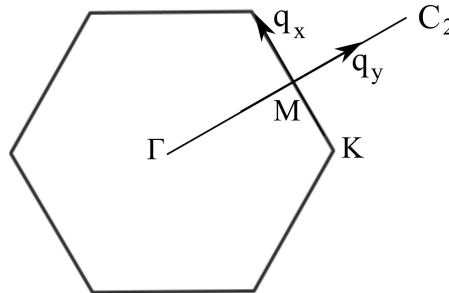


**Figure 13.** Local coordinate system at the  $M$  point of the BZ. The twofold rotation axis  $C_2$  is also shown.

Hamiltonian based on the theory of invariants. The six  $M_i$  points in the BZ are pairwise

connected by time-reversal symmetry. To describe this one can introduce the matrix  $\tau_z$ , whose eigenvalues,  $\tau = \pm 1$  label individual members of the pairs of  $M$  points. In the simplest approximation, the Hamiltonian of all four bands of interest is

$$H_M^{\tau,s} = \frac{\hbar^2 q_x^2}{2m_{M,x}^{\tau,s}} + \frac{\hbar^2 q_y^2}{2m_{M,y}} + \tau_z \Delta_M q_x s_z. \quad (14)$$

One can see that the dispersion is parabolic and characterised by different effective masses  $m_{M,x}^{\tau,s}$  and  $m_{M,y}$  along the  $M$ - $K$  and  $M$ - $\Gamma$  directions, respectively. To understand the implications of Equation (14), let us first neglect the SOC, i.e., we set  $\Delta_M = 0$  and  $m_{M,x}^{\tau,s} = m_{M,x}$ . Looking at Figure 12(a) one can notice that for the CB (denoted by  $B_2$ ) the effective masses  $m_{M,x}$  and  $m_{M,y}$  have the same sign. For the VB (denoted by  $A_1$ ), however, their sign is different. Similar conclusions hold for the CB+1 and the VB-1 bands. Therefore in the optical band structure one has a saddle point in the dispersion and consequently a Van Hove singularity.

SOC, as shown in Figure 12(b), has two main effects:

- i) It leads to a linear-in- $q_x$  splitting of the bands along  $M$ - $K$ , while the bands remain spin-degenerate along  $M$ - $\Gamma$ . This means that the saddle point in the optical DOS of any two bands will also be split along  $M$ - $K$ . In addition, the effective mass  $m_{M,x}^{\tau,s}$  becomes spin dependent.
- ii) It turns band crossings into avoided crossings.

As shown in Figure 12(b), the linear-in- $q_x$  splitting of the bands is a rather good approximation close to  $M$ . However, the situation is complicated by the fact that the CB+1 (VB-1) band is quite close in energy to the CB (VB). SOC couples the CB and CB+1 (VB and VB-1) bands and leads to avoided crossings between them. Therefore a more complete description would require a model similar to the  $K$  point, where the coupling of nearby bands is explicitly taken into account. We leave the construction of such a model to a future work.

The Hamiltonian of Equation (14) can be constructed using the theory of invariants. The symmetry group at the  $M$  point (and along  $\Gamma$ - $M$ ) is  $C_{2v}$ , which includes the following symmetry operations: a twofold rotation  $C_2$  around the  $\Gamma$ - $M$  direction, a reflection  $\sigma_v$  with respect to the  $q_y$ - $q_z$  plane, and the reflection  $\sigma_h$  with respect to the  $q_x$ - $q_y$  plane. The character table of  $C_{2v}$  is shown in Table 13, where the relevant basis functions, in the chosen coordinate system, are also given. The Hamiltonian, which

**Table 13.** Character table for the group  $C_{2v}$ . Basis functions for a given irrep are also shown.  $R_{x,y,z}$  denotes the angular momentum components.

$D_{2v}$			$E$	$C_2$	$\sigma_v$	$\sigma_h$
$A_1$	$q_x^2, q_y^2$	$q_y$	1	1	1	1
$A_2$		$R_y$	1	1	-1	-1
$B_1$		$R_x, q_z$	1	-1	1	-1
$B_2$	$q_x q_y$	$R_z, q_x$	1	-1	-1	1

can be constructed with the help of Table 13 and which is at most second order in the wavenumbers  $q_x$  and  $q_y$ , is given in Equation (14). The symmetries of the individual bands at the  $M$  point, which can be deduced by, e.g., considering which atomic orbitals contribute to a certain band, are indicated in Figure 12(a).

It is important to note that there is another possible optical transition, which may have a similar energy to the one between the VB and the CB at the  $M$  point. This

**Table 14.** Higher-energy optical transitions in monolayer TMDCs based on DFT calculations. SOC is taken into account.

	MoS <sub>2</sub>	MoSe <sub>2</sub>	WS <sub>2</sub>	WSe <sub>2</sub>	MoTe <sub>2</sub>	WTe <sub>2</sub>
$E_{M,VB \rightarrow CB}$ [eV] (HSE,LDA)	2.93	2.52	3.60	3.03	1.67	2.04
$E_{M,VB \rightarrow CB}$ [eV] (PBE,PBE)	2.83	2.48	3.61	3.04	1.67	2.07
$E_{M,VB \rightarrow CB}$ [eV] (GW)	3.87 <sup>a</sup>					
$E_{K,VB \rightarrow CB+2}$ [eV] (HSE,LDA)	3.56	3.02	3.77	3.16	2.46	2.48
$E_{K,VB \rightarrow CB+2}$ [eV] (PBE,PBE)	3.40	2.88	3.66	3.05	2.31	2.37

<sup>a</sup> [47].

transition can occur between the upper spin-split VB and the lower spin-split CB+2 (see Figure 14). Our DFT results shown in Table 14 suggest that for MoX<sub>2</sub> the transition at the  $M$  point has lower energy, while for WX<sub>2</sub> they are nearly degenerate. This prediction does not take into account excitonic effects, which are also expected to be important and may determine which transition actually has the lower energy, because the exciton binding energies at  $K$  and  $M$  may be different. We expect that, e.g., the polarisation of

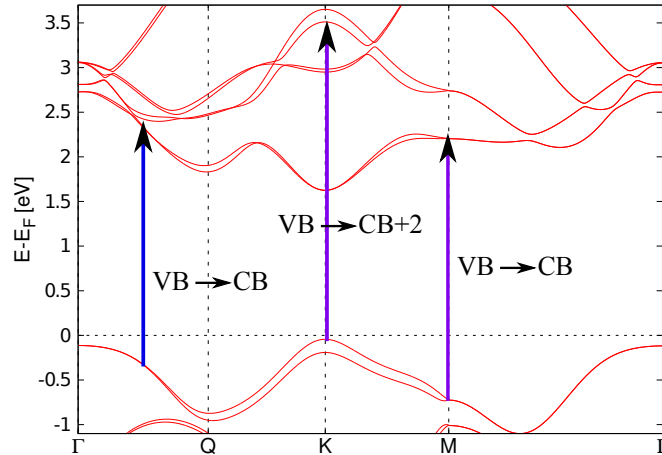


**Figure 14.** Optical transitions discussed in Sections 7.2 and 8.1.

the photoluminescence can give important information about these transitions. If the incident light is circularly polarised, then the photoluminescence related to the transition  $VB \rightarrow CB+2$ , which takes place at the  $K$  and  $-K$  points, should also be circularly polarised, as is the case for the well known fundamental  $VB \rightarrow CB$  transition. Since the

local symmetry at the  $M$  point is different, we do not expect that the photoluminescence due to the VB $\rightarrow$ CB transition at the  $M$  points is circularly polarised.

## 9. Conclusions

In this short review we have focused on the band structure of monolayer TMDCs. Our aim has been to discuss all the details of the band structure that we believe are relevant for transport and relaxation processes and optical transitions. The two main tools that we used were the (local) symmetries of the BZ (an essential ingredient of the  $\mathbf{k} \cdot \mathbf{p}$  expansion) and DFT calculations. The first of these tools allowed us to capture general features of the band structure. Material parameters, such as effective masses, spin-splittings, and band edge energy differences depend on the chemical composition of particular TMDCs and are important for quantitative predictions. For this reason we also performed extensive DFT calculations which can, in many cases, predict material parameters accurately. From a theoretical point of view, an important aspect of the approach used in this work is that it leads to explicit  $\mathbf{k} \cdot \mathbf{p}$  Hamiltonians that can be used to address a variety of problems. In particular, they are expected to be accurate when external perturbations vary on length scales much larger than the interatomic distances. Therefore we believe our results will help to develop further (semi)analytical approaches to study, e.g., exciton physics [86, 167, 168, 169, 170, 171, 172], plasmons [173, 174], diffusive transport [175], spin [176, 177], noise [178], topological properties [179, 180], valley-currents [122, 181, 182], proximity effect [183, 184], electron–electron interaction [185], and quantum dots [49, 186]. On the other hand, TB-based methods are probably more appropriate for studying the effects of, e.g., point or line defects [38, 187] on transport.

The picture that emerges from this study is that monolayer TMDCs in the ballistic limit should display a remarkable variety of optical and electronic properties, many of which are yet to be verified experimentally. Nevertheless, the recent reports of achieving high-transparency contacts to these materials [188, 189] are promising a further rapid development of this field.

## 10. Acknowledgement

Andor Kormányos acknowledges discussion with Yi Zhang, Philip King, Diana Qiu, and Timothy Berkelbach. We also acknowledge support by the DFG through the SFB 767 and SFB 689, the EU through the Marie Curie ITN S3NANO, EC Graphene Flagship Project CNECT-ICT-604391, ERC Synergy Grant Hetero2D, Royal Society Wolfson Research Merit Award, and EPSRC Science and Innovation Award EP/G035954.

## Appendix A. Seven-band $\mathbf{k} \cdot \mathbf{p}$ model at the $K$ ( $-K$ ) point

In this section we give a brief account of the seven-band  $\mathbf{k} \cdot \mathbf{p}$  model, which lies behind the effective Hamiltonian of Equation (2). The following discussion is based on our previous work published in References [49] and [60]; we believe it is helpful to present the main steps here again to make this work self-contained.

Our seven-band model (without spin) contains every band between the third band below the VB (which we denote by VB-3) and the second band above the CB (denoted by CB+2), i.e., we take the basis  $\{|\Psi_{E'_2}^{\text{vb}-3}, s\rangle, |\Psi_{E'_1}^{\text{vb}-2}, s\rangle, |\Psi_{E''_2}^{\text{vb}-1}, s\rangle, |\Psi_{A'}^{\text{vb}}, s\rangle, |\Psi_{E'_1}^{\text{cb}}, s\rangle, |\Psi_{A''}^{\text{cb}+1}, s\rangle, |\Psi_{E'_1}^{\text{cb}+2}, s\rangle\}$ . The upper index  $b = \{\text{vb} - 3, \text{vb} - 2, \text{vb} - 1, \text{vb}, \text{cb}, \text{cb} + 1, \text{cb} + 2\}$  denotes the band, the lower index  $\mu$  indicates the pertinent irreducible representation of the point group  $C_{3h}$ , which gives the symmetry of the bands at the  $K$  point of the BZ (see Table A1 for the character table of  $C_{3h}$ ). The spinful symmetry basis functions are introduced by  $|\Psi_{\mu}^b, s\rangle = |\Psi_{\mu}^b\rangle \otimes |s\rangle$ , where  $s = \{\uparrow, \downarrow\}$  denotes the spin degree of freedom. An important symmetry of the system is that it has a horizontal mirror plane. As a consequence, the basis states can be grouped into two sets: the first one contains states whose orbital part is symmetric (even) with respect to the mirror operation  $\sigma_h: \sigma_h |\Psi_{\mu}^b\rangle = |\Psi_{\mu}^b\rangle$ . This first group contains the following states:  $\{|\Psi_{A'}^{\text{vb}}, s\rangle, |\Psi_{E'_1}^{\text{cb}}, s\rangle, |\Psi_{E'_2}^{\text{vb}-3}, s\rangle, |\Psi_{E'_1}^{\text{cb}+2}, s\rangle\}$ . The second set contains antisymmetric (odd) states:  $\sigma_h |\Psi_{\mu}^b\rangle = -|\Psi_{\mu}^b\rangle$ . The corresponding states are  $\{|\Psi_{E''_1}^{\text{vb}-2}, s\rangle, |\Psi_{E''_2}^{\text{vb}-1}, s\rangle, |\Psi_{A''}^{\text{cb}+1}, s\rangle\}$ .

**Table A1.** Character table for the group  $C_{3h}$  ( $\bar{6}$ ). Here  $\omega = e^{\frac{2i\pi}{3}}$ .

$C_{3h}$	$E$	$C_3$	$C_3^2$	$\sigma_h$	$S_3$	$\sigma_h C_3^2$
$A'$	1	1	1	1	1	1
$A''$	1	1	1	-1	-1	-1
$E'_1$	1	$\omega$	$\omega^2$	1	$\omega$	$\omega^2$
$E'_2$	1	$\omega^2$	$\omega$	1	$\omega^2$	$\omega$
$E''_1$	1	$\omega$	$\omega^2$	-1	$-\omega$	$-\omega^2$
$E''_2$	1	$\omega^2$	$\omega$	-1	$-\omega^2$	$-\omega$

Two important questions can be raised at this point:

- i) What is the motivation to include seven bands in the model and not more (or less)?
- ii) How can we identify the irreducible representation of  $C_{3h}$  according to which a given band transforms?

To answer i), we remind the reader that, as mentioned in Section 5.3, a strictly two-band model, such as the one introduced in Reference [26] (see Equation (5)) cannot describe, e.g., the TW of the bands or the details of the spin-splitting in the CB. In  $\mathbf{k} \cdot \mathbf{p}$  theory these effects can be understood as arising from the coupling of the VB and CB to other energy bands. As a first step, let us neglect the SOC. The operator  $\mathcal{H}_{\mathbf{k}, \mathbf{p}}$  which describes the interaction of various bands in  $\mathbf{k} \cdot \mathbf{p}$  theory (see Equation (A.2))



below) is symmetric with respect to  $\sigma_h$ :  $\sigma_h^{-1} \mathcal{H}_{\mathbf{k}, \mathbf{p}} \sigma_h = \mathcal{H}_{\mathbf{k}, \mathbf{p}}$ . Therefore, non-zero matrix elements  $\langle \Psi_{\mu}^b, s | \mathcal{H}_{\mathbf{k}, \mathbf{p}} | \Psi_{\mu'}^{b'}, s \rangle$  only exist between states  $|\Psi_{\mu}^b, s\rangle$  and  $|\Psi_{\mu'}^{b'}, s\rangle$  whose orbital parts are either both even or both odd with respect to  $\sigma_h$ . A natural extension of a model containing only the VB and the CB is to include one more band, which, regarding its energy, is below the VB and one above the CB. The symmetry properties of individual bands can be extracted from DFT band-structure calculations. We found that, at the  $K$  and  $-K$  points, the first symmetric band below the VB is the VB-3 and the first even band above the CB is the CB+2 band. Thus we arrive at a four-band model containing  $\{|\Psi_{A'}^{\text{vb}}, s\rangle, |\Psi_{E_1'}^{\text{cb}}, s\rangle, |\Psi_{E_2'}^{\text{vb}-3}, s\rangle, |\Psi_{E_1'}^{\text{cb}+2}, s\rangle\}$ . This four-band model can already describe the electron-hole asymmetry and the TW of the spectrum [60]. The next step is to take into account the SOC. In the atomic approximation the corresponding Hamiltonian is given by Equation (A.3). This Hamiltonian can have non-zero matrix elements between even and odd states. Since our aim is, ultimately, to obtain an effective Hamiltonian describing the coupled dynamics of the VB and the CB, it is natural to enlarge our basis of four even states by those odd states which, regarding their energy, lie between VB-3 and CB+2: these are  $\{|\Psi_{E_1''}^{\text{vb}-2}, s\rangle, |\Psi_{E_2''}^{\text{vb}-1}, s\rangle, |\Psi_{A''}^{\text{cb}+1}, s\rangle\}$ . In this way we set up a seven-band model, as indicated above.

As for question ii), we next discuss how to find out the symmetries of the bands. Some DFT codes, such as WIEN2k [190], can directly provide this information. If this is not available, many DFT codes can calculate the projection of the Kohn-Sham wave functions of each energy band onto atomic orbitals  $\Phi_{\nu}^{\eta}$ , where  $\eta = \{\text{M}, \text{X1}, \text{X2}\}$  denotes whether the given orbital is centred on the metal (M) or on one of the chalcogen (X1, X2) atoms in the unit cell, and the lower index  $\nu = \{s, p_x, p_y, p_z, d_{z^2}, d_{xy}, d_{xz}, d_{yz}, d_{x^2-y^2}\}$  indicates the type of orbital. Such a calculation is also shown in Figure 3. To take into account the three-fold rotational symmetry of the system, we use linear combinations of these orbitals to form spherical harmonics  $Y_l^m$ . We then consider the transformation properties of the Bloch wave functions formed with these spherical harmonics:

$$\Psi_{l,m}^{\eta}(\mathbf{k}, \mathbf{r}) = \frac{1}{\sqrt{N}} \sum_{\mathbf{R}_n} e^{i\mathbf{k} \cdot (\mathbf{R}_n + \mathbf{t}_{\eta})} Y_l^m(\mathbf{r} - [\mathbf{R}_n + \mathbf{t}_{\eta}]). \quad (\text{A.1})$$

Here the summation runs over all lattice vectors  $\mathbf{R}_n$ ,  $\mathbf{t}_M$  and  $\mathbf{t}_{X1} = \mathbf{t}_{X2}$  give the positions of the metal and chalcogen atoms in the 2D unit cell, and the wavevector  $\mathbf{k}$  is measured from the  $\Gamma$  point of the BZ. By examination one can then find out how the Bloch wave functions  $\Psi_{l,m}^{\eta}(\mathbf{k}, \mathbf{r})$  transform at, e.g., the  $\mathbf{k} = K$  point of the BZ when the reflection  $\sigma_h$  or the rotation by  $2\pi/3$  around an axis perpendicular to the plane of the monolayer (denoted by  $C_3$ ) is applied. Considering first  $\sigma_h$ , it is clear that the  $d$  orbitals of the M atoms are either even ( $\{d_{z^2}, d_{xy}, d_{x^2-y^2}\}$ ) or odd ( $\{d_{xz}, d_{yz}\}$ ). Regarding the  $p$  orbitals of the X1 and X2 atoms, which are above and below the plane of the M atoms, one can also form linear combinations of  $\Psi_{l,m}^{X1}(\mathbf{k}, \mathbf{r})$  and  $\Psi_{l,m}^{X2}(\mathbf{k}, \mathbf{r})$  which are either even or odd (see Table A2).

The Bloch wave functions of Equation (A.1) are also eigenstates of the rotation operation  $C_3$  with an eigenvalue  $\lambda_{l,m}^{\eta}$ :  $C_3 \Psi_{l,m}^{\eta} = \lambda_{l,m}^{\eta} \Psi_{l,m}^{\eta}$ . At the  $\mathbf{k} = K$  or  $-K$  points,

**Table A2.** Basis functions for the irreducible representations of the  $C_{3h}$  group of the  $K$  point. The rightmost column shows the band to which a given basis function contribute. The basis functions for the  $K'$  point can be obtained by complex-conjugation.

irrep	basis functions	band
$A'$	$\Psi_{2,-2}^M, \frac{1}{\sqrt{2}} (\Psi_{1,-1}^{X1} + \Psi_{1,-1}^{X2})$	VB
$A''$	$\Psi_{2,1}^M, \frac{1}{\sqrt{2}} (\Psi_{1,-1}^{X1} - \Psi_{1,-1}^{X2})$	CB+1
$E'_1$	$ \Psi_{2,0}^M\rangle, \frac{1}{\sqrt{2}} (\Psi_{1,1}^{X1} + \Psi_{1,1}^{X2})$	CB
$E'_2$	$\Psi_{2,2}^M, \frac{1}{\sqrt{2}} (\Psi_{1,0}^{X1} -  \Psi_{1,0}^{X2})$	VB-3 CB+2
$E''_1$	$ \Psi_{1,0}^M\rangle, \frac{1}{\sqrt{2}} (\Psi_{1,1}^{X1} - \Psi_{1,1}^{X2})$	VB-2
$E''_2$	$\Psi_{2,-1}^M, \frac{1}{\sqrt{2}} (\Psi_{1,0}^{X1} + \Psi_{1,0}^{X2})$	VB-1

$\lambda_{l,m}^\eta$  can take on one of the following three values: 1,  $e^{i\frac{2\pi}{3}}$ ,  $e^{-i\frac{2\pi}{3}}$  (see Table A1). Note that  $C_3$  acts on both the spherical harmonics part  $Y_l^m(\mathbf{r})$  and on the plane-wave component  $e^{i\mathbf{k}\cdot(\mathbf{R}_n+\mathbf{t}_\eta)}$  in  $\Psi_{l,m}^\eta(\mathbf{k}, \mathbf{r})$  [58], because in a rotated coordinate system the vectors  $\mathbf{t}_M$  and  $\mathbf{t}_X$  are also transformed. For this reason the eigenvalues  $\lambda_{l,m}^\eta$  corresponding to  $\Psi_{l,m}^\eta(\mathbf{k} = \pm K, \mathbf{r})$  depend on the choice of the unit cell, which determines the centre of rotation. In our case the unit cell is defined in Figure 1(b) and the centre of rotation is the centre of the hexagon formed by the M and X atoms. Other possible choices are, e.g., the position of the M or the X atoms (see, e.g., Table 2 in Reference [76]). Once the eigenvalues of  $\Psi_{l,m}^\eta(\mathbf{k} = \pm K, \mathbf{r})$  under the action of  $\sigma_h$  and  $C_3$  are known, a symmetry label, e.g.,  $A'$  or  $E'$ , of an irreducible representation can be assigned to each state. These are listed in Table A2. In the single-particle picture hybridisation between different Bloch wave functions should preserve symmetry properties; hence, e.g., the CB at the  $K$  point can be thought of as a linear combination of  $\Psi_{2,0}^M$  and  $\frac{1}{\sqrt{2}} (\Psi_{1,1}^{X1} + \Psi_{1,1}^{X2})$  (third row in Table A2). The corresponding Bloch wave functions at the  $-K$  point can be obtained by complex conjugation, because the  $K$  and  $-K$  points are connected by time-reversal.

The above discussion illustrates how symmetries of each band at each high-symmetry point in the BZ can be found and used to construct effective Hamiltonians. It is important to point out the following: although, as mentioned above, the eigenvalues with respect to  $C_3$  and hence the assignment of irreducible representations may depend on the choice of the rotation centre, the form of the Hamiltonian (2), up to a unitary transformation, does not depend on such choices.

Appendix A.1.  $\mathbf{k} \cdot \mathbf{p}$  matrix elements

The  $\mathbf{k} \cdot \mathbf{p}$  matrix elements, which characterise the coupling of the bands away from the  $K$  and  $-K$  points, are calculated using the Hamiltonian

$$\mathcal{H}_{\mathbf{k},\mathbf{p}} = \frac{1}{2} \frac{\hbar}{m_e} (q_+ \hat{p}_- + q_- \hat{p}_+) = \mathcal{H}_{\mathbf{k},\mathbf{p}}^- + \mathcal{H}_{\mathbf{k},\mathbf{p}}^+, \quad (\text{A.2})$$

where  $\hat{p}_\pm = \hat{p}_x \pm i\hat{p}_y$  are momentum operators. As the operator (A.2) does not contain spin-operators, the matrix elements are diagonal in the spin-space. Furthermore, the matrix elements of  $\mathcal{H}_{\mathbf{k},\mathbf{p}}$  are constrained by the symmetries of the states with respect to  $C_3$ . Namely, the relation  $\langle \Psi_{A'}^{\text{vb}} | \hat{p}_+ | \Psi_{E_2'}^{\text{cb}+2} \rangle = \langle \Psi_{A'}^{\text{vb}} | C_3^\dagger C_3 \hat{p}_+ C_3^\dagger C_3 | \Psi_{E_2'}^{\text{cb}+2} \rangle$  should hold. Since  $\langle \Psi_{A'}^{\text{vb}} | C_3^\dagger = \langle \Psi_{A'}^{\text{vb}} |$ ,  $C_3 \hat{p}_\pm C_3^\dagger = e^{\mp i2\pi/3} \hat{p}_\pm$  and  $C_3 | \Psi_{E_2'}^{\text{cb}+2} \rangle = e^{-i2\pi/3} | \Psi_{E_2'}^{\text{cb}+2} \rangle$  one obtains that  $\langle \Psi_{A'}^{\text{vb}} | \mathcal{H}_{\mathbf{k},\mathbf{p}}^+ | \Psi_{E_2'}^{\text{cb}+2} \rangle = e^{-i4\pi/3} \langle \Psi_{A'}^{\text{vb}} | \mathcal{H}_{\mathbf{k},\mathbf{p}}^+ | \Psi_{E_2'}^{\text{cb}+2} \rangle$ , which means that this matrix element must vanish. By contrast,  $\langle \Psi_{A'}^{\text{vb}} | \mathcal{H}_{\mathbf{k},\mathbf{p}}^- | \Psi_{E_2'}^{\text{cb}+2} \rangle = \gamma_4$  is allowed to be finite.

The matrix elements  $H_{\mathbf{k},\mathbf{p}}^K$  calculated at the  $K$  point of the BZ are shown in Table A3, where the diagonal elements are the band-edge energies. The matrix elements at the  $-K$  point can be obtained with the substitutions  $\gamma_i \rightarrow \gamma_i^*$  and  $q_\pm \rightarrow -q_\mp$ .

**Table A3.** Matrix elements of  $\mathcal{H}_{\mathbf{k},\mathbf{p}}$  at the  $K$  point.

$H_{\mathbf{k},\mathbf{p}}^K$	$ \Psi_{A'}^{\text{vb}}, s\rangle$	$ \Psi_{E_1'}^{\text{cb}}, s\rangle$	$ \Psi_{E_2'}^{\text{vb}-3}, s\rangle$	$ \Psi_{E_2'}^{\text{cb}+2}, s\rangle$	$ \Psi_{E_1''}^{\text{vb}-2}, s\rangle$	$ \Psi_{E_2''}^{\text{vb}-1}, s\rangle$	$ \Psi_{A''}^{\text{cb}+1}, s\rangle$
$ \Psi_{A'}^{\text{vb}}, s\rangle$	$\varepsilon_v$	$\gamma_3 q_-$	$\gamma_2 q_+$	$\gamma_4 q_+$	0	0	0
$ \Psi_{E_1'}^{\text{cb}}, s\rangle$	$\gamma_3^* q_+$	$\varepsilon_c$	$\gamma_5 q_-$	$\gamma_6 q_-$	0	0	0
$ \Psi_{E_2'}^{\text{vb}-3}, s\rangle$	$\gamma_2^* q_-$	$\gamma_5^* q_+$	$\varepsilon_{v-3}$	0	0	0	0
$ \Psi_{E_2'}^{\text{cb}+2}, s\rangle$	$\gamma_4^* q_-$	$\gamma_6^* q_+$	0	$\varepsilon_{c+2}$	0	0	0
$ \Psi_{E_1''}^{\text{vb}-2}, s\rangle$	0	0	0	0	$\varepsilon_{v-2}$	$\gamma_8 q_-$	$\gamma_7 q_+$
$ \Psi_{E_2''}^{\text{vb}-1}, s\rangle$	0	0	0	0	$\gamma_8^* q_+$	$\varepsilon_{v-1}$	$\gamma_9^* q_-$
$ \Psi_{A''}^{\text{cb}+1}, s\rangle$	0	0	0	0	$\gamma_7^* q_-$	$\gamma_9^* q_+$	$\varepsilon_{c+1}$

Concrete values for the parameters  $\gamma_i$  can be obtained for each material by, e.g., directly evaluating the matrix elements  $\langle \Psi_\mu^b | \hat{p}_\pm | \Psi_{\mu'}^{b'} \rangle$  using Kohn–Sham orbitals. We used this method to calculate the values denoted by  $\gamma_{\text{KS}}$  in Tables 6 and 7.

Appendix A.2. Spin–orbit coupling

In the atomic approximation the SOC is given by the Hamiltonian

$$\mathcal{H}_{\text{so}}^{\text{at}} = \frac{\hbar}{4m_e^2 c^2} \frac{1}{r} \frac{dV(r)}{dr} \hat{\mathbf{L}} \cdot \hat{\mathbf{S}}, \quad (\text{A.3})$$

where  $V(r)$  is the spherically symmetric atomic potential,  $\hat{\mathbf{L}}$  is the angular-momentum operator, and  $\hat{\mathbf{S}} = (s_x, s_y, s_z)$  is a vector of spin Pauli matrices  $s_x$ ,  $s_y$ , and  $s_z$  (with eigenvalues  $\pm 1$ ). Note that  $\hat{\mathbf{L}} \cdot \hat{\mathbf{S}} = \hat{L}_z s_z + \hat{L}_+ s_- + \hat{L}_- s_+$ , where  $\hat{L}_\pm = \hat{L}_x \pm i\hat{L}_y$  and  $s_\pm = \frac{1}{2}(s_x \pm is_y)$ . The task is then to calculate the matrix elements of Equation (A.3) in the basis introduced earlier in this section.

The non-zero matrix elements  $H_{\text{so}}$  can be obtained by considering the transformation properties of the basis states and angular-momentum operators with respect to the mirror operation  $\sigma_h$  and the rotation  $C_3$ . Note that in contrast to the Hamiltonian in Table (A3), the SOC Hamiltonian shown in Table (A4) has non-zero matrix elements between symmetric and antisymmetric basis states as well. This is due to the fact that the  $\hat{L}_\pm$  operators are themselves antisymmetric with respect to  $\sigma_h$ . The full SOC Hamiltonian at  $K$  is shown in Table (A4).

**Table A4.** Matrix elements of  $\mathcal{H}_{\text{so}}^{\text{at}}$  at the  $K$  point.

$H_{\text{so}}^K$	$ \Psi_{A'}^{\text{vb}}, s\rangle$	$ \Psi_{E_1'}^{\text{cb}}, s\rangle$	$ \Psi_{E_2'}^{\text{vb}-3}, s\rangle$	$ \Psi_{E_2'}^{\text{cb}+2}, s\rangle$	$ \Psi_{E_1''}^{\text{vb}-2}, s\rangle$	$ \Psi_{E_2''}^{\text{vb}-1}, s\rangle$	$ \Psi_{A''}^{\text{cb}+1}, s\rangle$
$ \Psi_{A'}^{\text{vb}}, s\rangle$	$S_z \Delta_v$	0	0	0	$S_- \Delta_{v,v-2}$	$S_+ \Delta_{v,v-1}$	0
$ \Psi_{E_1'}^{\text{cb}}, s\rangle$	0	$S_z \Delta_c$	0	0	0	$S_- \Delta_{c,v-1}$	$S_+ \Delta_{c,c+1}$
$ \Psi_{E_2'}^{\text{vb}-3}, s\rangle$	0	0	$S_z \Delta_{v-3}$	$S_z \Delta_{v-3,c+2}$	$S_+ \Delta_{v-3,v-2}$	0	$S_- \Delta_{v-3,c+1}$
$ \Psi_{E_2'}^{\text{cb}+2}, s\rangle$	0	0	$S_z \Delta_{v-3,c+2}^*$	$S_z \Delta_{c+2}$	$S_+ \Delta_{c+2,v-2}$	0	$S_- \Delta_{c+2,c+1}$
$ \Psi_{E_1''}^{\text{vb}-2}, s\rangle$	$S_+ \Delta_{v,v-2}^*$	0	$S_- \Delta_{v-3,v-2}^*$	$S_- \Delta_{c+2,v-2}^*$	$S_z \Delta_{v-2}$	0	0
$ \Psi_{E_2''}^{\text{vb}-1}, s\rangle$	$S_- \Delta_{v,v-1}^*$	$S_+ \Delta_{c,v-1}^*$	0	0	0	$S_z \Delta_{v-1}$	0
$ \Psi_{A''}^{\text{cb}+1}, s\rangle$	0	$S_- \Delta_{c,c+1}^*$	$S_+ \Delta_{v-3,c+1}^*$	$S_+ \Delta_{c+2,c+1}^*$	0	0	$S_z \Delta_{c+1}$

The SOC Hamiltonian at  $-K$  can be obtained by making the following substitutions:  $|\Psi_{E_2'}^{\text{vb}-3}, s\rangle \rightarrow |\Psi_{E_1'}^{\text{vb}-3}, s\rangle$ ,  $|\Psi_{E_1'}^{\text{cb}}, s\rangle \rightarrow |\Psi_{E_2'}^{\text{cb}}, s\rangle$ ,  $|\Psi_{E_1''}^{\text{vb}-2}, s\rangle \rightarrow |\Psi_{E_2''}^{\text{vb}-2}, s\rangle$ ,  $|\Psi_{E_2''}^{\text{vb}-1}, s\rangle \rightarrow |\Psi_{E_1''}^{\text{vb}-1}, s\rangle$ ,  $\Delta_{b,b'} \rightarrow \Delta_{b,b'}^*$ ,  $S_\pm \rightarrow -S_\mp$ ,  $S_z \rightarrow -S_z$ . The change of the wave-function symmetry notation follows from the assumption that orbital wave functions at  $K$  and  $-K$  are connected by time-reversal symmetry, i.e.,  $|\Psi_\mu^b(K)\rangle = \hat{K}_0 |\Psi_{\mu'}^b(-K)\rangle$ , where  $\hat{K}_0$  denotes complex conjugation.

### Low-energy effective Hamiltonian

The low-energy effective Hamiltonian of Equation (4a) can be obtained from  $H_0 + H_{\mathbf{k},\mathbf{p}} + H_{\text{so}}$  by means of Löwdin partitioning (see, e.g., Reference [150]) by considering terms up to third order in various off-diagonal couplings.

## Appendix B. Fitting procedure at the $K$ point

The aim of this section is to explain the fitting procedure that we used to extract the material parameters that appear in the Hamiltonians of Equations (4b)–(4e) from our DFT calculations (see Tables 6 and 7). In order that the parameter sets obtained can be compared to other works, we think that it is important to give some details of the fitting procedure.

To simplify the notation, we consider the  $K$  point and suppress the  $\tau$  index. The eigenvalues of the low-energy Hamiltonian of Equation (2) read

$$E_{\pm}^{(s)} = \frac{\tilde{\varepsilon}_{\text{vb}} + \tilde{\varepsilon}_{\text{cb}}}{2} + \left( \frac{\hbar^2}{2m_e} + \frac{\alpha_s + \beta_s}{2} \right) \mathbf{q}^2 \pm \sqrt{\left( \frac{\tilde{\varepsilon}_{\text{cb}} - \tilde{\varepsilon}_{\text{vb}}}{2} + \frac{\beta_s - \alpha_s}{2} \mathbf{q}^2 \right)^2 + f(\mathbf{q})}, \quad (\text{B.1})$$

$$f(\mathbf{q}) = |\gamma|^2 \mathbf{q}^2 + |\mathbf{q}|^3 |\gamma| |\kappa_s| [2 \cos(\theta_{\kappa_s \gamma} + 3\varphi_{\mathbf{q}}) + \mathbf{q}^4 [|\kappa_s|^2 - |\gamma| |\eta_s| \cos(\theta_{\eta_s \gamma})]] \quad (\text{B.2})$$

where  $\tilde{\varepsilon}_{\text{vb}} = \varepsilon_{\text{vb}} + \tau s \Delta_{\text{vb}}$  and similarly for  $\tilde{\varepsilon}_{\text{cb}}$ ,  $\varphi_{\mathbf{q}} = \arctan(q_y/q_x)$ ,  $\theta_{\kappa_s \gamma}$  ( $\theta_{\eta_s \gamma}$ ) are the relative phase of  $\kappa_s$  and  $\gamma$  ( $\eta_s$  and  $\gamma$ ), and  $+$  ( $-$ ) sign corresponds to the CB (VB). Since Equation (B.1) depends on the parameters  $\gamma$ ,  $\alpha_s$ ,  $\beta_s$ ,  $\kappa_s$ , and  $\eta_s$  in a non-linear way, some care has to be taken in the fitting procedure.

First, one can determine  $|\gamma|$ ,  $\alpha_s$ , and  $\beta_s$  in the following way. For small enough  $\mathbf{q}$ , the largest energy scale under the square root in Equation (B.1) is the band gap (for a given spin  $s$ )  $E_{\text{bg}}^{(s)} = \tilde{\varepsilon}_{\text{cb}} - \tilde{\varepsilon}_{\text{vb}}$ . Expanding the square root one finds

$$\begin{aligned} E_+^{(s)} &\approx \tilde{\varepsilon}_{\text{cb}} + \left( \frac{\hbar^2}{2m_e} + \beta_s + \frac{|\gamma|^2}{E_{\text{bg}}^{(s)}} \right) \mathbf{q}^2 \\ E_-^{(s)} &\approx \tilde{\varepsilon}_{\text{vb}} + \left( \frac{\hbar^2}{2m_e} + \alpha_s - \frac{|\gamma|^2}{E_{\text{bg}}^{(s)}} \right) \mathbf{q}^2. \end{aligned} \quad (\text{B.3})$$

In this approximation  $E_{\pm}^{(s)}$  is described by a simple parabolic dispersion where the effective masses are given by

$$\frac{\hbar^2}{2m_{\text{cb}}^{(s)}} = \left( \frac{\hbar^2}{2m_e} + \beta_s + \frac{|\gamma|^2}{E_{\text{bg}}^{(s)}} \right) \quad (\text{B.4})$$

$$\frac{\hbar^2}{2m_{\text{vb}}^{(s)}} = \left( \frac{\hbar^2}{2m_e} + \alpha_s - \frac{|\gamma|^2}{E_{\text{bg}}^{(s)}} \right) \quad (\text{B.5})$$

Since  $E_{\text{bg}}^{(s)}$  can be directly read off from the DFT calculations and  $2m_{\text{cb}}^{(s)}$  and  $2m_{\text{vb}}^{(s)}$  can be obtained by fitting the CB and VB in the vicinity of the  $K$  point with a parabola, Equations (B.4)–(B.5) constitute four equations for five unknown parameters  $|\gamma|$ ,  $\alpha_s$ , and  $\beta_s$ . As explained in Section 5.2, the fitting around  $K$  was done in a range that corresponds to 5% of the  $\Gamma$ – $K$  distance. The dispersion over this range can be considered to be isotropic and the difference in the effective masses along  $K$ – $\Gamma$  and  $K$ – $M$  can be neglected. Over the same range in  $\mathbf{q}$ , one can also fit the function  $\frac{\tilde{\varepsilon}_{\text{vb}} + \tilde{\varepsilon}_{\text{cb}}}{2} + c_1^{(s)} \mathbf{q}^2 + \sqrt{(E_{\text{bg}}^{(s)})^2/4 + c_2^{(s)} \mathbf{q}^2}$  to the CB and the function

$\frac{\tilde{\epsilon}_{\text{vb}} + \tilde{\epsilon}_{\text{cb}}}{2} + c_1^{(s)} \mathbf{q}^2 - \sqrt{(E_{\text{bg}}^{(s)})^2/4 + c_2^{(s)} \mathbf{q}^2}$  to the VB such that the fitting parameters  $c_1^{(s)}$  and  $c_2^{(s)}$  simultaneously give the best fit to the dispersion both in the CB and in the VB. Comparing to Equation (B.1), one can see that this corresponds to

$$\frac{\alpha_s + \beta_s}{2} = c_1^{(s)} - \frac{\hbar^2}{2m_e}, \quad (\text{B.6})$$

$$\frac{\beta_s - \alpha_s}{2} + |\gamma|^2 = \frac{2c_2^{(s)}}{E_{\text{bg}}^{(s)}}, \quad (\text{B.7})$$

i.e., we have obtained four more equations for  $|\gamma|$ ,  $\alpha_s$ , and  $\beta_s$ . Using Equations (B.4)–(B.7) one finds eight equations for the five unknown parameters  $|\gamma|$ ,  $\alpha_s$ , and  $\beta_s$ , which can be solved as a linear least-squares problem. The solution, however, depends on the value of the quasiparticle band gap  $E_{\text{bg}}^{(s)}/2$  used in the least-squares problem. As shown in Table 5 this is significantly underestimated in DFT calculations. Therefore we have performed the fitting using both the DFT band gap and the *GW* gap. Note that in order to find  $E_{\text{bg}}^{(s)}$  one has to add to the  $E_{\text{bg}}$  values shown in Table 5 the relevant spin-splitting energies, which can be found in Tables 3 and 4. The two approach lead to two sets of parameters. In both cases the *same* effective masses  $m_{\text{cb}}^{(s)}$  and  $m_{\text{vb}}^{(s)}$ , obtained from our DFT calculations, were used. Since the available experimental results suggest that DFT can capture the effective masses quite well, at least in the VB (see Tables 4 and 10), we think that this is a reasonable approach to take into account the results of *GW* calculations.

Finally the four remaining parameters  $\kappa_s$  and  $\eta_s$  were determined in following way. Similarly to the previous step, a function of the form

$$\frac{\tilde{\epsilon}_{\text{vb}} + \tilde{\epsilon}_{\text{cb}}}{2} + c_1^{(s)} \mathbf{q}^2 \pm \sqrt{(E_{\text{bg}}^{(s)})^2/4 + c_2^{(s)} \mathbf{q}^2 + c_3^{(s)} |\mathbf{q}|^3 \cos 3\phi_{\mathbf{q}} + c_4^{(s)} \mathbf{q}^4} \quad (\text{B.8})$$

was fitted to the VB and CB. Here  $c_1^{(s)}$  and  $c_2^{(s)}$  were kept fixed at the values that were obtained at the previous step and the parameters  $c_3^{(s)}$  and  $c_4^{(s)}$  were required to give the best fit simultaneously to both the CB and the VB. The fitting was performed along the  $\Gamma$ – $K$ – $M$  directions around  $K$  and the fitting range corresponded to  $\approx 16\%$  of the  $\Gamma$ – $K$  distance. Note, that  $\cos 3\phi_{\mathbf{q}} = -1$  ( $\cos 3\phi_{\mathbf{q}} = 1$ ) along  $\Gamma$ – $K$  ( $K$ – $M$ ). Since  $|\gamma|$ ,  $\alpha_s$ , and  $\beta_s$  are already know by this step,  $\kappa_s$  and  $\eta_s$  is calculated as  $\kappa_s = c_3^{(s)}/(2|\gamma|)$  and  $\eta_s = [(\beta_s - \alpha_s)^2/4 - c_4^{(s)}]/|\gamma|$  [c.f., Equation (B.1)].

## References

- [1] Bromley R A, Murray R B, and Yoffe A D, 1972 *J. Phys. C: Solid State Phys.* **5**, 759.
- [2] Mattheis L F, 1973 *Phys. Rev. B* **8**, 3719.
- [3] Mak K F, Lee C, Hone J, Shan J, and Heinz T F, 2010 *Phys. Rev. Lett.* **105**, 136805.
- [4] Splendiani A, Sun L, Zhang Y, Li T, Kim J, Chim Ch-Y, Galli G, and Wang F 2010 *Nano Letters* **10**, 1271.
- [5] Korn T, Heydrich S, Hirmer M, Schmutzler J, and Schüller C, 2011 *Appl. Phys. Lett.* **99**, 102109.
- [6] Jones A M, Yu H, Ghimire N, Wu S, Aivazian G, Ross J S, Zhao B, Yan J, Mandrus D, Xiao D, Yao W, and Xu X, 2013 *Nature Nanotechnology* **8**, 634.

- [7] Gan X, Gao Y, Mak K F, Yao X, Shiue R-J, van der Zande A, Trusheim M E, Hatami F, Heinz T F, Hone J, and Englund D, 2013 *Applied Physics Letters* **103**, 181119.
- [8] Wu S, Buckley S, Jones A M, Ross J S, Ghimire N J, Yan J, Mandrus D G, Yao W, Hatami F, Vučković J, Majumdar A, and Xu X, 2014 *2D Materials* **1**, 011001. doi:10.1088/2053-1583/1/1/011001
- [9] Liu X, Galfsky T, Sun Zh, Xia F, Lin E, Lee Y-H, Kéna-Cohen S, and Menon V M, 2015 *Nature Photonics* **9**, 30.
- [10] Sie E J, McIver J W, Lee Y-H, Frenzel A J, Fu L, Kong J, and Gedik N, 2014 *Nature Materials*, Advanced online publication (<http://dx.doi.org/10.1038/nmat4156>).
- [11] Wang G, Marie X, Gerber I, Amand T, Lagarde D, Bouet L, Vidal M, Balocchi A, and Urbaszek B, 2015 *Phys. Rev. Lett.* **114**, 097403.
- [12] Radisavljević B, Radenović A, Brivio J, Giacometti V, Kis, A, 2011 *Nature Nanotechnology* **6**, 147.
- [13] Lembke D and Kis A, 2012 *ACS Nano* **6**, 10070.
- [14] Fang H, Chuang S, Chang T C, Takei K, Takahashi T, and Javey A, 2012 *Nano Letters* **12**, 3788.
- [15] Wang H, Yu L, Lee Y H, Shi Y, Hsu A, Chin M, Li L J, Dubey M, Kong J, and Palacios T, 2012 *Nano Letters* **12**, 4674.
- [16] Liu W, Kang J, Sarkar D, Khatami Y, Jena D, and Banerjee K, 2013 *Nano Letters* **13**, 1983.
- [17] Kang J, Liu W, and Banerjee K, 2014 *Appl. Phys. Lett.* **104**, 093106.
- [18] Das S, Gulotty R, Sumant A V, and Roelofs A, 2014 *Nano Letters* **14**, 2861.
- [19] Radisavljević B, Whitwick M B, and Kis A, 2011 *ACS Nano*, **5**, 9934.
- [20] Britnell L, Ribeiro R M, Eckmann A, Jalil R, Belle B D, Mishchenko A, Kim Y-J, Gorbachev R V, Georgiou T, Morozov S V, Grigorenko A N, Geim A K, Casiraghi C, Castro Neto A H, and Novoselov K S, 2013 *Science* **340**, 1311.
- [21] Pospischil A, Furchi M M, and Mueller T, 2014 *Nature Nanotechnology* **9**, 257.
- [22] Ross J S, Klement Ph, Jones A M, Ghimire N J, Yan J, Mandrus D G, Taniguchi T, Watanabe K, Kitamura K, Yao W, Cobden D H, and Xu X, 2014 *Nature Nanotechnology* **9**, 268.
- [23] Baugher B W H, Churchill H O H, Yang Y, and Jarillo-Herrero P, 2014 *Nature Nanotechnology* **9**, 262.
- [24] Jo S, Ubrig N, Berger H, Kuzmenko A B, and Morpurgo A F, 2014 *Nano Letters* **14**, 2019.
- [25] Yao W, Xiao D, and Niu Q, 2008 *Phys. Rev. B* **77**, 235406.
- [26] Xiao D, Liu G B, Feng W, Xu X, and Yao W, 2012 *Phys. Rev. Lett.* **108**, 196802.
- [27] Mak K F, He K, Shan J, and Heinz T F, 2012 *Nature Nanotechnology* **7**, 494.
- [28] Zeng H, Dai J, Yao W, Xiao D, and Cui X, 2012 *Nature Nanotechnology* **7**, 490.
- [29] Cao T, Wang G, Han W, Ye H, Zhu Ch, Shi J, Niu Q, Tan P, Wang E, Liu B, and Feng J, 2012 *Nature Communications* **3**, 887.
- [30] Sallen G, Bouet L, Marie X, Wang G, Zhu C R, Han W P, Lu Y, Tan P H, Amand T, Liu B L, and Urbaszek B, 2012 *Phys. Rev. B* **86**, 081301.
- [31] Kioseoglou G, Hanbicki A T, Currie M, Friedman A L, Gunlycke D, and Jonker B T, 2012 *Appl. Phys. Lett.* **101**, 221907.
- [32] Rostami H, Moghaddam A G, and Asgari R, 2013 *Phys. Rev. B* **88**, 085440.
- [33] Zahid F, Liu L, Zhu Y, Wang J, and Guo H, 2013 *AIP Advances* **3**, 052111.
- [34] Liu G B, Shan W Y, Yao Y, Yao W, and Xiao D, 2013 *Phys. Rev. B* **88**, 085433.
- [35] Cappelluti E, Roldán R, Silva-Guillén J A, Ordejón P, and Guinea F, 2013 *Phys. Rev. B* **88**, 075409.
- [36] Kośmider K, González J W, and Fernández-Rossier J, *Phys. Rev. B* **88**, 245436 (2013).
- [37] Roldán R, López-Sancho M R, Cappelluti E, Silva-Guillén J A, Ordejón P, and Guinea F, 2014 *2D Materials* **1**, 034003.
- [38] Ghorbani-Asl M, Enyashin A N, Kuc A, Seifert G, and Heine T, 2013 *Phys. Rev. B* **88**, 245440.
- [39] Kaasbjerg K, Thygesen K S, and Jacobsen K W, 2012 *Phys. Rev. B* **85**, 115317.
- [40] Li X, Mullen J T, Jin Z, Borysenko K M, Nardelli M B, and Kim K W, 2013 *Phys. Rev. B* **87**,

- 115418.
- [41] Kaasbjerg K, Thygesen K S, and Jauho A-P, 2013 *Phys. Rev. B* **87**, 235312.
  - [42] Ge Y, Wan W, Feng W, Xiao D, and Yao Y 2014 *Phys. Rev. B* **90**, 035414.
  - [43] Chang J, Register L F, and Banerjee S K, 2014 *Journal of Applied Physics*, **115**, 084506.
  - [44] Gong K, Zhang L, Liu D, Liu L, Zhu Y, Zhao Y, and Guo H, 2014 *Nanotechnology* **25**, 435201.
  - [45] Ramasubramaniam A, 2012 *Phys. Rev. B* **86**, 115409.
  - [46] Komsa H P and Krasheninnikov A V, 2012 *Phys. Rev. B* **86**, 241201(R).
  - [47] Qiu D Y, da Jornada F H, and Louie S G, 2013 *Phys. Rev. Lett.* **111**, 216805.
  - [48] Molina-Sánchez A, Sangalli D, Hummer K, Marini A, and Wirtz L, 2013 *Phys. Rev. B* **88**, 045412.
  - [49] Kormányos A, Zólyomi V, Drummond N D, and Burkard G, 2014 *Phys. Rev. X* **4**, 011034.
  - [50] Liu G-B, Pang H, Yao Y, and Yao W, 2014 *New Journal of Physics* **16**, 105011.
  - [51] Li X, Zhang F, and Niu Q, 2013 *Phys. Rev. Lett.* **110**, 066803.
  - [52] Rose F, Goerbig M O, and Piéchon F, 2013 *Phys. Rev. B*, **88** 125438.
  - [53] Ho Y H, Wang Y H, and Chen H Y, 2014 *Phys. Rev. B* **89**, 155316.
  - [54] Chu R L, Li X, Wu S, Niu Q, Xu X, and Zhang Ch 2014 *Phys. Rev. B* **90**, 045427.
  - [55] Ganchev B, Drummond N D, Aleiner I, and Fal'ko V, 2015 *Phys. Rev. Lett.* **114**, 107401.
  - [56] Luttinger J M and Kohn W, 1955 *Phys. Rev.* **97**, 869.
  - [57] Bir G and Pikus G, 1974 *Symmetry and Strain-Induced Effects in Semiconductors* (Wiley, New York)
  - [58] Dresselhaus M S, Dresselhaus G, and Jorio A, 2008 *Group Theory (Application to the Physics of Condensed Matter)*, (Springer-Verlag Berlin Heidelberg).
  - [59] Lew Yan Voon L C and Willatzen M, 2009 *The k · p Method* (Springer-Verlag Berlin Heidelberg).
  - [60] Kormányos A, Zólyomi V, Drummond N D, Rakyta P, Burkard G, and Fal'ko V I, 2013 *Phys. Rev. B* **88**, 045416.
  - [61] Dawson W G and Bullett D W, 1987 *J. Phys. C: Solid State Phys* **20**, 6159.
  - [62] Böker Th, Severin R, Müller A, Janowitz C, Manzke R, Voß D, Krüger P, Mazur A, and Pollmann J, 2001 *Phys. Rev. B* **64** 235305.
  - [63] Coleman J N, Lotya M, O'Neill A, Bergin Sh D, King P J, Khan U, Young K, Gaucher A, De S, Smith R J, Shvets I V, Arora S K, Stanton G, Kim H-K, Lee K, Kim G T, Duesberg G S, Hallam T, Boland J J, Wang J J, Donegan J F, Grunlan J C, Moriarty G, Shmeliov A, Nicholls R J, Perkins J M, Grievson E M, Theuwissen K, McComb D W, Nellist P D, and Nicolosi V, 2011 *Science* **331**, 568.
  - [64] Lezama I G, Ubaldini A, Longobardi M, Giannini E, Renner Ch, Kuzmenko A B, and Morpurgo A F, 2014 *2D Materials* **1**, 021002.
  - [65] Brown B E, 1966 *Acta Cryst.* **20**, 268.
  - [66] Augustin J, Eyert V, Böker Th, Frentrup W, Dwelk H, Janowitz C, and Manzke R, 2000 *Phys. Rev. B* **62**, 10812.
  - [67] Kresse G and Furthmüller J, 1996 *Phys. Rev. B* **54**, 11169.
  - [68] See <http://www.flapw.de/>
  - [69] Geim A K and Novoselov K S, 2007 *Nature Materials* **6**, 183.
  - [70] Castro Neto A H, Guinea F, Peres N M R, Novoselov K S, and Geim A K, 2009 *Rev. Mod. Phys.* **81**, 109.
  - [71] Bonaccorso F, Sun Z, Hasan T Ferrari A C, 2010 *Nature Photonics* **4**, 611.
  - [72] Han W, Kawakami R K, Gmitra M, and Fabian J, 2014 *Nature Nanotechnology* **9**, 794.
  - [73] Wang Q H, Kalantar-Zadeh K, Kis A, Coleman J N, and Strano M S, 2012 *Nature Nanotechnology* **7**, 699.
  - [74] Xu X, Yao W, Xiao D, and Heinz T F, 2014 *Nature Physics* **10**, 343.
  - [75] Yazyev O V and Kis A, 2014 *Materials Today*, **18**, 20. (<http://dx.doi.org/10.1016/j.mattod.2014.07.005>)
  - [76] Liu G-B, Xiao D, Yao Y, Xu X, and Yao W, 2015 *Chem. Soc. Rev.*, Advance Article (<http://dx.doi.org/10.1039/C4CS00301B>).



- [77] Jariwala D, Sangwan V K, Lauhon L J, Marks T J, and Hersam M C, 2014 *ACS Nano* **8**, 1102.
- [78] Ganatra R and Zhang Q, 2014 *ACS Nano* **8**, 4074.
- [79] Roldán R, Silva-Guillén J A, López-Sancho M P, Guinea F, Cappelluti E, Ordejón P, 2014 *Ann. Phys. (Berlin)* **526**, 347.
- [80] Zibouche N, Kuc A, Musfeldt J, and Heine T, 2014 *Ann. Phys. (Berlin)* **526**, 395.
- [81] Shi H, Pan H, Yong-Wei Zhang Y W, and Yakobson B I, 2013 *Phys. Rev. B* **87**, 155304.
- [82] Heyd J, Scuseria G E, and Ernzerhof M, 2006 *J. Chem. Phys.* **124**, 219906.
- [83] Perdew J P, Burke K, and Ernzerhof M, 1996 *Phys. Rev. Lett.* **77**, 3865.
- [84] Kang J, Tongay S, Zhou J, Li J, and Wu J, 2013 *Appl. Phys. Lett.* **102**, 012111.
- [85] Lagarde D, Bouet L, Marie X, Zhu C R, Liu B L, Amand T, Tan P H, and Urbaszek B, 2014 *Phys. Rev. Lett.* **112**, 047401.
- [86] Zhang C, Wang H, Chan W, Manolatou C, and Rana F, 2014 *Phys. Rev. B* **89**, 205436.
- [87] Soklaski R, Liang Y, and Yang L, 2014 *Appl. Phys. Lett.* **104**, 193110.
- [88] Wilson J A and Yoffe A D, 1969 *Advances in Physics*, **18:73**, 193.
- [89] Yang D and Frindt R F, 1995 *J. Phys. Chem. Solids* **57**, 1113.
- [90] Al-Hilli A A and Evans B L, 1972 *Journal of Crystal Growth* **15**, 93.
- [91] Schutte W J, de Boer J L, and Jellinek F, 1987 *Journal of Solid State Chemistry* **70**, 207.
- [92] Bronsema K D, de Boer J L, and Jellinek F, 1986 *Z. Anorg. Allg. Chem.* **540**, 15.
- [93] Evans B L and Hazelwood R A, 1971 *Phys. Stat. Sol. (a)* **4**, 181.
- [94] Poutinen D and Newnham R E, 1961 *Acta Crystallographica* **14**, 691.
- [95] Young P A, 1968 *Brit. J. Appl. Phys. (J. Phys. D)*, **1**, 932.
- [96] Song Y and Dery H, 2013 *Phys. Rev. Lett.* **111**, 026601.
- [97] Molina-Sánchez A and Wirtz L, 2011 *Phys. Rev. B* **84** 155413.
- [98] Horzum S, Sahin H, Cahangirov S, Cudazzo P, Rubio A, Serin T, and Peeters F M, 2013 *Phys. Rev. B* **87**, 125415.
- [99] Sahin H, Tongay S, Horzum S, Fan W, Zhou J, Li J, Wu J, and Peeters F M, 2013 *Phys. Rev. B* **87**, 165409.
- [100] Ribeiro-Soares J, Almeida R M, Barros E B, Araujo P T, Dresselhaus M S, Cançado L G, and Jorio A, 2014 *Phys. Rev. B* **90**, 115438.
- [101] Ding Y, Wang Y, Ni J, Shi L, Shi S, and Tang W, 2011 *Physica B* **406**, 2254.
- [102] Luo X, Zhao Y Y, Zhang J, Toh M L, Kloc C, Xiong Q H, and Quek S Y, 2013 *Phys. Rev. B* **88**, 195313.
- [103] Zhao W J, Ghorannevis Z, Amara K K, Pang J R, Toh M, Zhang X, Kloc C, Tan P H, and Eda G, 2013 *Nanoscale* **5**, 9677.
- [104] Li H, Zhang Q, Yap C C R, Tay B K, Edwin T H T, Olivier A, and Baillargeat D, 2012 *Adv. Func. Materials* **22**, 1385.
- [105] Klimeš J, Bowler D R, and Michaelides A, 2010 *J. Phys.: Cond. Matt.* **22**, 022201.
- [106] Jin W, Yeh P-CH, Zaki N, Zhang D, Sadowski J T, Al-Mahboob A, van der Zande A M, Chenet D A, Dadap J I, Herman I P, Sutter P, Hone J, and Osgood, R M Jr., 2013 *Phys. Rev. Lett.* **111**, 106801.
- [107] Zhang Y, Chang T-R, Zhou B, Cui Y-T, Yan H, Liu Z, Schmitt F, Lee J, Moore R, Chen Y, Lin H, Jeng H-T, Mo S-K, Hussain Z, Bansil A, and Shen Z-X, 2014 *Nature Nanotechnology* **9**, 111.
- [108] Alidoust N, Bian G, Xu S Y, Sankar R, Neupane M, Liu C, Belopolski I, Qu D-X, Denlinger J D, Chou F-C, and Hasan M Z, 2014 *Nature Communications* **5**, 4673.
- [109] Zhu Z Y, Cheng Y C, and Schwingenschlögl U, 2011 *Phys. Rev. B* **84**, 153402.
- [110] Mahatha S K, Patel K D, and Menon K S R, 2012 *J. Phys.: Condens. Matter* **24** 475504.
- [111] Zhang Y J, Oka T, Suzuki R, Ye J T, and Iwasa Y, 2014 *Science* **344**, 725.
- [112] MacNeill D, Heikes C, Anderson Z, Mak K F, Ralph D C, Kormányos A, Zólyomi V, and Park J, 2015 *Phys. Rev. Lett.* **114**, 037401.
- [113] Srivastava A, Sidler M, Allain A A, Lembke D S, Kis A, and Imamoğlu A, 2015 *Nature Physics*

- 11, 141.
- [114] Aivazian G, Gong Z, Jones A M, Chu R-L, Yan J, Mandrus D G, Zhang Ch, Cobden D, Yao W, and Xu X, 2015 *Nature Physics* **11**, 148.
- [115] Li Y, Ludwig J, Low T, Chernikov A, Cui X, Arefe Gh, Kim Y D, van der Zande A M, Rigosi A, Hill H M, Kim S H, Hone J, Li Zh, Smirnov D, and Heinz T F, 2014 *Phys. Rev. Lett.* **113**, 266804.
- [116] Ivchenko E L and Pikus G E, 1995 *Superlattices and Other Heterostructures (Symmetry and Optical Phenomena)* (Springer-Verlag Berlin Heidelberg).
- [117] Cheiwchanchamnangij T and Lambrecht W R L, 2012 *Phys. Rev. B* **85**, 205302.
- [118] Kadantsev E S and Hawrylak P, 2012 *Solid State Commun.* **152**, 909.
- [119] Kośmider K and Fernández-Rossier J, 2013 *Phys. Rev. B* **87**, 075451.
- [120] Ochoa H and Roldán R, 2013 *Phys. Rev. B* **87**, 245421.
- [121] Riley J M, Mazzola F, Dendzik M, Michiardi M, Takayama T, Bawden L, Granerød C, Leandersson M, Balasubramanian T, Hoesch M, Kim T K, Takagi H, Meevasana W, Hofmann Ph, Bahramy M S, Wells J W, and King P D C, 2014 *Nature Physics* **10**, 835.
- [122] Yu H, Wu Y, Liu G-B, Xu X, Yao W, 2014 *Phys. Rev. Lett.* **113**, 156603.
- [123] Peelaers H and Van de Walle C G, 2012 *Phys. Rev. B* **86**, 241401(R).
- [124] Wickramaratne D, Lake R K, and Zahid F, 2014 *J. Chem. Phys.* **140**, 124710.
- [125] Zibouche N, Philipsen P, Heine T, and Kuc A, *Phys. Chem. Chem. Phys.* **16**, 11251.
- [126] Zhang W, Huang Zh, and Zhang W, 2014 *Nano Research* **7**, 1731.
- [127] Radisavljević B and Kis A, 2013 *Nature Materials* **12**, 815.
- [128] Baugher B W H, Churchill H O H, Yang Y, and Jarillo-Herrero P, 2013 *Nano Letters* **13**, 4212.
- [129] Larentis S, Tolsma J S, Fallahazad B, Dillen D C, Kim K, MacDonald A H, and Tutuc E, 2014 *Nano Letters* **14**, 2039.
- [130] Braga D, Lezama I G, Berger H, and Morpurgo A F, 2012 *Nano Letters* **12**, 5218.
- [131] The fit results based on the ARPES measurements of Reference [107] were communicated to us by Yi Zhang.
- [132] Eknepaku T, King P D C, Asakawa M, Buaphet P, He R H, Mo S K, Takagi H, Shen K M, Baumberger F, Sasagawa T, Jungthawan S, and Meevasana W, 2014 *Nano Letters* **14**, 1312.
- [133] Ross J S, Wu S, Yu H, Ghimire N J, Jones A M, Aivazian G, Yan J, Mandrus D G, Xiao D, Yao W, and Xu X, 2013 *Nature Communications* **4** 1474.
- [134] Ye Z, Cao T, O'Brien K, Zhu H, Yin X, Wang Y, Louie S G, and Zhang X, 2014 *Nature* **513**, 214.
- [135] Chernikov A, Berkelbach T C, Hill H M, Rigosi A, Li Y, Aslan Ö B, Reichman D R, Hybertsen M S, and Heinz T F, *Phys. Rev. Lett.* **113**, 076802.
- [136] Zhao W, Ghorannevis Z, Chu L, Toh M, Kloc C, Tan P H, and Eda G, 2013 *ACS Nano* **7**, 791.
- [137] Kozawa D, Kumar R, Carvalho A, Kumar A K, Zhao W, Wang Sh, Toh M, Ribeiro R R, Castro Neto A H, Matsuda K, Eda G, 2014 *Nature Communications* **5**, 4543.
- [138] Sundaram R S, Engel M, Lombardo A, Krupke R, Ferrari A C, Avouris Ph, and Steiner M, 2013 *Nano Letters* **13**, 1416. doi: 10.1021/nl400516a
- [139] Zeng H, Liu G B, Dai J, Yan Y, Zhu B, He R, Xie L, Xu Sh, Chen X, Yao W, and Cui X, 2013 *Scientific Reports* **3**, 1608. doi:10.1038/srep01608
- [140] Li W, Birdwell A G, Amani M, Burke R A, Ling X, Lee Y-H, Liang X, Peng L, Richter C A, Kong J, Gundlach J D, and Nguyen N V, 2014 *Phys. Rev. B* **90**, 195434.
- [141] Zhu B, Chen X, and Cui X, 2015 *Scientific Reports* **5**, 9218. doi:10.1038/srep09218
- [142] Klots A R, Newaz A K M, Wang B, Prasai D, Krzyzanowska H, Caudel D, Ghimire N J, Yan J, Ivanov B L, Velizhanin K A, Burger A, Mandrus D G, Tolk N H, Pantelides S T, and Bolotin K I, 2014 *Scientific Reports* **4**, 6608.
- [143] Dumcenco D, Ovchinnikov D, Marinov K, Lopez-Sanchez O, Krasnozhan D, Chen M-W, Gillet Ph, Fontcuberta i Morral A, Radenović A, and Kis A, 2014 *Preprint* arXiv:1405.0129.
- [144] Hanbicki A T, Currie M, Kioseoglou G, Friedman A L, Jonker B T, 2015 *Solid State*

- Communications* **203** 16.
- [145] He K, Kumar N, Zhao L, Wang Z, Mak K F, Zhao H, and Shan J, 2014 *Phys. Rev. Lett.* **113** 026803.
- [146] Ugeda M M, Bradley A J, Shi S-F, da Jornada F H, Zhang Y, Qiu D Y, Mo S-K, Hussain Z, Shen Z-X, Feng W, Louie S G, and Crommie M F, 2014 *Nature Materials* **13** 1091.
- [147] Liang Y, Huang Sh, Soklaski R, and Yang L, 2013 *Appl. Phys. Lett.* **103**, 042106.
- [148] Xiao D, Chang M-C, and Niu Q, 2010 *Rev. Mod. Phys.* **82**, 1959.
- [149] Feng W, Yao Y, Zhu W, Zhou J, Yao W, and Xiao D, 2012 *Phys. Rev. B* **86**, 165108.
- [150] Winkler R, 2003 *Spin-Orbit Coupling Effects in Two-Dimensional Electron and Hole Systems*, (Springer-Verlag Berlin Heidelberg).
- [151] Zhang Ch, Johnson A, Hsu Ch-L, Li L-J, and Shih Ch-K, 2014 *Nano Letters* **14**, 2443.
- [152] Zhang Ch, Chen Y, Johnson A, Li M-Y, Huang J-K, Li L-J, and Shih Ch-K, 2014 *Preprint* arXiv:1412.8487.
- [153] Chiu M-H, Zhang Ch, Shiu H W, Chuu Ch-P, Chen Ch-H, Chang Ch-Y S, Chen Ch-H, Chou M-Y, Shih Ch-K, and Li L-J, 2014 *Preprint* arXiv:1406.5137.
- [154] Ochoa H, Finocchiaro F, Guinea F, and Fal'ko V I, 2014 *Phys. Rev. B* **90**, 235429.
- [155] Clark S J, Segall M D, Pickard C J, Hasnip P J, Probert M I J, Refson K, and Payne M C, 2005 *Z. Kristallogr.* **220**, 567.
- [156] Private communication by Philip King, based on the results in Reference [132].
- [157] Private communication by Diana Qiu; see calculations in Reference [47].
- [158] Winkler R and Zülicke U, 2010 *Phys. Rev. B* **82**, 245313.
- [159] Geissler F, Budich J C, Trauzettel B, 2013 *New J. Phys.* **15**, 085030.
- [160] Lu Ch-P, Li G, Mao J, Wang L-M, and Andrei E Y 2014 *Nano Letters* **14**, 4628.
- [161] Liu H, Jiao L, Yang F, Cai Y, Wu X, Ho W, Gao Ch, Jia J, Wang N, Fan H, Yao W, and Xie M, 2014 *Phys. Rev. Lett.* **113**, 066105.
- [162] Carvalho A, Ribeiro R M, and Castro Neto A H, 2013 *Phys. Rev. B* **88**, 115205.
- [163] Steinhoff A, Rösner M, Jahnke F, Wehling T O, and Gies C, 2014 *Nano Letters* **14**, 3743.
- [164] Gibertini M, Pellegrino F M D, Marzari N, and Polini M, 2014 *Phys. Rev. B* **90**, 245411.
- [165] Dresselhaus G, 1956 *Journal of Physics and Chemistry of Solids* **1**, 14.
- [166] Mak K F, da Jornada F H, He K, Deslippe J, Petrone N, Hone J, Shan J, Louie S G, and Heinz T F, 2014 *Phys. Rev. Lett.* **112** 207401.
- [167] Berkelbach T C, Hybertsen M C, and Reichman D R, 2013 *Phys. Rev. B* **88**, 045318.
- [168] Berghäuser G and Malic E, 2014 *Phys. Rev. B* **89**, 125309.
- [169] Glazov M M, Amand T, Marie X, Lagarde D, Bouet L, and Urbaszek B, 2014 *Phys. Rev. B* **89** 201302(R).
- [170] Yu T and Wu M W, 2014 *Phys. Rev. B* **89**, 205303.
- [171] Fogler M M, Butov L V, and Novoselov K S, 2014 *Nature Communications* **5**, 4555.
- [172] Thilagam A, 2014 *Journal of Applied Physics* **116**, 053523.
- [173] Scholz A, Stauber T, and Schliemann J, 2013 *Phys. Rev. B* **88**, 035135.
- [174] Kechedzhi K and Abergel D S L, 2014 *Phys. Rev. B* **89**, 235420.
- [175] Ochoa H, Guinea F, and Fal'ko V I, 2013 *Phys. Rev. B* **88** 195417.
- [176] Wang L and Wu M W, 2014 *Phys. Rev. B* **89**, 115302; Wang L and Wu M W, 2014 *Phys. Rev. B* **89**, 205401.
- [177] Hatami H, Kernreiter T, and Zülicke U, 2014 *Phys. Rev. B* **90**, 045412.
- [178] Tse W-K, Saxena A, Smith D L, and Sinitsyn N A, 2014 *Phys. Rev. Lett.* **113**, 046602.
- [179] Cazalilla M A, Ochoa H, and Guinea F, 2014 *Phys. Rev. Lett.* **113**, 077201.
- [180] Yuan N F Q, Mak K F, and Law K T, 2014 *Phys. Rev. Lett.* **113**, 097001.
- [181] Abergel D S L, Edge J M, Balatsky A V, 2014 *New J. Phys.* **16**, 065012.
- [182] Mak K F, McGill K L, Park J, and McEuen P L, 2014 *Science* **344**, 1489.
- [183] Majidi L, Rostami H, and Asgari R, 2014 *Phys. Rev. B* **89**, 045413.
- [184] Rameshti B R, Moghaddam A G, and Zareyan M, 2014 *EPL* **108** 37002.

- 
- [185] Ferreiros Y and Cortijo A, 2014 *Phys. Rev. B* **90** 195426.
- [186] Klinovaja J and Loss D 2013 *Phys. Rev. B* **88**, 075404.
- [187] Yuan S, Roldán R, Katsnelson M I, and Guinea F, 2014 *Phys. Rev. B* **90**, 041402.
- [188] Cui X, Lee G-H, Kim Y D, Arefe G, Huang P Y, Lee Ch-H, Chenet D A, Zhang X, Wang L, Ye F, Pizzocchero F, Jessen B S, Watanabe K, Taniguchi T, Muller D A, Low T, Kim P, and Hone J, 2014 *Preprint* Arxiv:1412.5977.
- [189] Liu Y , Wu H, Cheng H Ch , Yang S, Zhu E, He Q, Ding M, Li D, Guo J, Weiss N O, Huang Y, and Duan X, 2014 *Preprint* Arxiv:1412.7718.
- [190] Blaha P, Schwarz K, Madsen G K H, Kvasnicka D, and Luitz J, WIEN2k, An Augmented Plane Wave + Local Orbitals Program for Calculating Crystal Properties (Karlheinz Schwarz, Techn. Universität Wien, Austria), 2001. ISBN 3-9501031-1-2.
- [191] Pradhan N R, Rhodes D, Feng S, Xin Y, Memaran Sh, Moon B-H, Terrones H, Terrones M, and Balicas L, (2014) *ACS Nano* **8** 5911.
- [192] Ruppert C, Aslan O B, and Heinz T F, (2014) *Nano Letters* **14**, 6231.
- [193] Le D, Barinov A, Preciado E, Isarraraz M, Tanabe I, Komesu T, Troha C, Bartels L, Rahman T S, and Dowben P A, (2015) at press in *J. Phys. C: Condens. Matter*.
- [194] Guo H, Yang T, Yamamoto M, Zhou L, Ishikawa R, Ueno K, Tsukagoshi K, Zhang Zh, Dresselhaus M S, and Saito R, (2015) *Preprint* arXiv:1501.07078.
- [195] Wang G, Bouet L, Glazov M M, Amand T, Ivchenko E L, Palleau E, Marie X, and Urbaszek B, (2015) *Preprint* arXiv:1503.04105.
- [196] Arora A, Koperski M, Nogajewski K, Marcus J, Faugeras C, and Potemski M, (2015) *Preprint* arXiv:1503.01682.